HISTOPATHOLOGICAL AND MRI CORRELATES OF PERINATAL WHITE MATTER INJURY

By

Art Riddle

A DISSERTATION

Presented to the Department Pediatrics, Neuroscience Graduate Program and the Oregon Health & Science University School of Medicine in partial fulfillment of the requirements for the degree of

Doctor of Philosophy

July 2011

School of Medicine

Oregon Health & Science University

CERTIFICATE OF APPROVAL

This is to certify that the PhD dissertation of Art Riddle has been approved

_____

Mentor/Advisor

_____

Member

_____

Member

_____

Member

_____

Member

TABLE OF CONTENTS

ACKNOWLEDGEMENTS

I wish to thank my mentors, Dr. Stephen Back, Dr. Rorer Hohimer and Dr. Chris Kroenke for their direction, advice and patience that were instrumental to the completion of my studies. Dr. Justin Dean provided guidance and support and was an example of the tenacity requred to succed in research. I am also thankful for all the support and kindness of my family and friends who have and continue to be patient with me. I am grateful for the support of Dr. Lowell Davis, Dr. John Bissonnette and Dr. Kent Thornburg and the Oregon Heart Center for their assistance with development of the fetal ovine model. Clyde Barlow, Jeff Kelly and Katherine Kelly were instrumental in developing the in utero blood flow measurements. Without the assistance of Josh Buser, the development of the MRI registration techniqes would not have been possible. I would like to thank Robert Kayton and Elizabeth Geltz and the OHSU Electron Microscopy Core for their assistance with EM studies.

This work was supported by grants to SAB from the National Institute of Health (P51RR000163 (CDK); National Institutes of Neurological Diseases and Stroke: KO2 NS41343 and RO1NS045737, 1RO1NS054044, R37NS045737-06S1/06S2 to SAB and 1F30NS066704 to AR), the Medical Research Foundation of Oregon,the Dickinson Foundation, a Bugher Award from the American Heart Association (SAB) and the March of Dimes Birth Defects Foundation (SAB). High-field MRI instrumentation used in this work was purchased with support from the W.M. Keck Foundation.

ABSTRACT

Objective: Although periventricular white matter injury (WMI) is the leading cause of chronic neurological disability and cerebral palsy in survivors of premature birth, the cellular-molecular mechanisms, histopathological features and neuroimaging indicators of diffuse WMI are poorly defined.

Methods: To define pathophysiologic relationships among ischemia, acute cerebral white matter damage, and vulnerable target populations, we used a global cerebral ischemia-reperfusion model in the instrumented 0.65 gestation fetal sheep model. We developed a novel method for repeated measurements of cerebral blood flow using fluorescently labeled microspheres to resolve the spatial heterogeneity of flow in situ in three-dimensional space. We also developed novel algorithms to register histopathologically defined lesions with contrast- and diffusion-weighted high-field *ex vivo* MRI data. Combined electron microscopic techniques and MRI were used to assess the burden of axonal injury.

Results: Basal flow in the periventricular white matter was significantly lower than in the cerebral cortex. During global cerebral ischemia induced by carotid occlusion, flow to all regions was reduced by nearly 90%. Ischemia of 30 or 37 min duration generated selective graded injury to frontal and parietal periventricular white matter, two regions of predilection for human WMI. Surprisingly, the distribution of white matter damage was nonuniform and was not explained by heterogeneity in the degree of ischemia. Rather, the extent of white matter damage coincided with the presence of a susceptible population of late oligodendrocyte progenitors (preOL). Despite acute preOL

degeneration, preOL density recovered to control levels by 7 days after ischemia and was ~2 fold greater at 14 days. However, pre-myelinating oligodendrocytes were significantly diminished at 7 and 14 days. WMI evolved predominantly to gliotic lesions, where arrested preOL differentiation was directly proportional to the magnitude of astrogliosis. Reduced cerebral WM volume was accompanied by four classes of MRI-defined lesions. Each lesion type displayed unique astroglial and microglial responses that corresponded to distinct forms of necrotic or non-necrotic injury. High-field MRI defined two novel hypo-intense signal abnormalities on T_2-weighted images that coincided with microscopic necrosis or identified astrogliosis with high sensitivity and specificity. Within rare necrotic lesions, axonal degeneration was common. However, within MRI-defined regions of diffuse gliosis, no change in the number of degenerating axons, intact axons or their caliber was found.

Conclusions:

These data support the hypothesis that although ischemia is necessary to generate WMI, the presence of susceptible populations of preOLs underlies regional predilection to injury, and that myelination failure in survivors of premature birth is related to preOLs that undergo a chronic progressive process, resulting in proliferation and arrest of preOL maturation. Ultrastructutural characteristics of axons appear unaltered in the major form of WMI. These studies support the potential of high-field MRI for early identification of microscopic necrosis and gliosis with preOL maturation arrest.

INTRODUCTION

Cerebral white matter injury is the most common cause of chronic neurological disability in children with cerebral palsy (Ferriero, 2004; Volpe, 2008). Improvements in the survival of very low birth weight infants have led to significant increases in the number of preterm survivors with lifelong neurological deficits (Wilson-Costello et al., 2005). These survivors have a predilection for white matter injury, which localizes primarily to the periventricular white matter. Up to 25% of children with white matter injury have the permanent motor deficits of cerebral palsy, and 25–50% have a broad range of other cognitive and learning disabilities (Litt et al., 2005). Despite this association, we lack a clear understanding of the pathogenesis of white matter injury in preterm survivors that lead to preterm white matter injury and lifelong disability in these children.

As neonatal care advances, the spectrum of neuropathology associated with white matter injury also appears to be evolving. The highest-risk period for white matter injury is between 23–32 weeks postconceptual age (Volpe, 2008). The spectrum of injury ranges from focal cystic necrosis (periventricular leukomalacia; PVL) to diffuse white matter gliosis and myelination disturbances (Kinney and Back, 1998; Hamrick et al., 2004). White matter injury commonly appears as symmetric lesions anterior or lateral to the anterior horn of the lateral ventricles (Figure 1). PVL may occur as an isolated lesion or be accompanied by diffuse white matter gliosis. PVL is characterized by coagulative necrosis deep in the WM and subventricular zone that results in loss of all cellular elements, including blood vessels, glia and axons. These lesions may evolve to cavitary cysts or mineralize and form a solid glial scar. Diffuse white matter gliosis often

surrounds these foci of necrosis and is characterized by broad regions of reactive microglia early, and astrocytes and microglia in chronic lesions. Most infants with these disorders survive prematurity, making it difficult to define pathogenic mechanisms directly in human samples, and few studies have directly addressed this. However, neuroimaging is becoming more feasible, and recent magnetic resonance imaging studies indicate that the incidence of cystic necrotic lesions may be declining, while diffuse signal abnormalities are becoming the predominant lesion (Counsell et al., 2003; Inder et al., 2003; Miller et al., 2003; Hamrick et al., 2004). In support of these MRI findings, a recent study of white matter injury cases found that diffuse white matter lesions predominated with limited focal necrosis (Back et al., 2005). Although diffusion imaging has had success in defining white matter injury weeks to months after birth, MRI changes associated with acute non-cystic white matter injury have not yet been defined.

Figure 1

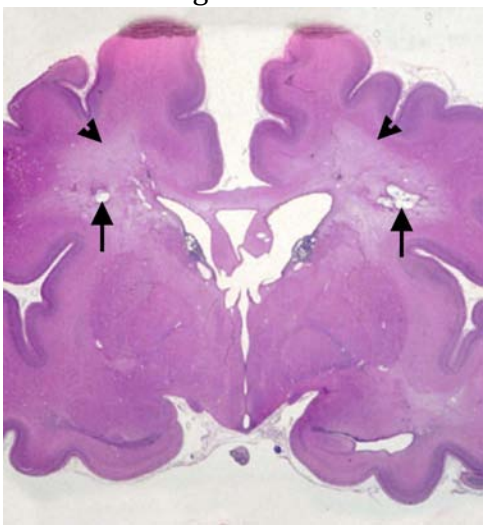

Figure 1. The pattern of human preterm white matter injury. Cystic PVL (arrows) with surrounding diffuse myelin pallor (arrowheads) is evident in this coronal section at the level of the body of the caudate.

Periventricular leukomalacia is distinguished by coagulative necrosis in the periventricular white matter that results in the destruction of all cellular elements. In early lesions, vascular endothelium and microglia have a reactive phenotype and axonal degeneration is evident (Kinney and Back, 1998). These lesions progress through a stage of prominent reactive astrogliosis before either forming cystic cavities or a solid glial scar

(Volpe, 2008). Early diffuse white matter lesions have a reactive microglial response that is followed by a robust astroglial response (Leviton and Gilles, 1984; Haynes et al., 2003). In diffuse injury, endothelium, microglia and astrocytes appear to be more resistant to degeneration.

The two major mechanisms considered to underlie white matter injury are a propensity for cerebral ischemia due to blood pressure instability combined with immature cerebrovascular regulation (Greisen and Borch, 2001; Volpe, 2008) and maternal-fetal infection (Hagberg et al., 2002). These mechanisms are not mutually exclusive, and maternal fetal infection may directly damage the brain or operate through vascular mechanisms (Young et al., 1982; Ando et al., 1988). The strongest evidence for maternal-fetal infection exists in term infants, where infection strongly correlates with the risk of cerebral palsy, although studies have failed to identify a similar risk in preterm infants (Grether et al., 2003; Nelson et al., 2003). Premature infants are predisposed to pressure passive circulation and impaired cerebral autoregulation that may lead to cerebral ischemia (Pyrds, 1991; Menke et al., 1997; Tsuji et al., 2000). Immaturity of the cerebral vasculature makes these infants able to maintain cerebral blood flow across only a narrow range of arterial pressures. Thus, when they are challenged by hypoxia or ischemia, cerebral oxygen delivery is quickly compromised. Basal blood flow is also lower in premature than term infants (Greisen, 1986; Skov et al., 1992; Yoxall and Weindling, 1998; Buchvald et al., 1999). However, current measures of cerebral blood flow lack the resolution to determine cerebral hemodynamics in human white matter, and most studies infer cerebral flow using indirect techniques such as Doppler ultrasonography. Studies with near infrared spectroscopy found that impaired

autoregulation correlated with the development of white matter necrosis and intraventricular hemorrhage (Takashima and Tanaka, 1978). Defining the basis of the vulnerability of the preterm white matter to ischemic injury will require the application of novel measurements of cerebral blood flow in animal models that reproduce the human spectrum of pathology.

Considerable progress has already been made in defining the cellular targets of white matter injury. Oligodendrocytes (OLs) produce myelin in the central nervous system when mature and develop along an established lineage, where they progressively gain in complexity (Figure 2). Early OL progenitors and late OL progenitors (preOLs) are both mitotically active and display a simple bipolar and multipolar morphology, respectively. Immature OLs and mature OLs are postmitotic and have complex multipolar morphology and form myelin, respectively. Because the

Figure 2

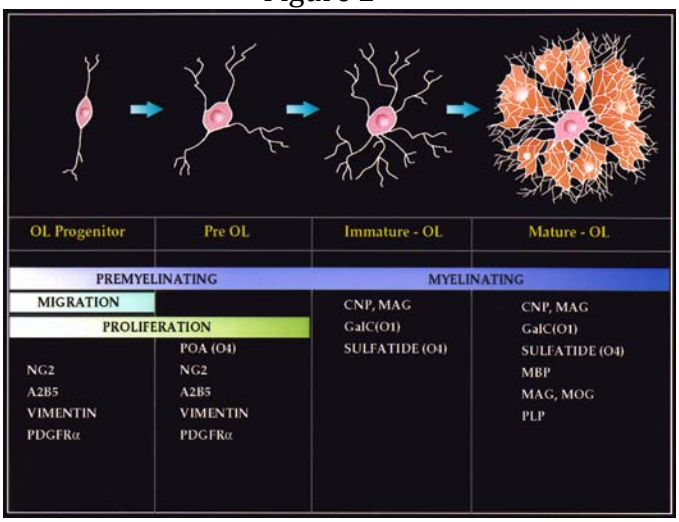

Figure 2. Maturation of the OL lineage. Four principal stages of OL lineage progression are depicted with their corresponding morphological features and capacity for myelination, migration and proliferation. Each stage is uniquely defined by a combination of marker genes or antibodies. A2B5, O4, O1 refer to mouse monoclonal antibodies. *Olig2* and *Sox10* are genes that are highly enriched in premyelinating OLs. *Olig2* is also expressed at later stage in the OL lineage. CNP indicates CNPase, 2':3'-cyclic nucleotide-3'-phosphodiesterase; GalC, galactocerebroside; MAG, myelin-associated glycoprotein; MBP, myelin basic protein; MOG, myelin oligo-dendrocyte glycoprotein; NG2, chondroitin sulfate proteoglycan 4; PDGFRα, platelet-derived growth factor-α; PLP, proteolipid protein.

period of vulnerability to white matter injury preceded myelination, white matter injury was hypothesized to be related to the degeneration of an immature stage of the OL (Volpe, 2001). During the period of high risk for white matter injury, preOLs are the primary lineage stage present in the white matter (Back et al., 2001). Moreover, the timing of differentiation of preOLs to immature OLs coincides with a decline in the risk for white matter injury (Back et al., 2002a).

In vitro and in vivo data supports the concept that preOLs may be selectively targeted by oxidative stress, a sequela of hypoxia-ischemia (Back et al., 1998; Fern and Moller, 2000; Back et al., 2002b; Baud et al., 2004; Fragoso et al., 2004; Lin et al., 2004). For example, OL progenitors undergo caspase-mediated cell death after oxidative stress in vitro (Druzhyna et al., 2003; Brault et al., 2004; Fragoso et al., 2004). Further, OL progenitors, but not mature OLs degenerate when exposed to lipid peroxidation products (Brault et al., 2004), a stable form of which is elevated in human white matter lesions (Back et al., 2005).

In vivo rat studies also support the hypothesis that maturation of the OL lineage drives vulnerability of the white matter. For example, the white matter was remarkably less susceptible to hypoxia-ischemia at postnatal day 7, compared to postnatal day 2. This change coincided with the maturation of the white matter from a state where preOLs predominated to one where immature and mature OLs predominated (Back et al., 2002b; Craig et al., 2003). Moreover, at postnatal days 2 and 7, preOLs were remarkably more vulnerable to injury than later stages of the OL lineage. Myelination disturbances have also been reported in 7-day-old rat pups after hypoxia-ischemia, although the extent of vulnerability of OL lineage stages was not determined (Follet et al., 2000; Liu et al.,

2002). However, small animal and rodent models have a paucity of white matter and a propensity for mixed gray and white matter damage that significantly limit our ability to extrapolate their findings to humans. Thus, there is a critical need for animal models of white matter injury that are more similar to human disease.

Currently, the instrumented fetal sheep (0.65 gestation) is the most promising model for determining the pathogenesis of periventricular white matter injury. First, unlike rodents, the ovine fetus is gyrencephalic and contains white matter similar in size, composition and organization to human fetal white matter (Barlow, 1969; Penning et al., 1994). The ovine fetus also displays pressure passive circulation and has cerebral hemodynamics similar to human (Hagberg et al., 2002). The size of the ovine white matter permits experimental techniques that are not feasible in rodents more accessible, including in situ measurement of blood flow and real-time physiological measures, such as blood pressure and blood oxygenation. Neurodevelopmental measures such as neurogenesis, the onset of cortical sulcation and the onset of the auditory and somatosensory evoked potentials are similar between the 0.65 gestation ovine fetus and the 24–28 week human preterm infant (Cook et al., 1987b; Cook et al., 1987a; Reddy et al., 1998). Thus, the instrumented fetal sheep at 0.65 gestation is anatomically, physiologically and developmentally similar to the preterm human during the high-risk period for white matter injury. It is also the most suitable model to address questions regarding the pathogenesis of white matter injury, such as the roles of cerebral hemodynamics and cellular vulnerability in acute responses to hypoxia-ischemia.

In this dissertation I have used the fetal sheep model define pathogenetic mechanisms of cerebral injury in survivors of premature birth ultimately aimed to devise therapeutic

strategies to prevent or repair the myelination disturbances related to cerebral palsy and cognitive deficits, which are very common in these children. I have built upon prior observations in human and rodent that defined maturation-dependent mechanisms of perinatal white matter injury, which involve selective degeneration of preOLs triggered by oxidative damage and hypoxia-ischemia. Chapter one addresses the contributions of heterogeneities in cerebral ischemia and the distribution of susceptible preOLs to the regional predilection to acute ischemia. In chapter two I address the evolution of acute injury into multiple types of lesions that cause myelination disturbances and determine the burden of each type of lesion. Chapter three addresses the contribution of axonal degeneration or disruptions in axonal development to myelination disturbances in necrotic and diffuse gliotic lesions.

CHAPTER 1

SPATIAL HETEROGENEITY IN OLIGODENDROCYTE LINEAGE MATURATION AND NOT CEREBRAL BLOOD FLOW PREDICTS FETAL OVINE PERIVENTRICULAR WHITE MATTER INJURY

Art Riddle[1], Ning Ling Luo[1], Mario Manese[1], Douglas J. Beardsley[1], Lisa Green[4], Dawn A. Rorvik[4], Katherine A. Kelly[4], Clyde H. Barlow[4], Jeffrey J. Kelly[4], A. Roger Hohimer[3] and Stephen A. Back[1, 2, 5]

Departments of Pediatrics[1], Neurology[2] and Obstetrics and Gynecology[3], Oregon Health & Science University, Portland, Oregon and Barlow Scientific Inc., and The Evergreen State College[4], Olympia, Washington

Riddle A, Luo N, Manese M, Beardsley D, Green L, Rorvik D, Kelly K, Barlow C, Kelly J, Hohimer A, Back S (2006) Spatial heterogeneity in oligodendrocyte lineage maturation and not cerebral blood flow predicts fetal ovine periventricular white matter injury. Journal of Neuroscience 26:3045-3055.

ABSTRACT

Although periventricular white matter injury (PWMI) is the leading cause of chronic neurological disability and cerebral palsy in survivors of premature birth, the cellular-molecular mechanisms by which ischemia-reperfusion contributes to the pathogenesis of PWMI are not well-defined. To define pathophysiologic relationships among ischemia, acute cerebral white matter damage and vulnerable target populations, we employed a global cerebral ischemia-reperfusion model in the instrumented 0.65 gestation fetal sheep. We developed a novel method to make repeated measurements of cerebral blood flow using fluorescently-labeled microspheres to resolve the spatial heterogeneity of flow *in situ* in three-dimensional space. Basal flow in the periventricular white matter (PVWM) was significantly lower than in cerebral cortex. During global cerebral ischemia, induced by carotid occlusion, flow to all regions was reduced by nearly 90%. Ischemia of 30 or 37 min duration generated selective graded injury to frontal and parietal PVWM, two regions of predilection for human PWMI. Injury was proportional to the duration of ischemia and increased markedly with 45 min of ischemia to extensively damage cortical and subcortical gray matter. Surprisingly, the distribution of PVWM damage was not uniform and not explained by heterogeneity in the degree of white matter ischemia. Rather, the extent of white matter damage coincided with the presence of a susceptible population of late oligodendrocyte progenitors. These data support that while ischemia is necessary to generate PWMI, the presence of susceptible populations of oligodendrocyte progenitors underlies regional predilection to injury.

ACKNOWLEDGEMENTS

This work was supported by grants to SAB from the National Institute of Health (NIH) (KO2 NS41343 and RO1 NS045737), from the Medical Research Foundation of Oregon and the Dickinson Foundation. We are grateful for the support of Dr. Lowell Davis, Dr. John Bissonnette and Dr. Kent Thornburg and the Oregon Heart Center. This paper is dedicated to Dr. Joseph J. Volpe on the occasion of the scientific symposium at Boston Children's Hospital to honor his leadership as the Chief of Pediatric Neurology. His relentless efforts to determine the causes of brain injury in premature infants served as the inspiration for this work.

INTRODUCTION

Periventricular white matter injury (PWMI) is a common and leading cause of chronic neurological disability in survivors of premature birth that manifests as cerebral palsy and cognitive impairment (Back and Rivkees, 2004). Two potential mechanisms for PWMI are cerebrovascular immaturity (Greisen and Borch, 2001; Volpe, 2001) and maternal-fetal infection (Hagberg et al., 2002). The timing of appearance of late oligodendrocyte progenitors (preOLs) coincides with the high-risk period for PWMI (Back et al., 2001). Early PWMI lesions display significant lipid peroxidation injury that results in pronounced degeneration of human preOLs (Haynes et al., 2003; Back et al., 2005). These findings are consistent with a role for ischemia-reperfusion injury in the pathogenesis of PWMI. However, the extent to which susceptible preOLs define the magnitude and distribution of injury is unclear.

Current measures of global cerebral blood flow lack the spatial resolution to define cerebral hemodynamics in human periventricular white matter. Moreover, prior experimental models have not established a relationship between PWMI and perturbations in periventricular blood flow. Small fetal and neonatal animal models have been uninformative due to a paucity of cerebral white matter, a propensity for mixed gray and white matter injury and the technical limitations of invasive blood flow measurements (Back, 2001). By contrast, the immature ovine fetus (0.65 gestation) is a widely studied preparation that displays cerebral hemodynamics similar to human and permits repeated physiological measurements *in utero* in the unanesthetized state (Hagberg et al., 2002). The immature ovine brain is similar to preterm human between 24-28 weeks in terms of the completion of neurogenesis, the onset of cerebral sulcation, the detection of the cortical component of the auditory and somatosensory evoked potentials and an increased predilection for white matter injury (Penning et al., 1994; Reddy et

al., 1998). Thus, the cephalically hypotensive immature ovine fetus appears to be particularly susceptible to hypoxia-ischemia, but prior studies provided no data regarding blood flow to periventricular white matter.

To study the pathophysiologic relationships among ischemia, acute cerebral white matter damage and vulnerable preOLs during prematurity, we developed a new method to repeatedly measure cerebral blood flow using fluorescently-labeled microspheres to resolve the spatial heterogeneity of fetal blood flow in situ in three-dimensional space. Since preOLs are the oligodendrocyte (OL) lineage stage most susceptible to hypoxia-ischemia (Back et al., 2002b), we hypothesized that cerebral ischemia is necessary but not sufficient to cause white matter damage and that the magnitude and distribution of damage is related to the distribution of preOLs. When the immature ovine fetus was subjected to global cerebral ischemia, relatively selective graded cerebral white matter damage resulted that was proportional to the duration of ischemia. The distribution of damage was not uniform even though no significant differences were observed in white matter ischemia. Rather, the heterogeneity in distribution of white matter damage coincided with the extent to which susceptible preOLs were present. These data support that ischemia is necessary, but not sufficient to generate PWMI and that the presence of susceptible preOLs is related to the regional predilection to injury.

MATERIALS AND METHODS

Surgical Procedure. This instrumented fetal cerebral hypoperfusion preparation (Reddy et al., 1998) and the general surgical procedures (Chao et al., 1991) were previously described. Time-bred sheep of mixed western breed (88-91 days gestation; term, 145 days) were studied. Twin pregnancies were studied so that each experimental fetus had a twin control. Fetuses were operated with sterile technique under general anesthesia (1% halothane in O_2 and N_2O). Vinyl catheters were placed in the amniotic cavity and into a fetal axillary artery and fetal hindlimb vein. To confine the cerebral blood supply to the carotid arteries, the vertebro-occipital anastomoses were ligated bilaterally. These anastomoses connect the vertebral arteries, supplied by the thoracic aorta, with the external carotid arteries that are fed by the brachiocephalic (Baldwin and Bell, 1963). Hydraulic occluders (silastic) were placed on each carotid artery. After closure of the uterus, the lines were externalized and 1 million units of penicillin G infused into the amniotic cavity. Post-operative housing was on clean dry bedding in an individual cage with free access to food and water and close visual contact with other sheep.

Cerebral hypoperfusion studies. A total of 37 animals (see results for the number dedicated to each experiment) were studied on the 2nd or 3rd post-operative day. Pressure transducers and a strip-chart recorder (TA 6000; Gould Instruments, Valley View, OH) recorded mean arterial blood pressure (MABP) in the fetal artery relative to amniotic fluid pressure. Fetal heart rate (HR) was calculated from triplicate measurements of the arterial pressure pulse intervals over a continuous recording of >20 seconds. Fetuses were studied only if they demonstrated normal oxygenation (>6 ml O_2 / 100 ml blood) and blood indices, as previously described (Chao et al., 1991). Sustained cerebral hypoperfusion of 30, 37 or 45 min duration was initiated by bilateral

carotid artery occlusion after inflation of the carotid occluders. Cerebral reperfusion was established by deflation of the occluders and was studied at either 15 or 60 min of restored flow.

Blood Analysis. One ml blood samples taken anaerobically from the fetal axillary artery were analyzed for arterial p_aH, P_aO_2, P_aCO_2 (corrected to 39°C; IL Synthesis 10 pH/Blood Gas Analyzer; Instrumentation Laboratory, Lexington, MA), hemoglobin content (Thb), arterial oxygen content (CaO_2), arterial oxygen saturation ($SatO_2$, IL 682 Co-Oximeter; Instrumentation Laboratory) and hematocrit (Hct, capillary microfuge). Fetuses were only studied if they demonstrated normal fetal oxygenation, defined as >6 ml O_2 / 100 ml blood, at a 24 h recovery from the operation.

Microsphere injection protocol. Fetal brain blood flow was measured spatially by the fluorescent microsphere distribution and reference sample method (Bernard et al., 2000). Fluorescent microspheres with four different colors (15 μm diameter; F-17047, F-17048, F-17048, F-17050; Molecular Probes, Eugene, OR) had the following peak excitation and emission: green (450/480) yellow (515/534), red (580/605) and scarlet (650/685). Approximately 3 x 10^6 microspheres suspended in 1 ml of saline with 0.05% Tween were sonicated and then injected over 30 seconds into the fetal hindlimb vein followed by a 2 ml flush with saline. Starting just before and continuing 2 min after each injection, a reference blood sample was drawn at 0.75 ml/min into a syringe mounted in a syringe pump (Harvard Apparatus Co., Dover, MA).

Tissue handling. At 24 or 72 h after cerebral reperfusion began, the ewe and fetuses were killed by intravenous injection of the ewe with Euthasol (Virbac Inc, Ft. Worth, TX). Fetal brains were immersion fixed at 4° C in 4% paraformaldehyde in 0.1M phosphate buffer, pH 7.4 for two days and then stored in PBS. The brains to be analyzed for microspheres, were subsequently immersed in 20% sucrose until they sank and then rapidly frozen in OCT.

Acquisition of microsphere distributions with the Imaging CryoMicrotome (ICM)™. Fluorescent microsphere detection and localization was performed with the ICM (Barlow Scientific, Inc., Olympia, WA) (Kelly et al., 2000), which combines fluorescence digital imaging of frozen tissue together with serial cryostat sectioning to determine the three-dimensional (3D) location of every microsphere. The accuracy of the ICM approach for measurement of regional blood flow versus radioactive and standard fluorescence microsphere methods has been validated (Bernard et al., 2000). The entire frozen fetal brain containing microspheres was mounted in the ICM and serially sectioned to yield ~1000, 38 μm-thick sections. Fluorescence images of the microspheres in the tissue block face were acquired at 25 μm resolution. At regular intervals, adjacent sections were retrieved from the ICM for histological analysis. Fluorescent microspheres in reference blood samples were counted so that the distribution of blood flow could be related to absolute blood flow for each color. A hole drilled into a block of frozen OCT was filled with blood that had been sonicated to disperse microspheres and the sample was frozen rapidly. An aliquot of each reference sample was serially sectioned and imaged as for the tissue samples.

Image Analysis for Regional Blood Flow. ICM-acquired fluorescence images, were preprocessed to correct for variations in illumination intensity and detector response. The images were analyzed as previously described to distinguish microspheres from background tissue fluorescence and to determine the 3D location of each microsphere (Bernard et al., 2000).

Measurement of Regional Cerebral Blood Flow. Unbiased *in situ* measurements of blood flow were made in frontal and parietal cortex and PVWM in a blinded manner by digital dissection of anatomically defined regions (Gluckman and Parsons, 1983; Vanderwolf and Cooley, 1990). ICM tissue block face images and the corresponding digitized images of the Nissl sections were imported to Amira 3-D image analysis software (TGS, San Diego, CA). All regions were

sampled in the coronal plane and contained within a region that extended 4300 μm posterior to the genu of the corpus callosum (frontal blood flow) or posterior to the level of the ventral thalamic nucleus, tail of the caudate and mammillary bodies (parietal blood flow). The 3D-ROIs were created by systematically outlining anatomical boundaries ascertained from co-registered Nissl sections at both extents and the middle of the sample region. The ROI volumes were at least 35 mm^3. 2D-ROI boundaries were checked in every 10^{th} slice for edge alignment and an interpolation algorithm applied to define volumetric ROIs encompassing the 110 slices prior to the incorporation of blood flow data. Hence, ROIs were defined from the histological data sets prior to co-registration with the microsphere data set. The operator was, thus, masked to the blood flow data set to ensure completely unbiased data analysis. The number of microspheres within the ROIs was then determined. Blood flow was calculated from the number of microspheres in the ROI per unit volume, the reference sample withdrawal rate and the number of microspheres in the reference sample. Blood flow is reported as mL/min/100g tissue, based upon a tissue specific gravity of 1.02.

Appropriate anatomical boundaries were systematically defined in the Nissl sections at each level. The frontal PVWM was defined as the region bounded by the apex of the lateral ventricle and three major dorsal sulci: the diagonal, ectomarginal and cingulate sulci. Within this region, a line was drawn between the depth of the ectomarginal sulcus and the apex of the lateral ventricle that divided the PVWM into the medial and lateral PVWM. The midpoint of this line was used to define a standard region of the PVWM that was sampled in all images. This region comprised the central 50% of the PVWM. Hence, this region did not contact the SVZ, the cortical mantle, the white matter adjacent to the depths of sulci or the superficial white matter (SWM) contained within the gyri. Parietal PVWM was defined as the region bounded by the

lateral aspect of the lateral ventricle as it extends between the caudal ectosylvian sulcus and the marginal sulcus. Within this region, a line was drawn from the depth of the caudal ectosylvian sulcus and perpendicular to the lateral ventricle. The midpoint of this line was used to define a standard region that comprised the central 50% of the parietal PVWM. ROIs of the frontal cortical mantle were outlined on the dorsal surface of three primary gryi present at 0.65 gestation: the marginal, ectomarginal and rostral suprasylvian gyri. ROI's of the parietal cortical mantle were outlined on the dorsal surface of the marginal, ectomarginal and caudal suprasylvian gyri.

Generation of Two Dimensional (2D) Blood Flow Images. The discrete locations for fluorescent microspheres were visualized as a 2D spatial probability distribution using image convolution (Russ, 1999). Virtual 2-mm-thick sections were created in the plane of sectioning that corresponded to 53 coronal tissue block face images and all the microspheres locations identified therein. Tissue edges of each 2 mm section were defined using the middle tissue block image by threshold routines that were manually verified; this created precise "masks" that defined tissue areas. The microsphere locations were registered on the tissue mask image as an integer number corresponding to the number of microspheres (0,1,2) at any Z location for each pixel (2000x2000) in the X-Y plane. These images were convolved with a 1 mm radius circular kernel whose elements were evenly weighted and were the same size as the image pixels. The luminosity of each pixel in the convolved image thus represented the number of microspheres in a 1 mm radius from each pixel in the tissue image. These convolved microsphere image flow values were divided by an image created by an identical convolution of the binary, tissue mask image. This normalized flow to the volume of tissue available for flow and prevented tissue

edges from appearing to be hypo-perfused. Finally, the image was converted to a pseudo-color flow image using the reference blood sample microsphere to flow ratio.

Immunohistochemical Studies. Fixed fetal brains were coronally-sectioned into serial 6 mm-thick blocks of tissue with a matrix tissue slicer. Tissue blocks were serially sectioned free-floating (50 μm) in PBS with a Leica VTS-1000 vibrating microtome. The detailed immunohistochemical protocols to visualize specific cell types were previously described (Back et al., 2001). OL lineage cells were visualized with the O4 and O1 monoclonal antibodies. Fluorescent double-labeling to distinguish preOLs (O4+O1-) and immature OLs (O4+O1+) employed a biotinylated O4 antibody and the O1 antibody. Astroglia were visualized with a rabbit anti-bovine glial fibrillary acidic protein (GFAP) antisera (Z-0334; DAKO, Carpinteria, CA) or with a mouse anti-human vimentin antibody (Clone V9, V6630; Sigma, Saint Louis, MO). Microglia and macrophages were visualized with the Bandeiria griffonia isolectin B4, biotinylated (1:100; Sigma, Saint Louis, MO). Axons were visualized with mouse monoclonal antibodies SMI 312 and SMI 31 (1:1000; Covance, Berkley, CA). Dr. Anu Srinivasan generously provided the anti-activated caspase-3-antibody (CM-1; Idun Pharmaceuticals, La Jolla, CA). Dr. Greg M. Cole generously supplied Fractin rabbit antisera. For fluorescent immunohistochemical studies, tissue sections were counterstained with Hoechst 33324.

Quantification of the density of TUNEL-labeled nuclei. Degenerating nuclei in frontal and parietal tissue serial adjacent sections were visualized by a TUNEL method for fluorescent *in situ* end-labeling of double-stranded DNA fragmentation (Back et al., 2002b). Sections were counterstained with Hoechst 33324 to delineate regional boundaries. Several strategies were done systematically to avoid introduction of counting bias. Fluorescent counterstain of nuclei was used to avoid overlapping fields. A field was not counted if it contained a tear or cerebral

vessel that comprised more than ~5% of the field. Cell counts were not done within fields adjacent to edges of the tissue section to avoid potential "edge artifacts," with the exception of the subventricular zone (SVZ) where the structure is narrow and adjacent to the third ventricle. Every field containing TUNEL-labeled nuclei within the cerebral cortex, PVWM, SVZ, caudate, putamen or hippocampus was photographed at 20x or 40x magnification (Hammamatsu Orca ER cooled CCD camera and Improvision Openlab 4.0.2) by AR. Between 20-80 images were counted by MM in a blinded manner in each of two adjacent sections. It should be noted that absolute stereologic methods were not feasible because of the uneven thickness inherent in the vibrating microtome-cut serial sections used for TUNEL and O4 counts and the limited penetration of antibodies into the ~50 μm thick sections (Guillery and Herrup, 1997). Free-floating sections were not subjected to freeze-thaw or dehydration with alcohols, which yielded optimal immunohistochemical localization of the O4 and O1 antibodies in preterm brain (Back et al., 2001). Under the ischemic conditions and survival times analyzed, there were no cystic or necrotic lesions that resulted in significant tissue distortion or shrinkage (see Results).

Generation of Composite Pseudo-color TUNEL maps. The distribution of cerebral lesions was plotted in the same regions from which digitized images of TUNEL-labeled nuclei were acquired. Two sections at frontal and parietal levels were analyzed in each of four animals subjected either to 30, 37 or 45 of ischemia (i.e., eight sections were used to generate each composite image of the distribution of lesions for the four animals in each experimental group). For each section, a low-power digital fluorescent image of the distribution of Hoechst 33324 stained nuclei in the entire section was acquired with a BioRad ChemiDoc (QuantityOne version 4.4.1 image acquisition software), contrast-enhanced and enlarged (Adobe Photoshop 8.0). These digital images were traced to generate maps that defined the boundaries of major cortical and

subcortical structures. The location of each lesion was recorded on these maps. Lesion boundaries were defined by the distribution of TUNEL-labeled nuclei and confirmed by Hoechst 33324 fluorescent counterstain, which permitted identification of condensed nuclei associated with degenerating cells.

The composite pseudo-color TUNEL maps for each level were generated by overlay of the individual lesion maps onto a representative control map. The control map was generated from a Nissl-stained control section that was imaged at high resolution on a color flatbed scanner (CanonScan 9900F with Adobe Photoshop 8.0). In order to match anatomical boundaries between sections, digital images from the lesion maps were overlaid onto the control map and resized to the edges of the control section, lateral ventricle and basal ganglia (Adobe Photoshop 8.0). A composite image of the eight lesion maps for each experimental group was then generated. Briefly, the eight anatomically-registered images were added as layers to a single document (Adobe Photoshop 8.0). The area encompassed by each lesion was filled in and the opacity of each layer was reduced to 20%. The image was then flattened to create a gray-scale image with up to seven gray intensities correlating to the number of times lesions overlapped at a given point. The grayscale palette was then replaced with a pseudocolor palette ranging from blue (no lesions) to red (7 lesions).

Quantification of the density of O4-labeled cells. The total density of O4-labeled cells in the medial and lateral PVWM followed the protocol, described above, for TUNEL counts. Cells were counted in a blinded manner in a minimum of three serial adjacent sections. Cell profiles that contained a nucleus, visualized with Hoechst 33324, were counted with a 20x (0.125 mm^2/field) objective equipped with a counting grid. The profiles of both intact-appearing and degenerating O4-labeled cells were counted and together comprised the calculation of total

density of O4-labeled profiles. Degenerating O4-positive cells were confirmed to contain a degenerating nucleus. For each lesion, a minimum of 40 fields was counted. A minimum of 60 fields was counted for each control region.

Statistical Analysis. Data analysis was performed using SPSS 12.0 statistical software. Blood flow data were expressed as mean ± 1 SEM. Comparisons between regions or between basal flow and occlusion were performed using paired two-tailed t tests. Blood gas, hemodynamic data and regional TUNEL indices were analyzed using ANOVA for repeated measures with *post hoc* inference testing done with Bonferroni or Least Significant Differences (LSD) test. Cell counts and time-course TUNEL data were analyzed with unpaired two-tailed t tests using SPSS prescribed corrections for equal or unequal variances where appropriate.

RESULTS

Ovine OL lineage progression at 0.65 gestation coincides with human during the high-risk period for PWMI.

We first determined if cerebral white matter maturation in the 0.65 gestation sheep is similar to that of human preterm infants at risk for PWMI. Since preOLs predominate in human PVWM during the high-risk period for PWMI (Back et al., 2001), we determined the distribution of OL lineage stages in the 0.65 gestation sheep. Figure 1A-C compares the distribution of somata labeled immunofluorescently with a biotinylated O4 (bO4, red) and the O1 antibody (O1, green) in the medial and lateral frontal PVWM (PVWM*m* and PVWM*l*). We studied frontal PVWM, because, this is a region of particular predilection for PWMI in survivors of premature birth (Kinney and Back, 1998). We first confirmed that the total density of preOLs (O4+O1-) and immature OLs (O4+O1+) (defined as total O4-labeled cells) was similar in the PVWM*m* (496 ± 59 cells /mm^2; mean ± SD) and the PVWM*l* (471 ± 60 cells/mm^2). OL lineage maturation was markedly less advanced in the PVWM*m* than in the PVWM*l*. PreOLs comprised 84 ± 2% of the total O4-labeled cells in the PVWM*m*, but in the PVWM*l* comprised only 39 ± 1% (mean ± SEM, n=4; $p<0.001$). There was, thus, about a 3-fold greater number of immature OLs in the PVWM*l* than in the PVWM*m*. Parietal PVWM had less regional variation in OL lineage maturation than frontal PVWM. PreOLs comprised 68 ± 8% of the total O4-labeled cells in the parietal PVWM. Hence, OL lineage maturation in the PVWM*m* and parietal PVWM of the 0.65 gestation fetal sheep is similar to human preterm PVWM in that preOLs were the major OL stage present.

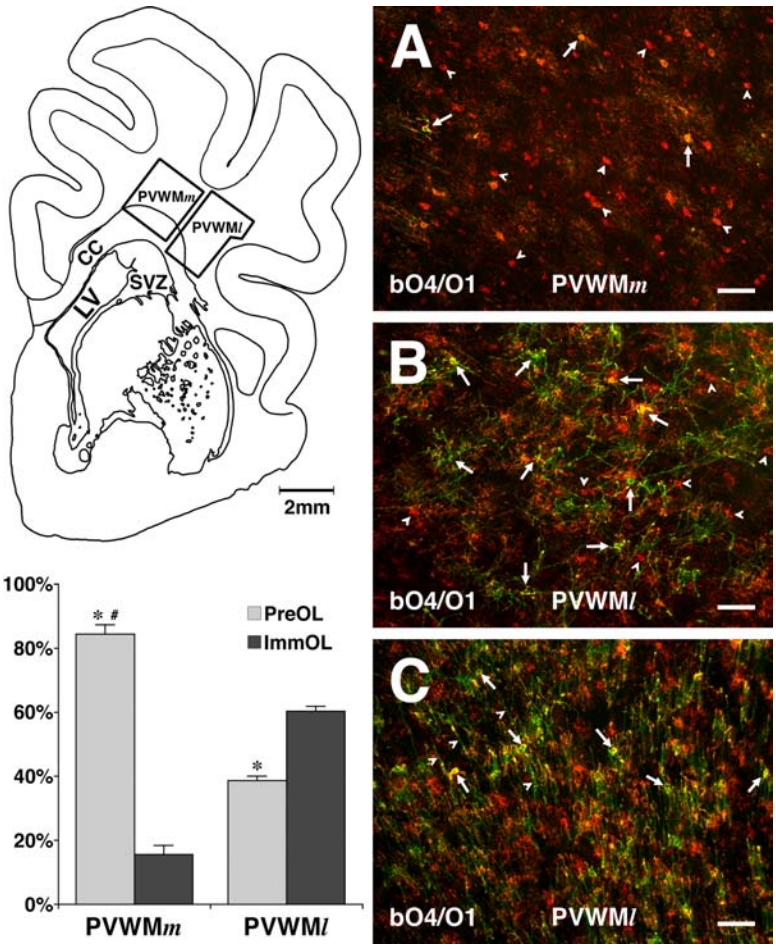

Figure 1. Spatial heterogeneity of OL maturation in "0.65 gestation" ovine brain. At *top left*, a representative frontal section from the ovine brain shows schematically the approximate boundaries of the medial (PVWM*m*) and lateral (PVWM*l*) regions of the frontal PVWM. See Materials and Methods section ("Measurement of regional cerebral blood flow") for the definition of the boundaries of the PVWM analyzed for cell counts and blood flow measurements. *A-C* show the differences in OL maturation between the PVWM*m* and the PVWM*l* by immunohistochemical double-labeling with bO4 (red) and O1 (green) antibodies. *A*, The PVWM*m* contains few immature OLs, (*arrows*) (O4+, O1+) and numerous single labeled preOLs (*arrowheads*) (O4+, O1-). *B*, The PVWM*l* contains more differentiated cells with larger, more developed processes. The majority are immature OLs (*arrows*), and a minority are preOLs (red; *arrowheads*). *C*, Consistent with the more mature state of the white matter in the PVWM*l*, numerous O1-labeled myelinated axons (*arrowheads*) are also seen in association with the immature OLs (*arrows*) and the smaller population of preOLs (red). The graph (*bottom left*) shows the relative percentages of preOLs and immature OLs in the PVWM*m* and the PVWM*l*. PreOLs predominate in the PVWM*m*, comprising over 84% of the total OLs and immature OLs comprise the remaining 16%. In the PVWM*l*, immature OLs are markedly increased and comprise about 62% of total OLs (* $p<0.001$ preOLs *vs*. immature OLs for PVWM*m* and PVWM*l*; # $p<0.001$ preOLs in PVWM*m* *vs*. PVWM*l*: unpaired two-tailed t tests). Abbreviations: CC, corpus callosum; LV, lateral ventricle; SVZ, subventricular zone. Scale bars: *A*, *B*, *C*, 200 μm.

Basal cerebral blood flow is low in the PVWM.

Since the developmental predilection for PWMI appears related to vascular anatomic immaturity of human PVWM (Volpe, 2001), we quantified regional cerebral blood flow by *in situ* analysis of fluorescent microsphere distributions. Table 1 demonstrates that under basal conditions the

fetuses exhibited normal physiological parameters (mean ± SD). By 30 min of ischemia, there was a small but consistent increase in P_aO_2, $SatO_2$ and CaO_2. At 15 min after reperfusion, all blood gas and hemodynamic values returned to basal levels.

	Basal	Ischemia	15 Post Ischemia
HR	197 ± 16	196 ± 23	206 ± 24
MABP	36 ± 4	37 ± 4	35 ± 4
p_aH	7.39 ± 0.03	7.39 ± 0.02	7.38 ± 0.03
p_aCO_2 (mmHg)	46 ± 3	45 ± 4	47 ± 4
p_aO_2 (mmHg)	24 ± 2	28 ± 3 *	25 ± 3
HCO_3^- (mmol/L)	28 ± 2	27 ± 2	27 ± 2
THb (mmol/L)	10 ± 1	10 ± 1	9 ± 1
$SatO_2$ %	73 ± 7	81 ± 5 *	73 ± 9
CaO_2 (Vol%O_2)	9 ± 2	10 ± 1 *	9 ± 1
Hct %	29 ± 4	30 ± 3	28 ± 4

Table 1: Fetal MABP, HR, p_aH, blood gases, arterial oxygen content and Hct 10 min before ischemia (basal), at 30 min of ischemia and 15 min after ischemia. Data are mean ± SD. Basal, *n*=33; Ischemia, *n*=28; 15 min Post Ischemia, *n*=33 (* $p<0.001$ *vs*. Control: one-way ANOVA with *post hoc* Bonferroni for multiple comparisons).

Figure 2 demonstrates our approach to obtain high-resolution spatial blood flow measurements from animals subjected to 45 min of ischemia (n=8). Fig. 2A shows representative data obtained after the entire fetal brain, containing fluorescent microspheres, was frozen, mounted in a cryomicrotome and serially sectioned. A Nissl section is shown alongside a corresponding raw fluorescence ICM image that shows the location of microspheres and a reconstructed map of blood flow for the same region (Flow). Fig. 2B-E shows convolved maps of frontal and parietal blood flow under basal and ischemic conditions. Figures 2B,C show that basal blood flow in the frontal and parietal PVWM (arrows) was markedly lower than several adjacent regions, particularly the cerebral cortex (dorsal arrowheads) and the pons (ventral arrowheads). Figures 2F,G show data obtained by query of anatomically defined ROIs and calculation of the mean blood flow for these ROIs through *post hoc* digital analysis. Mean basal flow rates measured in frontal and parietal cerebral cortex were 84 ± 13 mL/min/100g and 86 ± 11 mL/min/100g, respectively. By contrast, basal flow rates were significantly lower in the frontal and parietal PVWM (33 ± 4 mL/min/100g and 26 ± 4 mL/min/100g, respectively, $p<0.001$).

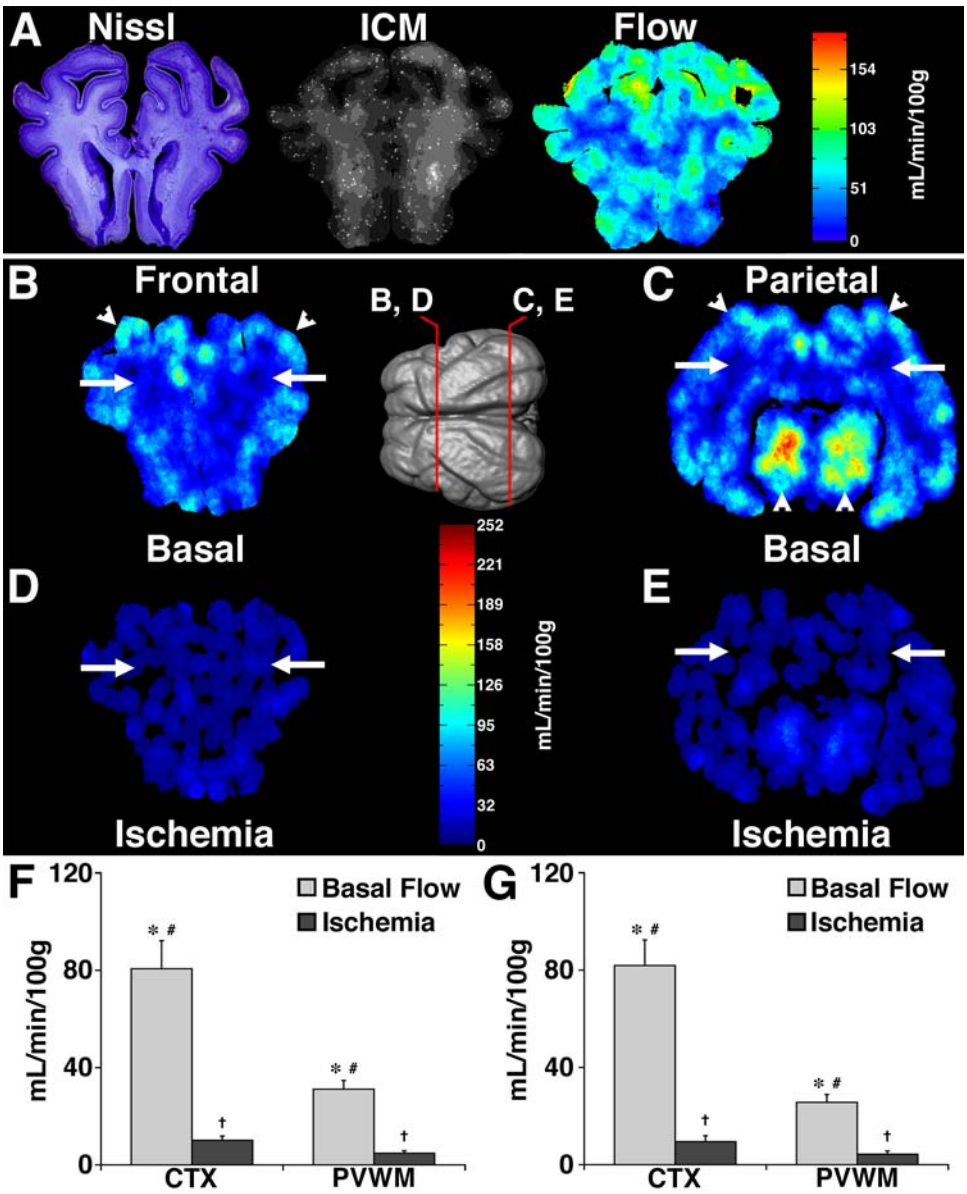

Figure 2. Quantification of fetal cerebral blood flow in situ under conditions of basal cerebral blood flow and global ischemia. *A*, Nissl stained coronal frontal section that corresponds to the ICM image (*middle*) and convolved image of blood flow (*right*). *B-E*, The center image represents a 3-D surface reconstruction (Amira, TGS, San Diego, CA) of magnetic resonance images of a 0.65 gestation ovine control brain that indicates the frontal and parietal levels at which the blood flow analysis was done in B-E. *B*, *C*, Representative pseudo-color basal flow images show higher blood flow (*light blue*) in cortical gray matter areas (arrowheads) and lower flow (*dark blue*) in the PVWM (arrows). The pons (double arrowheads, C) had higher basal flow rates than any region of the cerebrum. *D*, *E*, During global ischemia, blood flow was dramatically reduced in all regions and approached zero (dark blue/black) in the PVWM (arrows). *F*, *G*, Blood flow measured by digital dissection in the frontal (F) and parietal (G) cortex (CTX) and PVWM during basal blow and ischemia. In F, G, * $p<0.001$, basal flow *vs*. ischemia; # $p<0.001$, basal flow CTX *vs*. basal flow PVWM; † $p<0.001$, ischemia CTX *vs*. ischemia PVWM: paired two-tailed t tests.

Global ischemia severely and proportionally reduced cerebral blood flow.

We next determined the effect of global ischemia on blood flow in selected regions of the immature ovine cerebrum. By 30 min of ischemia, blood flow decreased markedly throughout the brain (Fig. 2D, E). In the frontal and parietal cerebral cortex, flow decreased significantly to 10 ± 2 mL/min/100g (14 ± 4% of basal flow; $p<0.001$) and 10 ± 2 mL/min/100g (13 ± 3%; $p<0.002$), respectively (Fig. 2F, G). When compared to cerebral cortex, the PVWM decreased to a similarly low percentage of basal flow (*frontal*, 15 ± 2%; *parietal*, 16 ± 4%). However, the absolute flow during ischemia was significantly lower in PVWM than in cerebral cortex in both frontal (5 ± 1 mL/min/100g; $p<0.001$) and parietal PVWM (5 ± 1 mL/min/100g; $p<0.02$).

Cerebral cortical and subcortical gray matter were less vulnerable to ischemic injury than the PVWM.

Figure 3 shows representative histopathological findings for early PVWM lesions identified at 24 h after an ischemic insult of 30, 37 or 45 min duration with the microglial/macrophage markers, isolectin B4 or Ham 56. Although 30 min of ischemia infrequently generated small focal lesions (data not shown), two types of PVWM lesions were commonly identified at 37 and 45 min (Fig. 3A, B and supplemental Fig. 1). Focal lesions contained numerous reactive microglia and phagocytic macrophages visualized with both isolectin B4 and Ham 56. Diffuse white matter lesions mostly contained numerous reactive microglia. After 37 min of ischemia, PVWM lesions were typically more circumscribed and accompanied by limited gray matter injury. However, after 45 min of ischemia, PVWM lesions were more extensive and accompanied by significant lesions in the superficial white matter (Fig 3C). In addition, large lesions in the basal ganglia (Fig. 3B) and cerebral cortex (Fig. 3D) were common.

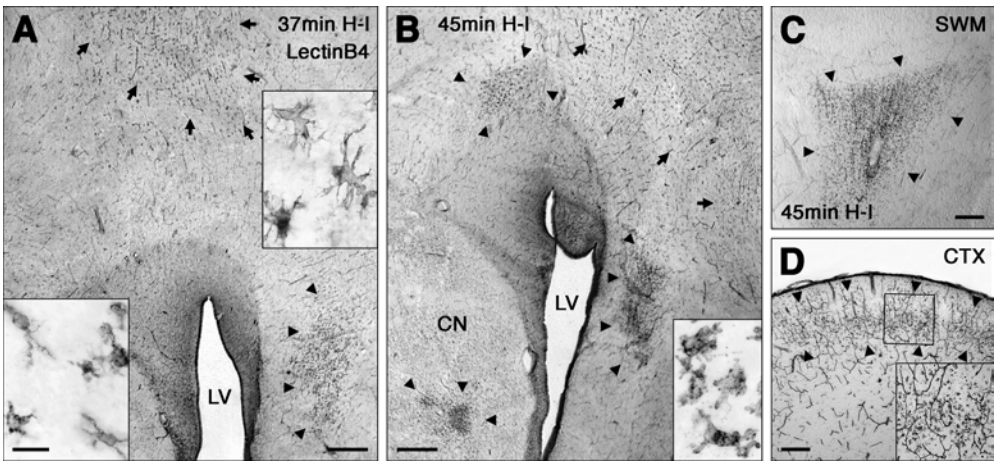

Figure 3. Histopathological features of PVWM lesions generated after global ischemia of 37 or 45 min duration, as visualized with isolectin B4. *A*, After 37 min of ischemia, activated microglial were localized to a lesion at the apex of the lateral ventricle (arrows). The typical morphology of the activated microglia is shown in the inset at upper right. The inset at lower left shows the typical morphology of ramified microglia and resting macrophages in control PVWM. A focal collection of reactive macrophages/microglia localized to the lateral body of the corpus callosum (arrowheads). *B*, After 45 min of ischemia, activated microglia were diffusely localized to a lesion at the external angle of the lateral ventricle (arrows). Focal collections of reactive phagocytic macrophages/microglia localized to medial and lateral regions in the PVWM (arrowheads). The typical morphology of the reactive phagocytic macrophages is shown in the inset at lower right. Note the presence of a focal lesion in the caudate nucleus (CN) (arrowheads). *C*, *D*, After 45 min of ischemia, large lesions were also generated in the superficial white matter (SWM; panel C, arrowheads) and in the cerebral cortex (D, arrowheads). A detail of the cortical lesion is shown in the inset. Scale Bars: *A*, *B*, 500 μm; *C*, *D*, 300 μm; insets in A, B, 30 μm.

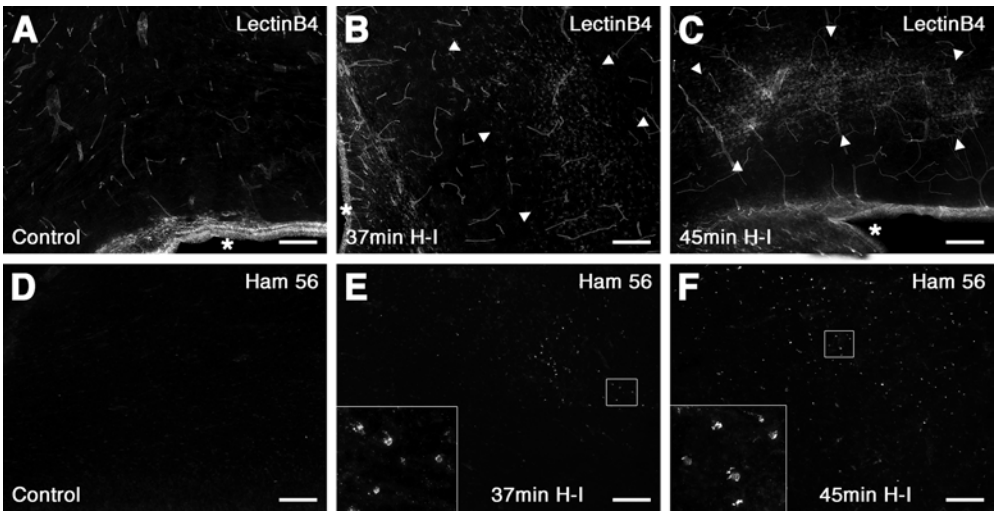

Supplemental Figure 1. Focal PVWM lesions contain activated microglia and phagocytic macrophages identified with isolectin B4 or Ham 56. Panels *A-C* show higher power details of immunofluorescent staining for isolectin B4 in the control PVWM (A) relative to PVWM lesions (arrowheads) generated after 37- (B) or 45-min (C) of ischemia. Microglia/macrophage-rich

lesions were also confirmed using a Ham 56 antibody (D-F). Asterisk denotes apex of lateral ventricle. Scale Bars: *A-F*, 200 μm.

Distribution of cerebral lesions identified by TUNEL staining

In order to quantify cell degeneration in the PVWM, we first determined the survival time after ischemia when TUNEL staining was greater. We determined the mean density of TUNEL-labeled nuclei from frontal or parietal lesions in animals that survived for 24 or 72 h after 30 or 45 min of ischemia. Animals that survived for 24 h consistently had a higher mean TUNEL density in both the PVWM and cerebral cortex compared to survival for 72 h (supplemental figure 2).

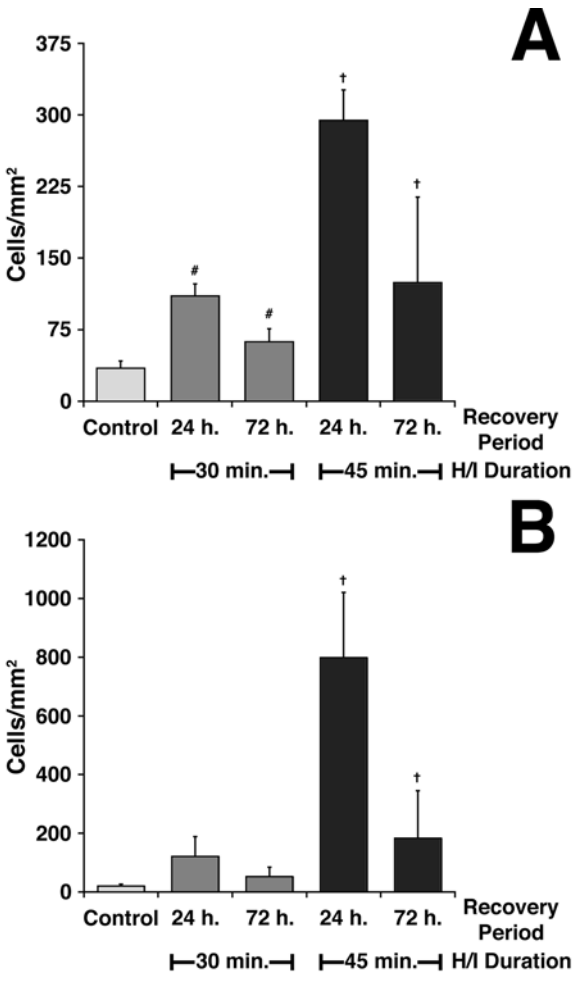

Supplemental Figure 2. Time course for appearance of TUNEL-labeled nuclei in frontal PVWM (A) and cerebral cortex (B) after 30 or 45 min of global ischemia (n=4 animals per group at 24 h or 72 h survival). The density of TUNEL-labeled nuclei was consistently higher 24 h after global ischemia than after 72 h. In A, B, # $p<0.001$, 30 min H/I 24 *vs*. 72 h recovery; † $p<0.05$, 45 min H/I 24 *vs*. 72 h recovery: unpaired two-tailed t tests.

We next generated frequency maps of the distribution of TUNEL-labeled nuclei in frontal and parietal lesions from animals that survived for 24 h after 30 (n=4), 37 (n=4) or 45 min (n=4) of ischemia (Fig. 4). In these maps, the frequency of a lesion in any location is designated by color, with no overlap in the location of lesions among animals depicted in green and the most overlap in red. After 30 min of ischemia, injury to frontal (Fig. 4B) and parietal (Fig. 4F) PVWM was

limited and infrequently detected. After 37 min of ischemia, greater PVWM injury was consistently generated (Figs. 4C,G, I; yellow-to-red regions). In most animals, lesions were infrequently detected in superficial white matter, cortical gray matter or SVZ. One exception was a predilection for neuronal injury in both frontal and parietal deep cortex. In addition, superficial white matter lesions occurred at the depth of the cortical gyrus adjacent to the most vulnerable region of the PVWM. Small discrete or confluent lesions of the caudate nucleus were detected in all animals. Hippocampal lesions were not detected.

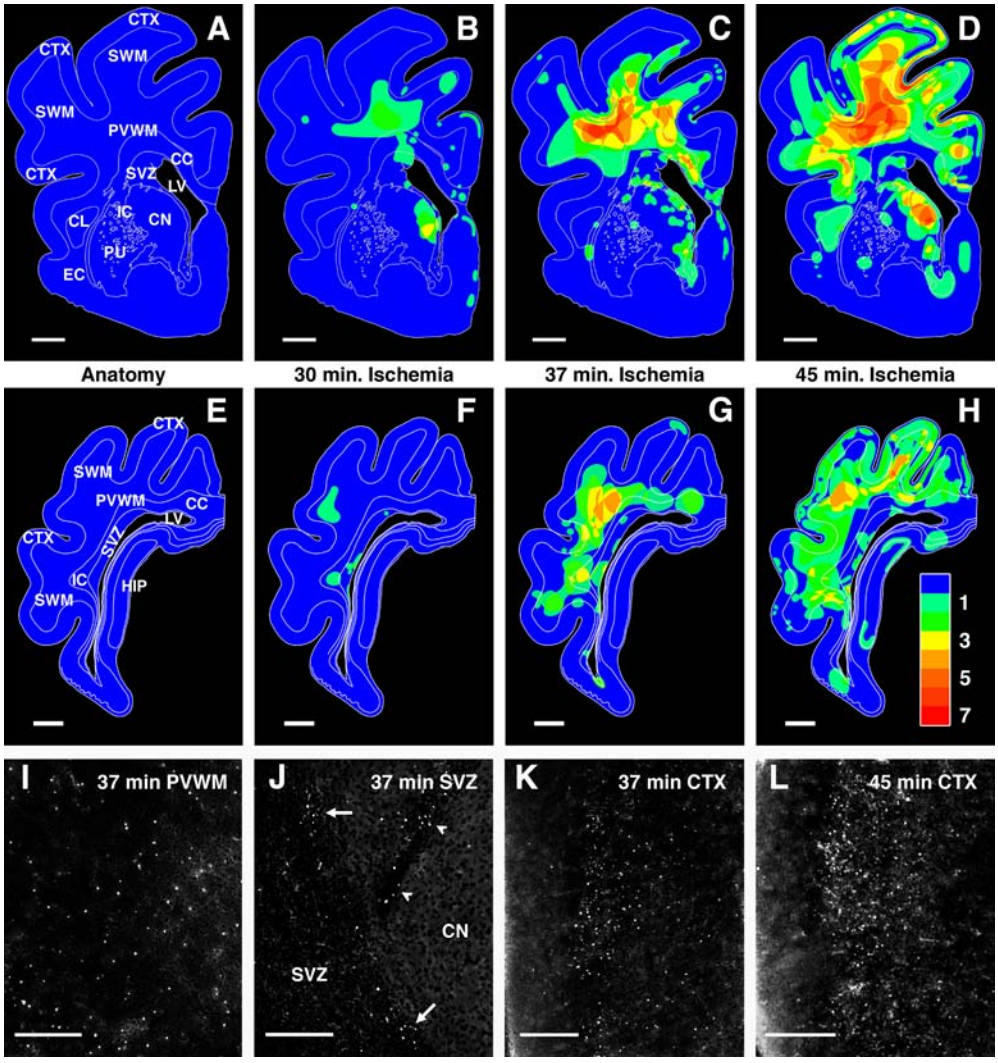

Figure 4. Regional distribution of TUNEL-labeled nuclei in cerebral lesions at 24 h after 30, 37 or 45 min of global ischemia. Panels A and E show major anatomical structures (see abbreviations, below) at frontal and parietal levels of the PVWM. Panels B-D and F-H show composite pseudo-color TUNEL maps of the distribution of TUNEL-labeled nuclei plotted in two sections from each of four animals. The pseudo-color probability scale (1-7) in H indicates the number of sections in which overlapping lesions were found for any given region. Note that at 30 and 37 min, cerebral injury was mostly restricted to cerebral white matter. However, at 45 min, injury to the cerebral cortex and basal ganglia greatly increased, but

the SVZ and hippocampus remained relatively spared. Panels I-L show representative examples of the magnitude and distribution of TUNEL-labeled nuclei in cerebral lesions after either 37 min (I-K) or 45 min (L) of ischemia. *I*, Large numbers of TUNEL-labeled nuclei were typically localized to the PVWM even after 37 min of ischemia. *J*, Within the SVZ, TUNEL-labeled nuclei typically localized to the dorsal extent of the SVZ (arrows) and to small extensions of the SVZ (arrowheads) into the adjacent caudate n. (CN). *K*, Focal cortical lesions were uncommon after 37 min of ischemia. *L*, Large cortical lesions were common after 45 min of ischemia, and contained a high density of TUNEL-labeled nuclei. Abbreviations: CC, corpus callosum; CD, caudate nucleus; CL, claustrum; EC, external capsule; HIP, hippocampus; IC, internal capsule; LV, lateral ventricle; PU, putamen; SWM, superficial white matter. Scale Bars: A-H, 2mm; I-L, 200μm.

After 45 min of ischemia, cerebral lesions were more extensive (Fig. 4D, H, L). Confluent lesions were commonly observed that involved both the PVWM and the superficial white matter. There was a striking increase in the extent of neuronal injury to both the cerebral cortex and the basal ganglia. Interestingly, large confluent lesions of the caudate nucleus were observed in all animals, whereas the putamen and SVZ were mostly spared. Lesions were also uncommon in the hippocampal formation (Fig. 4H). Thus, prolonged ischemia generated pronounced injury to both cerebral gray and white matter structures. However, cerebral ischemia of 37 min duration generated mostly selective injury to the PVWM.

Graded PVWM injury was proportional to the duration of global ischemia.

We next quantified the density of TUNEL-labeled nuclei in frontal PVWM lesions from animals that survived for 24 hours after 30 (n=4), 37 (n=5) or 45 min (n=4) of ischemia compared to control (n=5). Consistent damage of graded severity was generated between 30 to 45 min. After 30 min, the density of TUNEL-labeling in frontal PVWM was significantly increased (110 ± 13 nuclei/mm^2) versus control (35 ± 7; $p<0.001$; one-way ANOVA with post hoc Bonferroni). The density of TUNEL-labeled nuclei in the PVWM increased to 151 ± 17 nuclei/mm^2 after 37 min of ischemia and to 294 ± 32 nuclei/mm^2 after 45 min ($p<0.05$; 37 vs. 45 min). Likewise, in frontal cortical lesions, mean TUNEL densities increased from 185 ± 60 after

37 min ischemia to 798 ± 223 nuclei/mm^2 after 45 min ($p<0.05$; 37 vs. 45 min). Similarly, TUNEL density in the caudate nucleus increased from 227 ± 26 at 37 min to 723 ± 235 nuclei/mm^2 at 45 min ($p<0.05$).

We next compared the relative vulnerability of the PVWM relative to frontal cerebral cortex, caudate nucleus and the SVZ by analyzing TUNEL-labeled cells as a percentage of total cells in each region (Figure 5). Relative to the other regions, the PVWM displayed the most significant injury at 30 min and 37 min of ischemia. After 45 min, the magnitude of injury markedly increased in a non-linear fashion, and there was a pronounced similar increase in gray and white matter injury.

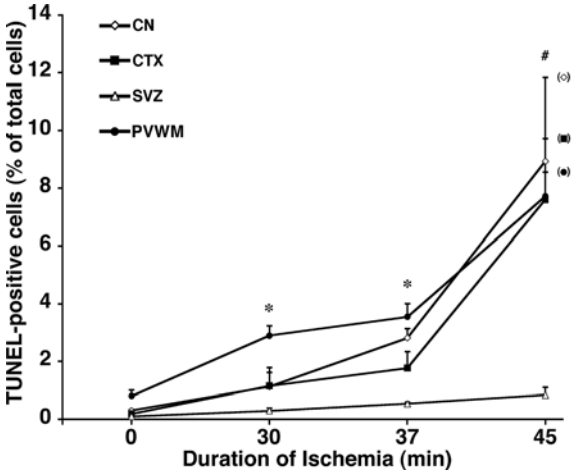

Figure 5. Regional heterogeneity of cerebral injury at 24 h after cerebral ischemia of 30, 37 min or 45 min duration relative to control. Cell degeneration in the PVWM was compared with that in the CTX, CN and SVZ by quantification of TUNEL-labeled cells as a percentage of total cells in each region. *$p<0.05$ (PVWM vs. CTX; LSD test); # indicates not significant (NS).

Differential vulnerability of glia in severe white matter lesions.

To determine the origin of degenerating nuclei in PVWM lesions from animals that survived for 24 h, we did immunohistochemical double-labeling studies for TUNEL and cell type-specific markers. In agreement with prior studies (Falkowski et al., 2002), programmed cell death was very low throughout the control cerebral white matter. When detected, these rare TUNEL-labeled nuclei typically double-labeled with the O1 monoclonal antibody but not with antibodies against GFAP, vimentin or isolectin B4.

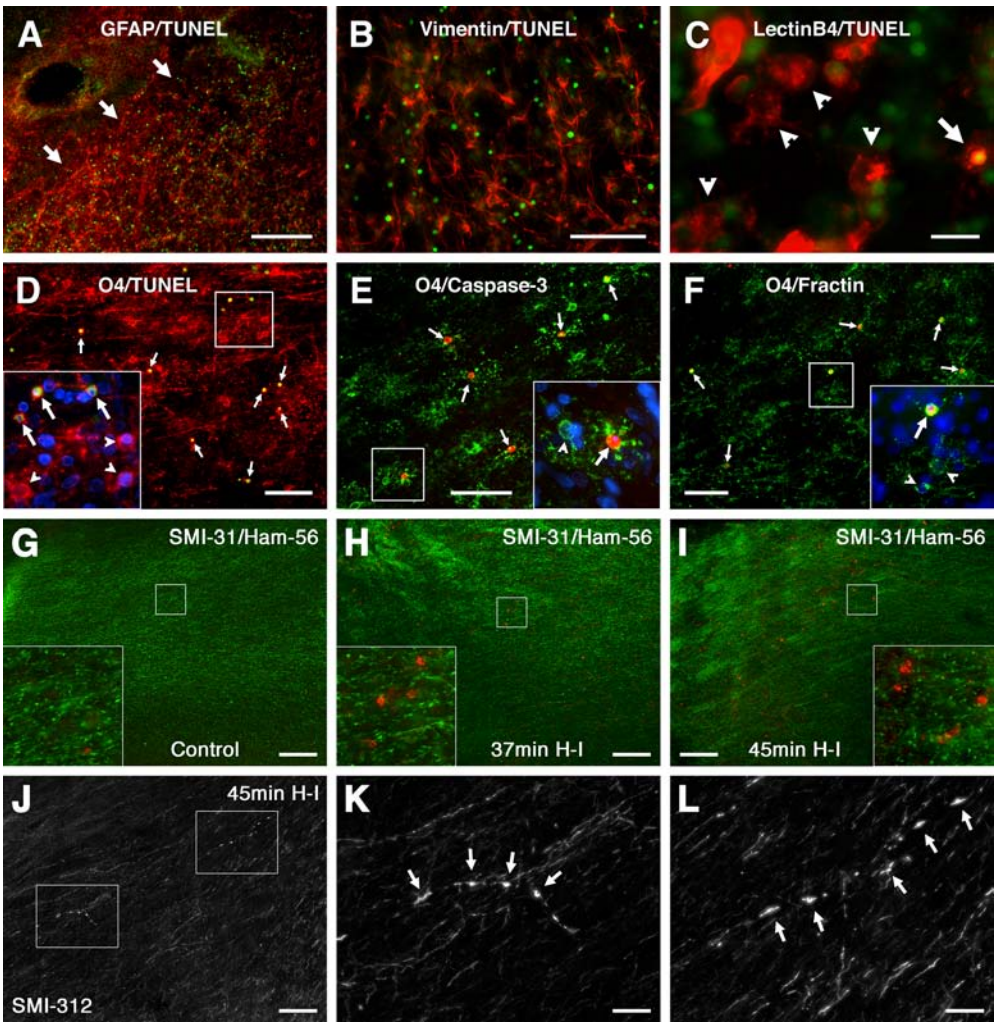

Figure 6. Differential vulnerability of glia and axons in PVWM lesions at 24 h after ischemia. Although astrocytes and microglia appeared mostly resistant to injury from prolonged ischemia (45 min; A-C), numerous degenerating OL precursors were detected after more mild ischemia (37 min; D-F). Axons were also mostly resistant to prolonged ischemia (G-L). *A*, A lesion with numerous astroctyes visualized by staining for GFAP (red; arrows) that did not overlap with TUNEL-labeled nuclei (green). *B*, A higher power image shows intact-appearing vimentin-labeled astrocytes (red) that did not co-localize with TUNEL-labeled nuclei (green). *C*, Most isolectin B4-labeled microglia/macrophages (red) were TUNEL-negative (arrowheads), but an occasional shrunken TUNEL-labeled cell appeared to be degenerating (arrow). *D*, A low-power image where many degenerating O4+ cells (red) double-labeled for TUNEL (green; arrows). *D inset*, High power image shows several degenerating O4+ cells (arrows) with pyknotic Hoechst 33324-labeled nuclei (blue) that also labeled with TUNEL. Note the intact cells with normal-appearing nuclei (arrowheads). *E*, Low-power image in which many degenerating O4+ cells (green) labeled for activated caspase-3 (red; arrows). *E inset*, A triple-labeled high-power image shows a degenerating O4+ cell (arrow) that labeled for activated caspase-3 (red) and had a pyknotic Hoescht-labeled nucleus (blue). An intact cell (arrowhead) did not label for activated caspase-3. *F*, A low power image of O4+ cells (green) where degenerating cells labeled with the fractin antibody (red). *F inset*, shows a degenerating cell that labeled with fractin (arrow). Intact cells had normal-appearing nuclei (arrowheads). *G-I*, Low power images of SMI-312-labeled

axons (green) and Ham 56-labeled microglia/macrophages (red) in the PVWM from control (G), and animals subjected to 37 min (H) or 45 min (I) of ischemia. Note the increased labeling for Ham 56 in the ischemic animals relative to control (insets), but the similar axonal staining pattern for all conditions. *J*, Apparent degenerating axons were rarely detected in the PVWM after prolonged ischemia (45 min). *K, L*, higher power images of the axons in the boxes in J. Note that the degenerating axons had a fragmented staining pattern and focal swellings (arrows). Scale Bars: *A*, 200 μm; *B* 100μm; *C*, 20 μm; *D*, *E*, *F*, 100 μm. *G-J, 100* μm; K, L, 25 μm.

After prolonged ischemia (45 min, n=4), astrocytes visualized with GFAP or vimentin appeared intact and did not double-label with TUNEL (Fig. 6A, B). Similarly, microglia and reactive macrophages rarely labeled with TUNEL (Fig. 6C). As recently reported in early human PWMI lesions (Back et al, 2005, Haynes et al., 2003), degenerating astroglia and microglia were rarely detected in ovine white matter lesions after severe ischemia, which suggests that the vulnerability of these cell types is low at this time in development.

In contrast to other glial cell types, many TUNEL-labeled nuclei co-localized with the O4 antibody, a marker of preOLs and immature OLs (Fig. 6D). The degenerating O4-labeled cells were commonly visualized in animals that sustained 37 min of ischemia and were also present at much lower density in mild lesions after 30 min of ischemia. Since the nuclei of these degenerating O4-labeled cells often appeared condensed or fragmented when visualized with Hoechst 33324 (Fig. 6D, inset), we determined whether some of these cells might be degenerating via a caspase-dependent mechanism. We commonly visualized degenerating O4-labeled cells that double-labeled for activated caspase-3 (Fig 6E). Caspase-activation was confirmed in these cells by co-localization of the O4 antibody with the fractin antibody that detects caspase-cleaved fragments of actin (Fig. 6F).

Axonal elements were mostly resistant to ischemic injury in severe white matter lesions.

To determine the susceptibility of axons to degeneration with increasing duration of ischemia, we first visualized SMI 31, an antibody against heavily phosphorylated neurofilament proteins,

together with Ham 56 to identify white matter lesions. At survival times of 24 or 72 h, no degenerating axons were detected after 37 (n=4) or 45 min (n=4) of ischemia relative to controls in frontal cerebral white matter (Fig. 6G-I). However, using SMI 312, an antibody used to define axonal maturation in human fetal brain (Ulfig et al., 1998; Back et al., 2002a), we detected rare degenerating axons in the PVWM of one of four animals subjected to prolonged ischemia (45 min). Degenerating axons displayed more intense staining, focal swellings and a fragmented staining pattern (Fig 6J-L).

Differences in the OL maturational state were related to differential susceptibility to ischemic injury in the PVWM.

Since OL lineage maturation was significantly less advanced in the PVWM*m* than in the PVWM*l*, we hypothesized that regional maturational differences would manifest as different degrees of susceptibility to ischemia. First, we established that the overall density of degenerating cells was very similar in selective white matter lesions (PVWM*m* and PVWM*l* combined) when TUNEL density (151 ± 9; mean ± SE, n=5) was compared with the density of degenerating O4-labeled cells (158 ± 21, n=4) after 37 min of ischemia. Hence, cell death in white matter lesions was mostly accounted for by the number of degenerating O4-labeled cells.

When we compared the percentage of degenerating O4-labeled cells in the PVWM*m* (Fig. 7A, B) and PVWM*l* (Fig. 7C, D), we found that cell death was markedly higher in the PVWM*m*. In the PVWM*l*, many more intact-appearing cells were visualized. In fact, O4-labeled myelinating cells typically showed no features of degeneration (Fig. 7D, red arrows). There were ~3-fold more degenerating O4-labeled cells in the PVWM*m* (27 ± 1%) versus only 8 ± 2% in the PVWM*l* (Fig. 7E; $p<0.001$). Moreover, relative to control, there was a significant ~2-fold greater reduction in the total density of O4-labeled cells in the PVWM*m* (496 ± 10 vs. 293 ± 7)

compared to the PVWM*l* (471 ± 9 vs. 369 ± 6; p<0.01, Fig. 7F). Hence, there was a significant depletion of O4-labeled cells during the initial phase of ischemic white matter injury that was particularly pronounced in the PVWM*m* where preOLs predominated.

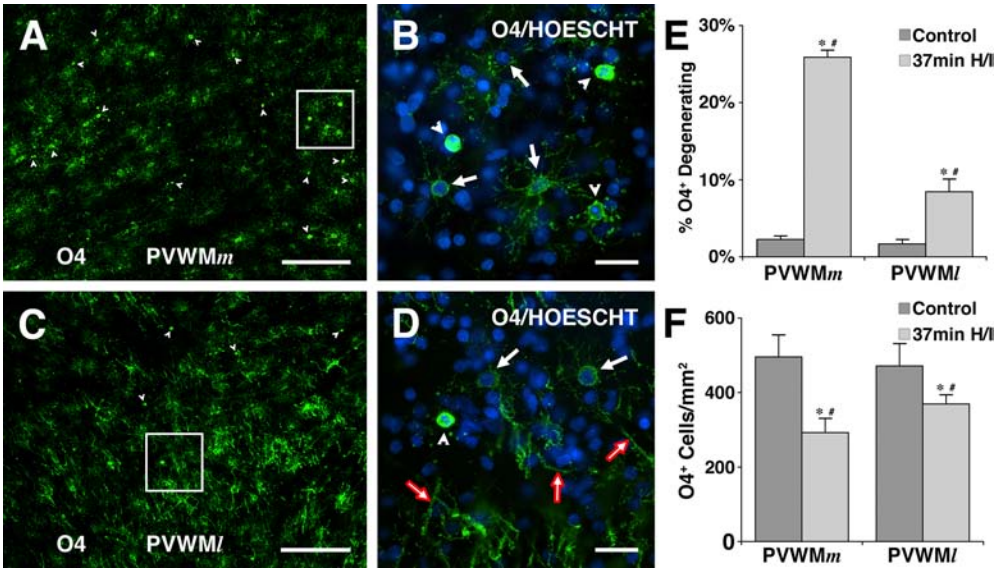

Figure 7. Differential injury in two adjacent regions of the PVWM, the PVWM*m* and PVWM*l*, coincides with the extent of preOL degeneration. A, Many degenerating O4-labeled cells (arrowheads) localized to the PVWM*m*. Note the lack of early myelination in this region. B, High power image that corresponds to the inset in A shows typical degenerating cells with pyknotic Hoechst-labeled nuclei (arrowheads). Intact O4-labeled cells are indicated (arrows). C, The low power distribution of O4-labeled cells and early-myelinated axons in the PVWM*l*. Note that most pre-myelinating cells localized to the border of the myelinated tract, where occasional pyknotic cells (arrowheads) were observed. D, High power image that corresponds to the inset in C shows a degenerating cell (arrowhead) and adjacent intact cells (arrows). Several myelinated axons are indicated (red arrows). E, The percentage of total OLs degenerating at 24 h after ischemia. The PVWM*m* had a markedly higher (26 ± 1%) percentage of cells that degenerated than the PVWM*l* (8 ± 2%). F, The total density of 04-labeled cells at 24 h after ischemia relative to control in the PVWM*m* and PVWM*l*. Note that the total density of OL lineage cells, defined by labeling with the O4 antibody, was very similar in the control PVWM*m* and PVWM*l*. A significant loss of O4-labeled cells of ~40% occurred in the PVWM*m* while the number of cells in the PVWM*l* decreased by only ~20%. In E, F, * p<0.001 for control vs. 37 min ischemia; # p<0.01 for ischemia PVWM*m* vs. PVWM*l*: unpaired two-tailed t tests. Scale Bars: A, C, 200 μm; B, D, 25 μm.

Blood flow in the PVWM*m* and PVWM*l* were equivalent.

Since we found the magnitude of ischemic damage to the PVWM*m* and PVWM*l* to differ significantly, we determined if the difference in susceptibility of these adjacent regions might be

accounted for by intrinsic differences in cerebral blood flow (Fig. 8). Under basal conditions (n=8), blood flow to the PVWM*m* (32 ± 4 mL/min/100g) and PVWM*l* (33 ± 4) was equivalent. During ischemia (n=7), blood flow decreased similarly to 4 ± 1 mL/min/100g in the PVWM*m* and 6 ± 1 in the PVWM*l*. Even after prolonged ischemia of 45 min duration, at both 15 (n=5) and 60 min (n=7) of reperfusion there were no significant differences in cerebral flow between these two regions. Hence, the differences in susceptibility of the PVWM*m* and PVWM*l* to ischemic damage were related to differences in the maturational state of the OL lineage stages present in these adjacent regions of the PVWM.

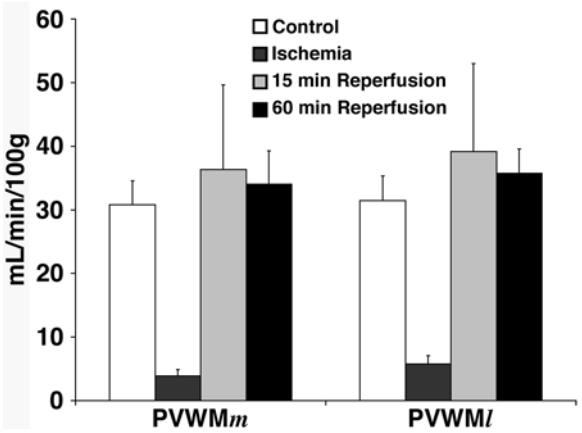

Figure 8. *In situ* quantification of cerebral blood flow by digital dissection of microsphere density in the PVWM*m* and PVWM*l*. No significant differences in blood flow between the PVWM*m* and PVWM*l* were detected under conditions of basal flow (n=8), ischemia (n=7), or at 15 min (n=5) or 60 min (n=7) of reperfusion. During ischemia, blood flow decreased to similar levels of 14 ± 9% of basal in the PVWM*m* and 17 ± 11% in the PVWM*l*. After 15 min of reperfusion, there was a modest hyperemia in both the PVWM*m* and PVWM*l*. By 60 min, blood flow returned to near basal levels again in the PVWM*m* and PVWM*l*.

DISCUSSION

We developed a fetal model that yielded the following findings in support of a significant role for ischemia-reperfusion injury in PWMI: (1) Graded white matter injury was generated that was proportional to the duration of ischemia. (2) Selective white matter injury ranged from discrete focal lesions to diffuse injury similar to early PWMI. (3) The PVWM displayed a lower threshold for injury than cortical or subcortical gray matter or SVZ. (4) Lower blood flows occurred in PVWM than in cerebral cortex but did not account for the distribution of white matter damage. (5) The distribution of white matter injury coincided with greater immaturity of the OL lineage stages present in vulnerable regions of PVWM. (6) Selective white matter injury spared most glial cell types and primarily involved pre-myelinating stages in the OL lineage.

We took several departures from prior approaches (Penning et al., 1994; Mallard et al., 1998; Reddy et al., 1998; Matsuda et al., 1999; Raad et al., 1999; Petersson et al., 2002), to develop a model of selective PVWM injury. To identify potential target populations of preOLs, we defined OL lineage maturation in the immature ovine brain. As in preterm human PVWM (Back et al., 2001), there were distinct regions of ovine PVWM where at-risk preOLs predominated. Secondly, by varying the duration of ischemia, we identified a threshold where brain injury transitioned from predominantly PVWM injury to extensive cerebral injury. Thirdly, we combined cell-type-specific and cell death markers to define the relative susceptibility of glia and axons under conditions of prolonged ischemia.

Immature ovine ischemia reproduced histopathological features of early PWMI.

The principal pathologic features of late PWMI range from focal cystic necrosis (PVL) to diffuse myelination disturbance with gliosis (Kinney and Back, 1998). How these late lesions relate to early PWMI lesions is unclear. We recently described a range of histopathological features in

human early PWMI (Back et al., 2005). The principal features were diffuse lesions in the PVWM that contained activated microglia and focal lesions rich in phagocytic macrophages. We similarly generated early ovine PVWM lesions that ranged from focal to diffuse lesions rich in microglia/macrophages. Although PWMI is often characterized by selective injury, in more severe forms it may coexist with cortical or subcortical gray and white matter injury (Kinney and Back, 1998). With more prolonged ischemia, we generated diffuse PVWM injury that was accompanied by lesions in gyral white matter, cerebral cortex and basal ganglia. Similar lesions were detected after repeated systemic fetal endotoxin exposure (Duncan et al., 2002; Dalitz et al., 2003).

Role of cerebral ischemia in PVWM injury

In the immature fetus, shorter periods of ischemia than employed here caused damage primarily to subcortical white matter (Mallard et al., 1998; Raad et al., 1999). PVWM lesions were infrequently detected in mid-gestation models of hypoxemia where a restriction in uteroplacental blood flow resulted in decreased oxygen delivery and mild acidemia to the fetus without systemic hypotension or cerebral hypoperfusion (Rees et al., 1997; Mallard et al., 1998; Rees et al., 1999). Systemic fetal endotoxin exposure that triggered transient hypoxemia and hypotension generated superficial and PVWM lesions (Duncan et al., 2002; Dalitz et al., 2003). We found that selective white matter injury was lost with more prolonged ischemia. In fact, prolonged ischemia (>45 min) was associated with extensive cystic necrotic encephalomalacia (data not shown) as seen in severe human PVL (Marin-Padilla, 1997, 1999). Focal necrotic white matter lesions were similarly generated in response to hemorrhagic hypotension (Matsuda et al., 1999) that caused an acute decrease in cerebral blood flow of about 30% in a similar model (Szymonowicz et al., 1990). Hence, the neuropathological similarities of our model to human

PWMI supports the notion that human PVWM may be particularly vulnerable to global cerebral hypoperfusion (Volpe, 2001).

Quantification of cerebral blood flow (CBF) in developing brain

We undertook an integrated analysis of CBF disturbances in regions of PVWM where OL lineage susceptibility was defined. Even large differences in flow in small regions can be obscured when averaged with larger unaffected regions, as is the case with more global measures of CBF. This is the first quantitative study of CBF in situ achieved through digital dissection of CBF in anatomically defined regions using fluorescently-labeled microspheres. Fluorescent microspheres have replaced radioactive microspheres in many laboratories and there is a high correlation of flows determined by radio- and fluorescent-labeled microspheres (Glenny et al., 1993; Bernard et al., 2000). Under basal conditions, our blood flow measurements in white and gray matter agreed closely with those obtained with radioactive microspheres (Szymonowicz et al., 1988; Gleason et al., 1989; Szymonowicz et al., 1990).

Previous studies with this global hypoperfusion model in immature fetal sheep did not measure CBF (Reddy et al., 1998). We found PVWM flows under both basal and ischemic conditions were lower than in cerebral cortex. Although CBF in both regions fell proportionally to ~15% of basal flow during ischemia, in absolute units PVWM flow was very low relative to the cortex. PVWM flow, thus, may have fallen below a critical threshold for hypoxic-ischemic damage, which may explain the overall greater susceptibility of PVWM relative to the better-perfused cerebral cortex.

Role of susceptible preOLs in the pathogenesis of PVWM lesions.

While global ischemia was necessary for PVWM injury, no regional differences in blood flow were found between the PVWM*m* and PVWM*l* under any conditions to account for the disparate

rates of cellular degeneration in these regions. Our data provide the first evidence that regional differences in PVWM injury were related primarily to the maturational state of the OL lineage rather than to heterogeneity of PVWM flow. Although preOLs are particularly susceptible to hypoxia-ischemia, their susceptibility in PVWM had not been addressed. Almost all cell degeneration seen in ovine PVWM lesions was accounted for by OL lineage degeneration. Conditions that produced significant preOL degeneration, caused limited injury to adjacent gray matter structures. This was unexpected, because in perinatal rodents preOL degeneration in white matter was accompanied by extensive cortical-neuronal degeneration (Back et al., 2002b) and substantial SVZ lesions (Levison et al., 2001; Plane et al., 2004). Selective degeneration of preOLs in ischemic ovine PVWM is consistent with human studies that OL progenitors are depleted in early PVWM lesions that sustain pronounced oxidative damage (Haynes et al., 2003; Back et al., 2005). Moreover, the PVWM of near term sheep demonstrates increasing developmental resistance to ischemic injury (Penning et al, 1994; Reddy et al., 1998). Future studies are needed to define the role of acute preOL degeneration in chronic myelination disturbances. Since OL progenitors have other potential fates in gliogenesis and neurogenesis (Kondo and Raff, 2000; Belachew et al., 2003), it will be of interest to determine other potential roles of these cells in white matter regeneration and repair.

Another unexpected difference between perinatal rodents and fetal sheep is the predominant mechanism of preOL death. In a perinatal rodent model of hypoxia-ischemia, the majority of preOLs degenerated by a mechanism that did not involve apparent caspase-3 activation (Back et al., 2002b). By contrast, ovine preOL degeneration commonly involved activation of caspase-3. Similar observations were made in late-gestation sheep (Cao et al., 2003; Castillo-Melendez et al., 2004). We speculate that the severity of the insult in our fetal model

may be less than that sustained in perinatal rat models and, thus, favors a greater degree of apoptotic death. However, the relative extent of apoptotic and necrotic preOL degeneration remains to be determined.

Clinical Implications

Although premature infants display a particular predilection for PWMI, recent studies support a widening spectrum of pathology associated with this injury that includes PVL and diffuse myelination disturbances characterized by reactive gliosis. One frequent sequela of PWMI in chronic survivors of premature birth is volume loss of cortical and deep nuclear gray matter (Inder et al., 2005). The neuropathological basis for these reductions in gray matter volume is unknown. Although small and discrete, we observed that lesions to the caudate nucleus were the most consistently observed gray matter pathology seen in association with moderate ischemia. By contrast, ovine cerebral cortex was relatively resistant to ischemia-reperfusion injury that damaged PVWM. Our data suggests that significant cortical and subcortical volume loss may arise in the setting of more severe ischemia and that there is a narrow threshold for a nonlinear increase in neuronal injury. Future studies are needed, however, to determine whether cortical or deep nuclear volume loss is related to delayed neuronal death, axonal degeneration or depletion of subplate neurons or neural stem cells. In perinatal rats, subplate neurons are markedly more susceptible to hypoxia-ischemia than other neuronal populations (McQuillen et al., 2003), but we rarely detected degenerating cells in the ovine subplate. We also detected limited damage to SVZ progenitors.

Our data predicts that those infants with earlier or more extensive OL differentiation and myelination would be less susceptible to PWMI. In fact, a more variable degree of white matter injury was detected in near term sheep after several insults (Clapp III et al., 1988; Penning et al.,

1994; Mallard et al., 1998; Ikeda et al., 1999; Ohyu et al., 1999; Raad et al., 1999). Future studies are needed to determine whether acceleration of OL differentiation might be a feasible strategy to reduce the incidence and severity of PWMI.

CHAPTER 2

HISTOPATHOLOGICAL CORRELATES OF MRI-DEFINED CHRONIC PERINATAL WHITE MATTER INJURY

Art Riddle, B.S.[1], Justin Dean, Ph.D.[1], Joshua R. Buser, B.S.[1], Xi Gong, M.D.[1], Jennifer Maire, B.S.[1], Kevin Chen, B.S.[1], Tahir Ahmad, B.S.[1], Victor Cai[1], Thuan Nguyen, Ph.D.[2], Christopher D. Kroenke, Ph.D.[3,4,5], A. Roger Hohimer, Ph.D.[6] and Stephen A. Back, M.D., Ph.D.[1,7]

From the Departments of Pediatrics[1], Public Health and Preventive Medicine,[2] Behavioral Neuroscience[3], the Advanced Imaging Research Center[4], the Oregon National Primate Research Center[5], Obstetrics and Gynecology[6], and Neurology[7] Oregon Health & Science University, Portland, Oregon.

Riddle A, Dean J, Buser J, Gong X, Maire J, Chen K, Ahmad T, Chen V, Nguyen T, Kroenke C, Hohimer A, Back S (2011) Histopathological correlates of MRI-defined chronic perinatal white matter injury. Annals of Neurology; Epub ahead of print.

ABSTRACT

Although MRI is the optimal imaging modality to define cerebral white-matter injury (WMI) in preterm survivors, the histopathological features of MRI-defined chronic lesions are poorly defined. We hypothesized that chronic WMI is related to a combination of delayed oligodendrocyte (OL) lineage cell death and arrested maturation of pre-oligodendrocytes (preOLs). We determined whether *ex vivo* MRI can distinguish distinct microglial and astroglial responses related to WMI progression and arrested preOL differentiation. We employed a preterm fetal sheep model of global cerebral ischemia where acute WMI results in selective preOL degeneration. We developed novel algorithms to register histo-pathologically defined lesions with contrast- and diffusion-weighted high-field *ex vivo* MRI data. Despite mild delayed preOL degeneration, preOL density recovered to control levels by 7 days after ischemia and was ~2 fold greater at 14 days. However, pre-myelinating OLs were significantly diminished at 7 and 14 days. WMI evolved to mostly gliotic lesions where arrested preOL differentiation was directly proportional to the magnitude of astrogliosis. A reduction in cerebral WM volume was accompanied by four classes of MRI-defined lesions. Each lesion type displayed unique astroglial and microglial responses that corresponded to distinct forms of necrotic or non-necrotic injury. High-field MRI defined two novel hypo-intense signal abnormalities on T_2-weighted images that coincided with microscopic necrosis or identified astrogliosis with high sensitivity and specificity. These studies support the potential of high-field MRI for early identification of microscopic necrosis and gliosis with preOL maturation arrest, a common form of WMI in preterm survivors.

ACKNOWLEDGEMENTS

Supported by the NIH (P51RR000163 (CDK); National Institutes of Neurological Diseases and Stroke: 1RO1NS054044, R37NS045737-06S1/06S2 to SAB and 1F30NS066704 to AR) a Bugher Award from the American Heart Association (SAB) and the March of Dimes Birth Defects Foundation (SAB). High-field MRI instrumentation used in this work was purchased with support from the W.M. Keck Foundation.

INTRODUCTION

Cerebral white matter injury (WMI) is the most common cause of chronic neurological disability in children with cerebral palsy.(Bax et al., 2006) Survivors of premature birth are at particular risk for WMI, which results in disrupted WM maturation and chronic myelination disturbances.(Volpe, 2008) Advances in neonatal neuro-imaging have identified a pronounced shift in the features of WMI defined by conventional (T_1- and T_2-weighted) and diffusion-weighted MRI. Whereas, the cystic-necrotic lesions of periventricular leukomalacia (PVL) were previously the most common, the incidence of PVL has markedly declined,(Hamrick et al., 2004) and a new form of chronic WMI has emerged as defined by MRI, dominated by focal or diffuse non-destructive lesions.(Counsell et al., 2003; Inder et al., 2003; Miller et al., 2003; Ment et al., 2009) However, controversy exists regarding the extent to which necrotic injury contributes to chronic human WMI.(Volpe, 2008) Although there is a significant incidence of microscopic lesions seen at autopsy, these lesions are not readily detected by MRI in clinical studies.(Pierson et al., 2007) Hence, the extent to which necrotic injury contributes to the overall burden of WMI is unclear. Moreover, there appear to be many cases of WMI where necrosis is not seen in association with diffuse white matter gliosis. The clinic-pathological significance of these lesions is unclear, although such lesions coincide with preOL maturation arrest.(Segovia et al., 2008)

Critically ill preterm neonates appear susceptible to WMI after episodes of oxidative stress that selectively target susceptible pre-oligodendrocytes (preOLs)(Haynes et al., 2003; Back et al., 2005b) The spatial distribution of WMI is related to the relative density of susceptible preOLs and more resistant myelinating OLs.(Riddle et al., 2006) However, preOL degeneration in rodents was followed by rapid regeneration of preOLs that failed to differentiate in the astroglial

scar of chronic lesions.(Segovia et al., 2008) Growing evidence supports that arrested maturation of the OL lineage at the preOL stage is a central feature of myelination failure in both human perinatal WMI(Buser et al.) as well as adult demyelinating lesions and traumatic spinal cord injury.(Back et al., 2005a; Struve et al., 2005)

Although MRI is the optimal imaging modality to define WMI in preterm survivors,(Ment et al., 2009; Miller and Ferriero, 2009; Mathur et al., 2010; Rutherford et al., 2010) the histopathological features of particular MRI signal abnormalities have received limited study.(Inder et al., 2005b; Lodygensky et al., 2010; Lodygensky et al., 2011) To determine whether MRI can distinguish distinct cellular responses related to WMI progression and preOL maturation arrest, we developed novel algorithms to register histo-pathologically defined lesions with contrast- and diffusion-weighted high-field MRI data. We analyzed WMI in a clinically relevant large pre-clinical model, preterm fetal sheep that sustained global cerebral ischemia.(Reddy et al., 1998; Riddle et al., 2006) In this model, fetal sheep display cerebral hemodynamics and brain maturation similar to human(Hagberg et al., 2002; Back et al., 2006b; Ferriero, 2006) and develop acute WMI with preOL loss that closely resembles human.(Riddle et al., 2006; McClure et al., 2008)

Chronic WMI evolved to mostly gliotic lesions in which preOL arrest was directly proportional to the magnitude of astrogliosis. A reduction in cerebral WM volume was accompanied by four classes of MRI-defined lesions. Each type of lesion displayed unique astroglial and microglial responses that corresponded to distinct forms of necrotic or non-necrotic injury. A new hypo-intense signal abnormality was identified on T_2-weighted images that identified early gliotic lesions without necrosis. In addition, high-field T_2w-imaging identified microcyts that have been difficult to demonstrate at lower field. Although there was a

high incidence of microcysts, these lesions were infrequently observed in large regions of WMI and were not an essential feature of diffuse astrogliosis that was associated with preOL maturation arrest in our model. To our knowledge, lesions with these characteristics have not been previously reported, potentially as a result of limited study of perinatal WMI with static magnetic field strengths of greater than 3T. These studies support the potential of high-field MRI for early identification of gliosis with preOL maturation arrest, the major form of WMI in human preterm survivors.

MATERIALS AND METHODS

Animal surgical procedures. Surgery was performed on time-bred sheep of mixed western breed between 88–91d of gestation (term 145d) as previously described.(Riddle et al., 2006) Ewes with twin pregnancies were studied so that each experimental animal had a twin control. The ewe was initially anesthetized with intravenous ketamine (5 mg/kg) and diazepam (0.13 mg/kg), an endotracheal tube placed, and anesthesia maintained with 1% halothane in O_2 and N_2O. Maternal end tidal PCO_2 and oxygen saturation were monitored continuously. A midline laparotomy and a hysterotomy were performed in a sterile field and the fetus exposed. Vinyl catheters were placed in an axillary artery and a femoral vein. The vertebral-occipital arteries were isolated bilaterally and ligated with silk suture. In sheep, these anastomoses connect the vertebral arteries supplied by the thoracic aorta with the external carotid arteries that are fed by the brachiocephalic.(Baldwin and Bell, 1963) Hydraulic occluders (silastic) were placed on each fetal carotid artery. Finally, an amniotic fluid catheter was placed and one million units of penicillin G were given when the uterus was closed.

Physiological Monitoring. On the second or third post-operative day, at least 30 minutes prior to the start of the experiment, pressure transducers and a chart recorder (PowerLab 16/30, ADInstruments, Sydney, Australia) recorded pressure in the fetal artery relative to amniotic fluid (MABP). Fetal heart rate (HR) was calculated from triplicate measurements of the arterial pressure pulse intervals over a continuous recording of no less than 20 seconds.

Blood analysis. Blood samples (1 mL) taken anaerobically from the fetal axillary artery were analyzed for arterial pH_a, P_aO_2, P_aCO_2 corrected to 39°C, hemoglobin content (Thb), arterial oxygen saturation ($SatO_2$) and hematocrit (Hct; ABL725 blood gas analyzer, Radiometer

Medical A/S, Bronshoj, Denmark). After a 24 h recovery from surgery, fetuses were entered into the study if they demonstrated normal fetal oxygenation, defined as > 6 ml O_2/100 ml blood.

Cerebral Hypoperfusion Studies. Ischemia of 37 min duration was performed on the second or third post-operative day as previously reported.(Riddle et al., 2006) Briefly, sustained cerebral hypoperfusion was initiated by bilateral carotid artery occlusion after inflation and reestablished by deflation of the carotid occluders.*Tissue handling*. The ewe and fetuses were sacrificed (barbiturate overdose, Euthasol) at 1 (control, n=8; ischemia, n=8) or 2 (Control, n=6; ischemia, n=6) weeks following completion of the occlusion protocol. One 1-week experimental animal that developed extensive cystic necrotic injury was excluded from the study, making the final number studied 7. Fetal brains were immersion fixed at 4° C in 4% paraformaldehyde in 0.1M phosphate buffer, pH 7.4 for 3 d and then stored in PBS for at least 60 days.

Tissue preparation. Fixed fetal brains were cut into five equivalent coronal blocks in proportion to the distance between the frontal and parietal poles (6–10 mm). All frontal blocks studied spanned from the genu of the corpus callosum to the optic chiasm.

Ex vivo magnetic resonance imaging. Tissue was embedded alongside a twin control tissue block from the same level in 0.5% agarose and immersed in PBS within a 4 cm diameter plexiglass tube. A custom single-turn solenoidal coil (5 cm diameter, 5 cm length) was utilized for radiofrequency transmission and reception. Experiments were performed using an 11.7 T magnet interfaced with a 9 cm inner diameter magnetic field gradient coil (Bruker, Rheinstetten, Germany). Procedures generally followed the previously published strategy that used diffusion tenser imaging (DTI) to characterize postmortem tissue from other species.(Kroenke et al., 2005a; Kroenke et al., 2009) A Stejskal-Tanner multi- slice spin-echo pulse sequence (δ = 12 ms, Δ = 21 ms, and G = 11.6 G/cm; resulting in b = 2.5 $\mu s/mm^2$) was used for DTI

measurements. The *b*-value for this study was selected to provide an approximate match in diffusion sensitization to a typical *in vivo* measurement in which b = 1 μs/mm^2 (the water apparent diffusion coefficient is ~2.5-fold smaller in post-mortem tissue than *in vivo*).(Sun et al., 2005) Diffusion anisotropy measurements were made using a 25-direction, icosahedral sampling scheme (Batchelor, 2003) in combination with two measurements in which $b = 0$. Other pulse sequence settings were TR = 10 s, TE = 42 ms and NEX (the number of averaged transients) = 1. The image resolution was isotropic, with voxel dimensions of 0.3 mm and a 128 voxel (phase-encode) by 256 voxel (readout) by 70 voxel (slice-select) field of view. Standard procedures(Batchelor, 2003) were followed to determine eigenvalues ($\lambda1$, $\lambda2$, and $\lambda3$, listed from smallest to largest) and the signal amplitude in the absence of diffusion weighting for each voxel from the set of 27 3D images. The apparent diffusion coefficient (ADC = ($\lambda1 + \lambda2 + \lambda3$)/3) and fractional anisotropy (FA, defined in (Basser and Pierpaoli, 1996)) were calculated from the eigenvalues for each voxel. T_2-weighted (T_2w) images were acquired in the same session with pulse sequence settings of TR = 10 s, TE = 80 ms and NEX = 3, and image resolution was isotropic with voxel dimensions as above.

MRI segmentation. ADC maps and diffusion weighted images, herein defined as an image in which the intensity is S(0)*exp(-ADC), were used to classify all tissue and agarose voxels using Matlab 2008b software (Mathworks, Natick, MA). T_2w images were corrected for any small field bias present along the z-axis using the intensity of the uniform agarose embedding medium, which has a T_2 value near fetal brain tissue. Briefly, a profile of the mean intensity of image voxels within agarose along the direction parallel to the rf coil axis of symmetry (the z-axis) was generated. A 1-dimensional bias field correction was implemented by multiplying voxel intensities by a factor derived from the profile that adjusts the mean agarose intensity to unity for

all values of z. Note that this procedure normalizes between-scan T_2 image intensity differences.

Voxels for each tissue block were manually classified by an individual who was blinded to neuropathologic classification as either GM or WM using the derived T_2w image, ADC map, and standard functionalities of the ITK-snap program (http://www.itksnap.org).(Yushkevich et al., 2006) WM within each tissue block was examined for groups of voxels that exhibited abnormal T_2w intensity values defined as follows. At 1 and 2 weeks, focal hyper-intensities (F-hyper) and diffuse hypo-intensities (D-hypo) were identified and classified as compared to normal-appearing WM. At 2 weeks, we observed a decrease of T_2w-image intensity within the WM in control animals that corresponds to normal WM development. We also classified voxels that displayed a diffuse hyper-intensity relative to this pattern as D-hyper voxels. Due to the relatively indistinct borders of this lesion type, only the core of these lesions with clearly elevated intensity vs. surrounding tissue was used for analysis. Additionally, we observed and classified small focal hypo-intense lesions in the PVWM at 2 weeks (F-hypo). Mean values for MRI-derived parameters within WM reported herein for a given case were computed as means over the set of voxels classified as WM. Mean values for lesions within a given case were computed as means of all voxels of a given classification. Mean values for control cases were computed as means of all voxels classified as WM. Thus, MRI lesion characteristics were compared to all WM voxels within control animals, a stringent criterion.

Immunohistochemical studies. After MRI, frontal tissue blocks were cryoprotected by sequential equilibration in 15% and 30% sucrose solutions over 3d. Tissue was rapidly frozen using a liquid nitrogen interface for optimal preservation of O4 and O1 staining. Tissue blocks were serially sectioned at 50 μm using a CM 1950 cryostat (Leica Microsystems Inc., Bannockburn, IL). The detailed immunohistochemical protocols to visualize specific cell types were performed as

previously described.(Back et al., 2001; Riddle et al., 2006; Segovia et al., 2008) OL lineage cells were visualized with the O4 and O1 monoclonal antibodies. Fluorescent double-labeling to distinguish preOLs ($O4^+O1^-$) and immature OLs ($O4^+O1^+$) employed a biotinylated O4 antibody (1:500) and the O1 antibody (1:2000). OL progenitors were distinguished using an antibody against platelet-derived growth factor receptor-α (PDGFRα; 1:1000; courtesy of Dr. William Stallcup, Burnham Institute, La Jolla, CA). Astroglia were visualized with rabbit glial fibrillary acidic protein (GFAP) antisera (1:500, Z-0334; DAKO, Carpinteria, CA). Microglia and macrophages were visualized with a rabbit anti-ionized calcium-binding adapter molecule 1 (Iba1) antibody (1:500; 019-19741; Wako Chemicals, Richmond, VA). Rabbit anti-activated caspase-3-antibody (AC3; 9661B; 1:500; Cell Signaling, Danvers, MA) was used to identify apoptotic cells. Mouse monoclonal antibody Ki67 (1:400; NCL-L-Ki67-MM1; Novocastro, Newcastle upon Tyne, United Kingdom) was visualized after antigen retrieval (10 min in 50mM sodium citrate, pH 6.0 at 90°C). Axons were visualized with the pan-axonal neurofilament marker, mouse monoclonal antibody SMI-312 (1:1000; SMI-312R; Covance, Berkley, CA). Appropriate anti-mouse and anti-rabbit AlexaFluor secondary antibodies were used for visualization of primary antibodies (1:500; Invitrogen, Carlsbad, CA). Neurons were identified using a mouse anti-NeuN antibody (1:500; MAB377; Millipore, Billerica, MA) and visualized using the peroxidase-immunoperoxidase reaction (Vectastain ABC Kit; PK4000; Vector Laboratories, Burlingame, CA) and 3,3'-diaminobenzidine with nickel-enhancement (SK4100; Vector Laboratories). For fluorescent immunohistochemical studies, tissue sections were counterstained with Hoechst 33342 (Invitrogen).

Quantification of the density of GFAP, O4- and O1-labeled cells. The total density of O4- and O1-labeled cells in the corona radiata was determined by a blinded individual in a minimum of

three serial adjacent sections for each case as previously described.(Riddle et al., 2006) Sections were immunostained for O4, O1 and GFAP and imaged using a DMRA fluorescent microscope (Leica Microsystems Inc.). Cell profiles that contained a nucleus, visualized with Hoechst 33324, were counted with a 40x (0.03125 mm^2/field) objective equipped with a counting grid. The profiles of both intact-appearing and degenerating O4-labeled cells were counted and together. Only intact-appearing cells comprised the calculation of total density of O4-labeled profiles. Double-labeled, $O4^+O1^+$ profiles that were not degenerating comprised the immature OL population. Degenerating O4-positive cells were confirmed to contain degenerating nuclei. A minimum of 40 fields were counted for each case. Sixty fields were counted for each control region.

Quantification of GFAP stained area fraction. GFAP staining in each O4/O1-counted field was photographed using a 40x objective with fixed image acquisition settings. GFAP-labeled area was determined by a blinded individual in an unbiased fashion as previously described.(Back et al., 2006a) Briefly, a pixel-intensity histogram was generated for this region using ImageJ (NIH; rsbweb.nih.gov/ij/index.html)(Abramoff et al., 2004) and exported to a spreadsheet. The peak of the histogram was calculated using the three highest frequency bins, and the histogram curve integrated towards the background pixel side of the peak and a value obtained for the area of this region. This area was then doubled to estimate the total distribution of background voxels in the image. The total background area was subtracted from the total region area to define the GFAP-labeled area.

Quantification of activated caspase-3. The density of AC3 in WM lesions followed the protocol outlined above for O4/O1 double-labeling studies. Cells were counted in a minimum of three serial adjacent sections for each case. Sections were stained for AC3 and O4. Cells were counted

with a 40x objective equipped with a counting grid. AC3-labeled cell nuclei that had an O4-labeled profile were defined as degenerating OLs. A minimum of 60 fields were counted for each ischemia case and matched control.

Registration of histopathological and MRI data. From each tissue block, 50 μm serial sections at 600 μm intervals (~12 sections per block) were triple-labeled with anti-Iba1, anti-GFAP, and anti-NeuN. Using a motorized xy stage mounted on an inverted fluorescent microscope, montages of the entire GFAP, IBA-1, NeuN stained sections were captured at 5x magnification (DMIRE2 inverted fluorescent microscope, Leica Microsystems Inc.) using an Orca ER cooled CCD camera (Hammamatsu Photonics, Hammamatsu, Japan) and Stereo Investigator (MicroBrightField Inc., Williston, VT). NeuN montages from each block (scaled to match MRI resolution, see above) were aligned to create a 3D volume using the TurboReg plugin(Thevenaz et al., 1998) (ImageJ). The MRI from each block was aligned with the 3D NeuN stack using FSL (Analysis Group, FMRIB, Oxford, UK).(Jenkinson and Smith, 2001; Smith et al., 2004; Woolrich et al., 2009) Precise 2D alignment between NeuN slices and the corresponding 3D-aligned MRI slices was obtained using a custom program written based on the Insight Segmentation and Registration Toolkit (NIH; www.itk.org) that included sequential position/rotation/scaling and b-spline warping algorithms. (Yoo et al., 2002) All alignment and registration steps were performed using NeuN images as reference, which had good gray/white matter contrast but did not show lesions, and ADC maps as input. Two-dimensional image registration was performed with output voxel dimensions of 0.075mm x 0.075mm. All other MRI parameters and image segmentations were adjusted using the transformation created by this comparison.

Quantification of GFAP and IBA-1 ROI. MRI-derived segmentations were rescaled to match the native histo-pathological resolution and overlaid onto individual GFAP and IBA-1 histo-pathological montages (ImageJ). GFAP and IBA-1 expression in the MRI-defined ROIs was quantified at 5x using the unbiased foreground extraction method previously described for GFAP, above.

Definition of the sensitivity and specificity of high-field MRI. All GFAP montages were analyzed by a blinded individual and image segmentations of gliotic WM areas containing hypertrophic glial processes and increased GFAP density were created. MRI-derived segmentations were rescaled to match the native histopathological resolution and overlaid onto individual GFAP montages (ImageJ). Areas of astrogliosis were defined as the gold standard for brain injury and were aligned and analyzed in 3D. All ROI that were connected in the z plane were classified as a lesion. Overlap between GFAP- and MRI-defined segmentations was analyzed across all registered sections in the injured cohort. Sections without a GFAP ROI were defined as negative. GFAP lesions that did not overlap with MRI ROI were considered false-negative. MRI ROI that were unconnected to GFAP ROI were defined as false-positive. Lesions were divided into two groups, those with GFAP-defined lesions greater and less than 2.5 mm^3 for sensitivity analyses. Sensitivity was defined as the proportion of GFAP lesions that were correctly identified by MRI. Specificity was defined as the proportion of negatives that were correctly identified by MRI.

Statistical analysis. Data analysis was performed using Prism 4 statistical software (GraphPad Software Inc., La Jolla, CA) except where noted. Data were expressed as means ± 1 SEM unless otherwise noted. Comparisons between brain weight data, cell counts and lesion detection were performed using unpaired two-tailed t-tests. Blood gas, regional MRI, lesion-class MRI and MRI lesion-defined histo-pathological descriptive indices were analyzed using ANOVA with *post hoc*

inference testing done with Tukey's multiple comparison test. Analysis of the association between GFAP and OL markers was performed using Pearson correlations on triplicate data from each animal. $P<0.05$ was considered statistically significant.

RESULTS

Ischemia at 0.65 gestation generates three types of chronic progressive WMI.

We analyzed 0.65 gestation fetal sheep that had equivalent physiological responses to global ischemia (Supp. Table 1) at 1 (n=7) or 2 (n=6) weeks recovery. At 1 week recovery, there was no difference in brain weight between the two groups (ischemia; 19.4 ± 2.3 g vs. control; 20.4 ± 2.1 g; mean ± SD). However, at 2 weeks recovery the ischemic group showed a significant reduction in brain weight (ischemia; 25.3 ± 2.8 g vs. control; 31.1 ± 1.8 g; $p < 0.01$) that was accompanied by cerebral white matter atrophy with enlarged lateral ventricles (Supp. Fig. 1). No animals showed signs of intracerebral or intraventricular hemorrhage.

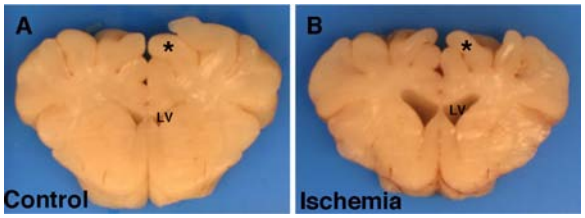

Supplemental Figure 1: Gross pathology apparent in chronic WM injury. A, A 2-week control coronal block at the level of the corpus callosum and caudate. B, The corresponding block of a 2-week ischemia survivor with apparent WM atrophy and an enlarged lateral ventricle (LV).

Three types of cerebral WMI were identified. In 1 and 2 week survivors, the most frequent were diffuse lesions with pronounced astrogliosis (Fig. 1A vs. B). Consistent with prior studies, GFAP-labeled astrocytes had a hypertrophic reactive morphology (Supp. Fig 2A vs. B) and a trend for increasing density at 1 week that was significant at 2 weeks (Supp. Fig 2C).(Roessmann and Gambetti, 1986; Biran et al., 2006) Iba1-labeled microglia and macrophages displayed reactive features (e.g., amoeboid morphology), but were not markedly increased in density (Fig. 1A vs. 1B and insets), and neurofilament protein-labeled axons appeared normal (Fig. 1F). Less frequently observed were apparent focal necrotic lesions where the core contained numerous microglia/macrophages (Fig. 1C) while the periphery typically had more prominent GFAP-labeling. A minority of these lesions had dystrophic-appearing axons (Fig. 1G, arrows) and

axonal spheroids (Fig. 1G, inset). Two week survivors rarely exhibited microcystic lesions (< 1mm across) that were rich in microglia, but contained no astrocytes or axons (Fig.1D, H).

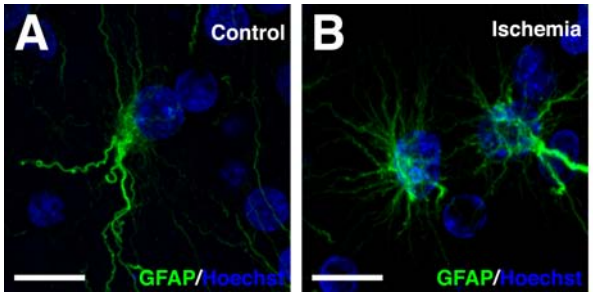

Supplemental Figure 2: Diffuse white matter lesions contained reactive astrocytes. A, Normal appearing GFAP-labeled astrocyte in the deep white matter of a control animal. B, GFAP-labeled astrocytes in an area of diffuse white matter injury with reactive hypertrophic morphologies. C, In areas of diffuse white matter injury, a trend for elevation in astrocyte density was present at 1 week and was significant at 2 weeks. Scale bars: 10 μm, * $p<0.05$

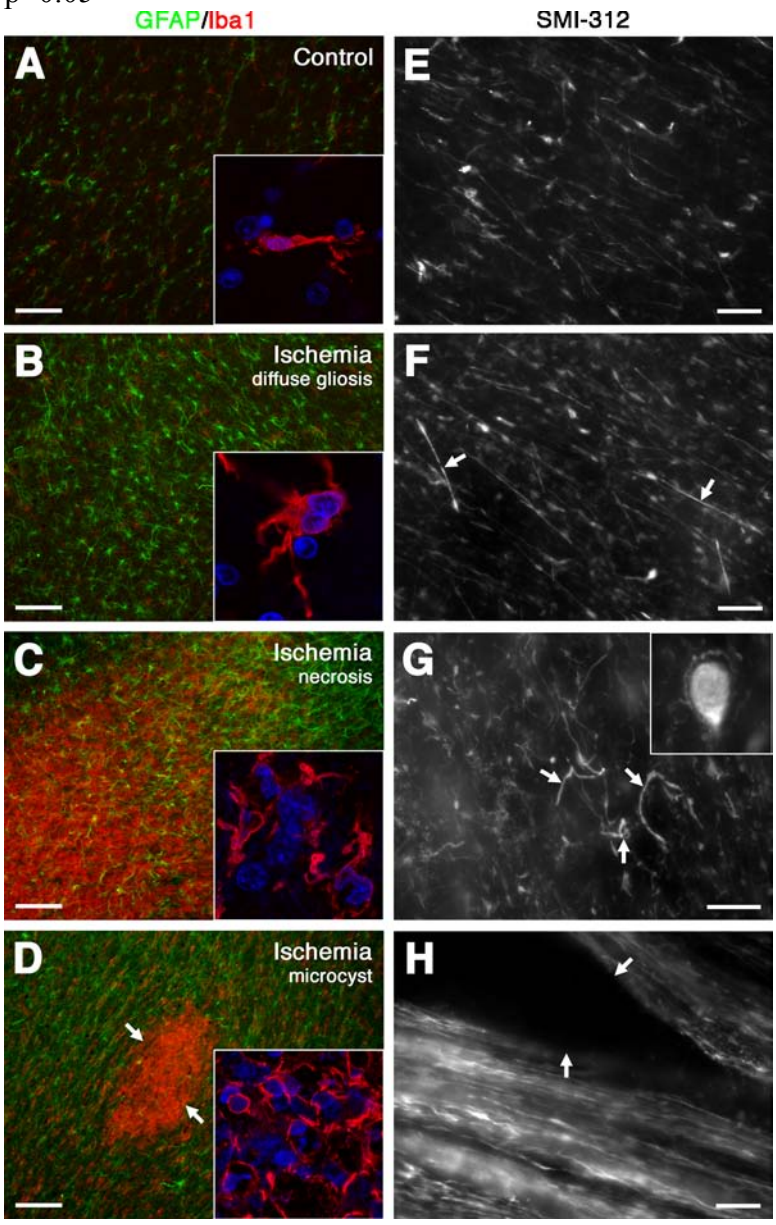

Figure 1: Three major lesion types in chronic WM lesions. A, Control white matter contained resting astrocytes (GFAP) and microglia/macrophages (Iba1) with a resting morphology (inset, Iba1; red, nuclei; blue). B, Diffuse WM lesions had pronounced astrogliosis and a lesser population of microglia/macrophages with a reactive morphology (inset). C, Necrotic foci were observed less frequently that contained numerous reactive microglia/macrophages with amoeboid morphology (inset) and reduced astrocyte staining. D, At 2 weeks, microcysts were infrequently observed that were distinguished by their small size (< 1mm), well-defined borders, intense microglia/macrophage activation and diminished astrocyte staining. E, F Neurofilament staining (SMI 312) reveals normal appearing axons in control white matter (E) and in diffuse gliotic lesions (F, arrows). G, Necrotic foci contained disrupted axons (arrows) and axonal spheroids (inset). H, A microcyst (arrows) surrounded by normal-appearing

axons. Insets: A-D (40 μm x 40 μm); Iba1:red, Hoechst: blue. Scale bars: A-D; 100 μm, E-H; 20 μm.

PreOLs accumulate in diffuse gliotic lesions

In diffuse gliotic lesions, we next analyzed the response of the two major successive OL lineage stages (i.e., preOLs and immature (pre-myelinating) OLs) that predominate in preterm human cerebral WM.(Back et al., 2001) Despite the initial reduction in the total density of these two OL lineages stages by 1 d after ischemia (Fig 2A, upper panel), density recovered to control levels at 1 week, and was significantly increased by 2 weeks. This acute injury response data is from a prior study and illustrates the trajectory of OL maturation.(Riddle et al., 2006) Unexpectedly, a marked increase in density of preOLs at 2 weeks accounted for this pronounced expansion in total OL lineage cells (Fig. 2A middle panel). However, ischemia resulted in a significant reduction in immature OL density at 1 and 2 weeks relative to control (Fig. 2A, lower panel). Indeed, immature OLs failed to increase by 2 weeks after ischemia, despite a 50% increase in controls. Figure 2B, D illustrates a diffuse lesion enriched in reactive astrocytes (GFAP, red) that rarely contained immature OLs or early myelin (O1, green) in contrast to adjacent less gliotic WM. Rather, these gliotic lesions were rich in preOLs (Fig. 2C, E; O4, red). Hence, regions of diffuse astrogliosis coincided with apparent hypo-myelinated lesions that showed an arrest in OL lineage progression at the preOL stage.

In order to determine the associations between preOL and immature OL densities and the degree of gliosis, we quantified GFAP-labeled astrocytes at 1 and 2 weeks in both control and ischemia groups. At 1 week, immature OL density was significantly negatively associated with the GFAP area fraction (Fig. 2F), consistent with onset of arrested OL lineage maturation by 1 week (Fig. 2F upper panel, $r^2=0.32$, $p<0.001$). By 2 weeks, preOL accumulation was significantly positively associated with GFAP area fraction (Fig. 2F lower panel, $r^2=0.68$,

p<0.00001). Thus, progressive preOL accumulation and maturation arrest occur in areas of increasing gliosis, consistent with the notion that astrogliosis is a surrogate marker of preOL maturation arrest in diffuse lesions.

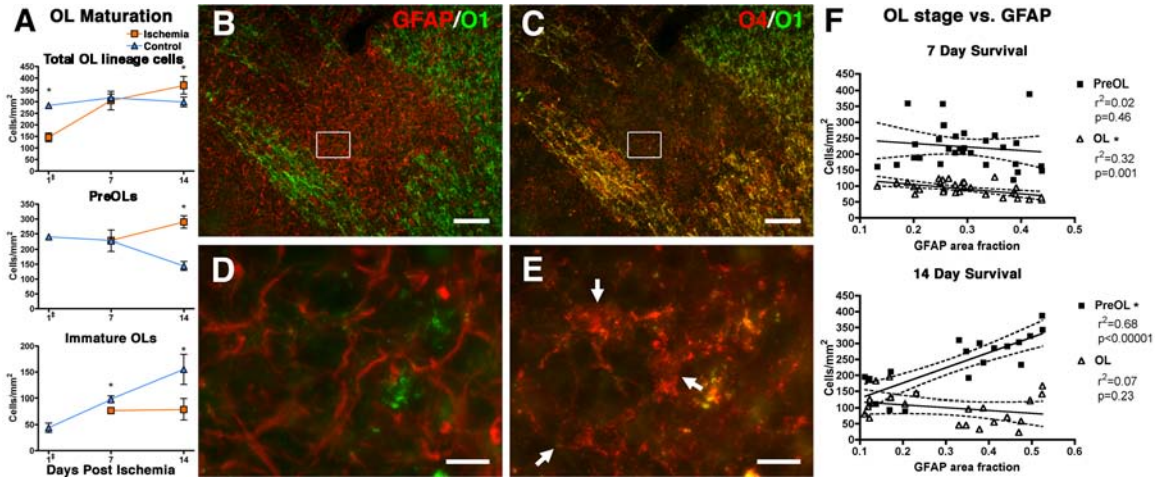

Figure 2: OL lineage maturation arrest in diffuse gliotic lesions. A, After initial depletion (1 d), total OL lineage cells (O4-labeled preOLs and immature OLs) recovered to control levels by 7 d and were significantly increased by 14 d. PreOLs ($O4^+O1^-$) expanded significantly vs. control by 14 d, while immature OLs ($O4^+O1^+$) remained significantly reduced at both 7 and 14 d. Data are presented as mean ± SEM. B, D, A gliotic lesion with increased GFAP had rare immature OLs or early myelin (O1, green). C, E, The same lesion was rich in preOLs (O4, red). F, Linear regression analysis of the association between the degree of astrogliosis and preOL maturation at 7 and 14 d. Importantly, at 14 d, increased preOL density was highly significantly associated with increased gliosis, indicating that gliosis is a strong positive predictor of preOL maturation arrest in chronic diffuse gliotic lesions. The solid line denotes the regression lines and the dashed lines indicate 95% confidence intervals. Scale bars: B, C; 100 μm, D, E; 25 μm. ‡ Previously reported;[12] * p<0.05.

Diffuse WMI is accompanied by early OL progenitor proliferation and delayed preOL death.

Expansion of the preOL population also coincided with a progressive increase in the density of preOLs that displayed morphological features of degeneration (Fig. 3A). By 2 weeks, preOL degeneration was more than two-fold higher than at 1 week (Fig. 3B). Rarely, degenerating cells were labeled with AC3 (Fig. 3C). However, increased preOL degeneration was not accompanied by increased staining for AC3 in either the 1 or 2 week lesions (Fig 3D). The magnitude of preOL degeneration was strongly associated with the extent of astrogliosis as defined by the

GFAP area fraction (r^2=0.39, $p<0.001$). We next determined whether the accumulation of preOLs in diffuse gliotic lesions was related to increased proliferation of preOLs or the OL progenitors that generate preOLs. PDGFRα-positive OL progenitors were infrequently labeled with Ki67 in controls (Fig. 3E), but were increased in lesions (Fig. 3F). By contrast, preOLs rarely co-localized with Ki67 (not shown). Chronic cerebral lesions were, thus, characterized by astrogliosis that coincided with preOL maturation arrest, OL progenitor expansion and persistent preOL degeneration.

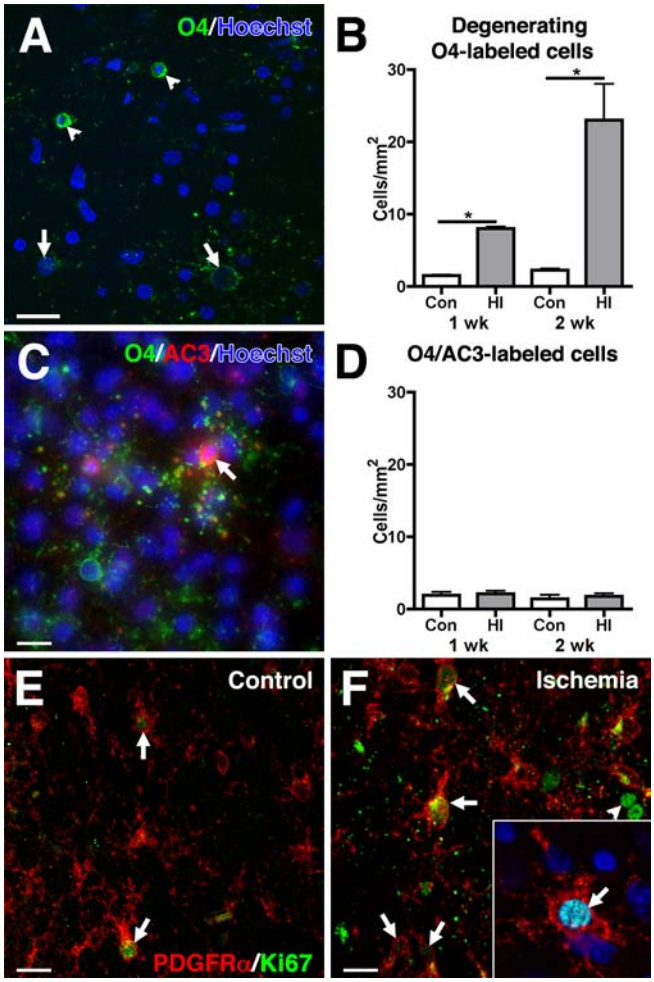

Figure 3: Chronic WM injury is accompanied by delayed preOL death and OL progenitor proliferation. A, Degenerating preOLs were observed 1 and 2 weeks after ischemia by morphological criteria including increased cytoplasmic labeling, process degeneration and nuclear condensation (arrowheads) as compared to healthy preOLs (arrows). This degeneration was significant at 1 and 2 weeks (B). C, Apoptotic (activated caspase-3 positive) preOLs were observed in the WM (arrow), however they were a minority of degenerating cells (D). E, Early OL progenitors (PDGFRα$^+$) in control WM were occasionally positive for Ki67 (arrows). F, Ki67 staining was increased in early OL progenitors 2 weeks after ischemia (arrows) and occasional non-OL lineage cells were also positive for Ki67 (arrowheads). Triple-labeling studies with PDGFRα (red), Ki67 (green), O4 (orange) confirmed that the Ki67-positive cells were O4-negative early OL progenitors. Counterstained with hoechst (blue). Inset; (40 μm x 40 μm). Scale bars: 20 μm * $p<0.05$

Chronic WMI results in progressive cerebral growth retardation

We employed ex vivo MRI to determine if the progressive failure in OL maturation in chronic lesions was accompanied by volumetric changes in total cerebral WM. Based upon the T_2w-

images (with confirmation from ADC and FA images), maps were generated that classified WM image voxels (Fig. 4A). At 1 week, there were no differences in WM volume between control and lesion groups (Fig. 4B). However, at 2 weeks, WM volume was significantly lower in the ischemic group, at levels similar to 1-week controls. By contrast, WM volume in the control animals increased by 30% between 1 and 2 weeks (Fig. 4B). Thus, chronic injury inhibited the normal maturational increase in WM volume.

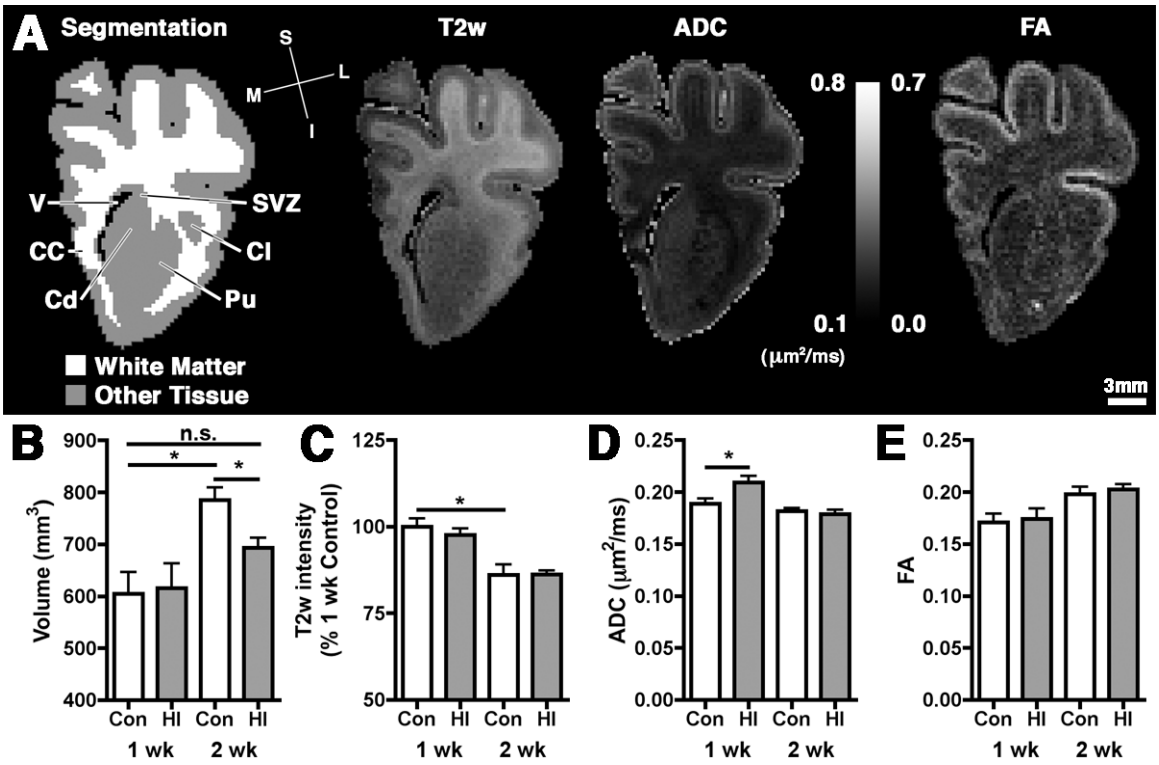

Figure 4: High-field MRI analysis of chronic WM injury. A, Coronal hemisections at the level of the corpus callosum and caudate at 1 week are shown. A WM segmentation was generated based on the T_2w image and used to analyze WM volume, ADC and FA maps. B, WM volume was unchanged at 1 week. At 2 weeks, control WM expanded ~ 30%, but this growth was significantly retarded in the ischemia group. C, Analysis of T_2w image intensities revealed a reduction in WM intensity between 1 and 2 weeks but no significant differences due to ischemia. D, ADC was significantly increased in the 1 week ischemia group, but no other differences were found. E, WM FA values tended to increase between the 1 and 2 week groups but did not reach significance (p=0.07) and no overall differences were found due to ischemia. Abbreviations: CC; corpus callosum, Cd; caudate, Cl; claustrum, Pu; putamen, SVZ; subventricular zone, V; ventricle. * $p<0.05$

High field strength MRI signal abnormalities associated with WMI

We analyzed MRI data for changes in T_2w image intensity, ADC and FA within WM. Between 1 and 2 weeks, T_2w intensity decreased in controls (Fig. 4C), consistent with a process of normal WM maturation. ADC was significantly elevated at 1 week but returned to control levels by 2 weeks (Fig. 4D), consistent with transient edema. There was a non-significant trend toward increasing FA from 1 to 2 weeks (Fig. 4E), but no changes in FA due to ischemia. Consistent with observations in preterm human, FA was elevated in more rapidly maturing WM tracts, such as the posterior limb of the internal capsule (Supp. Fig. 3).(Huang et al., 2009)

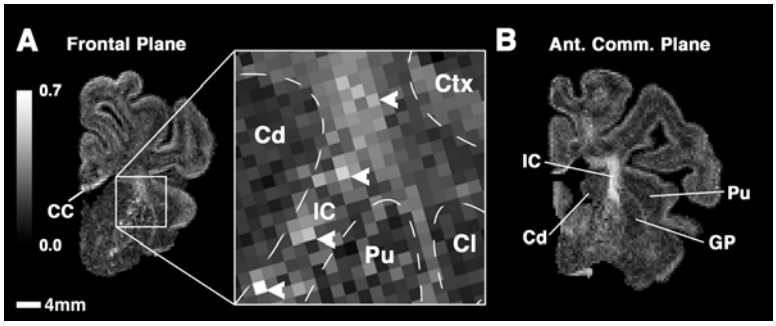

Supplemental Figure 3: FA was increased in the internal capsule in the preterm sheep by 2 weeks. A, At the frontal level observed in this study most WM is immature, however increased FA was observed in fiber bundles from the internal capsule penetrating the striatum (arrowheads) and the corpus callosum. B, At the level of the anterior commissure, the internal capule had markedly increased FA. Abbreviations: CC; corpus callosum, Cd; caudate, Cl; claustrum, Ctx; cortex, GP; globus pallidus, IC; internal capsule, Pu; putamen.

Several types of high field strength MRI signal abnormalities were identified across a spectrum of WMI that ranged from moderate (Fig. 5B, E) to more severe (Fig. 5C, F). At 1 week, T_2w image intensity identified diffuse hypo-intense (D-hypo) abnormalities (Fig. 5B, C) in the deep and sub-gyral WM as well as less frequent focal hyper-intense (F-hyper) lesions that usually localized to superficial gyral WM (Fig. 5C). At 2 weeks, T_2w hypo-intensities (Fig. 5F; D-hypo) were still observed but were less pronounced. However, diffuse WM hyper-intensities (D-hyper) were detected in the deep WM at 2 weeks (Fig. 5E, F). Small focal T_2w hypo-intensities (F-hypo) were detected in the deep WM of some animals (Fig. 5E; F-hypo). F-hyper lesions were still detected in locations similar to week 1 (Fig. 5F; F-hyper). At 1 week, D-hypo and D-hyper lesions were significantly different from control by T_2w (Fig. 5G). At 2 weeks, only

D-hyper lesions did not differ significantly from control (Fig. 5J). Diffusion characteristics were not altered within most of the defined lesion types. ADC was elevated in F-hyper lesions at both 1 and 2 weeks (Fig 5H, K), and FA was significantly reduced in these lesions at 2 weeks (Fig. 5L). However, diffusion imaging was insensitive to the diffuse lesions in the deep WM (D-hypo and D-hyper, Supp. Fig. 4).

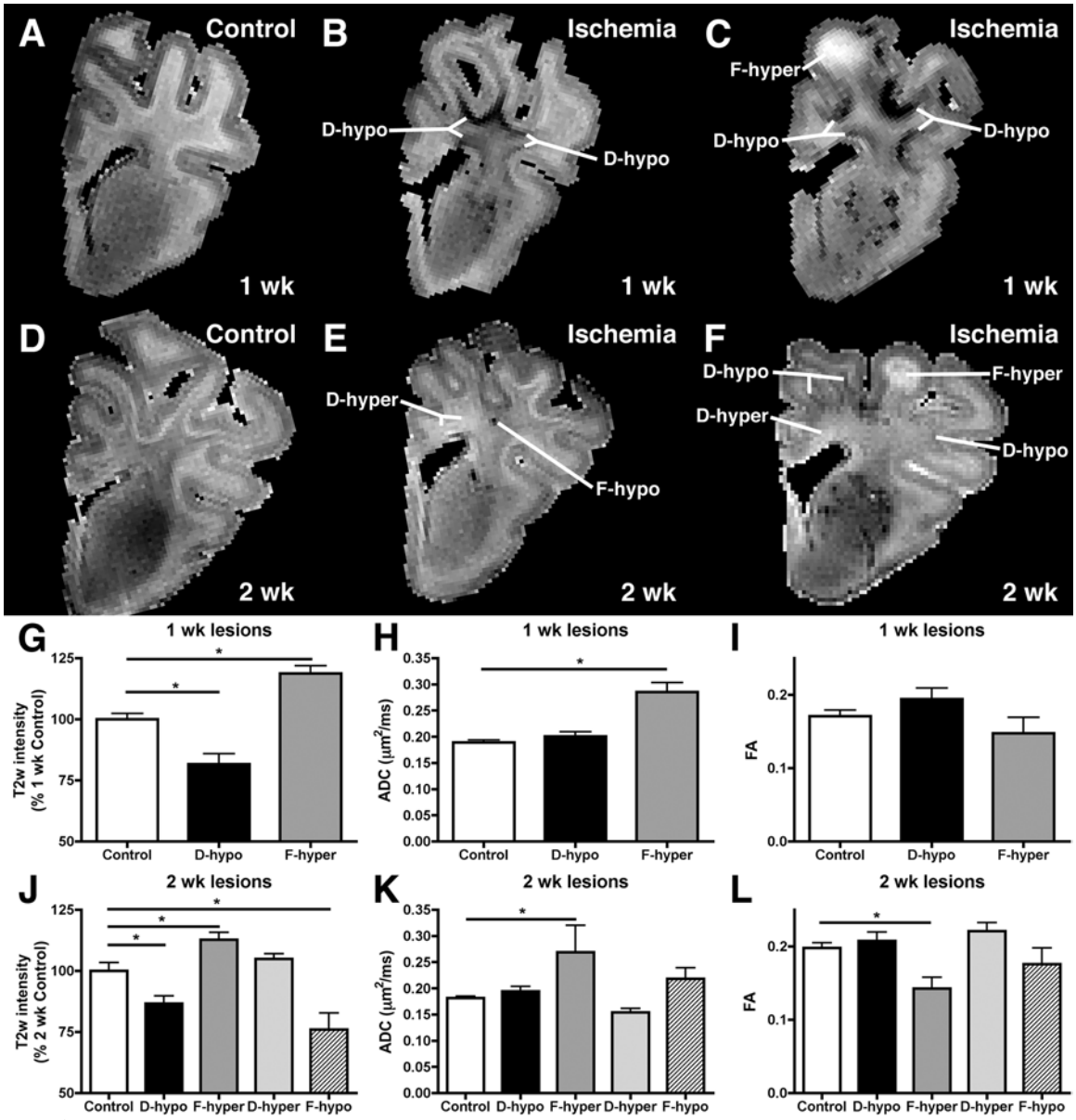

Figure 5: High-field strength MRI signal abnormalities were associated with chronic WM lesions. A, A representative 1 week control T_2w image. B, A T_2w image of an ischemic animal shows prominent diffuse WM hypo-intensities (D-hypo). C, T_2w image shows the most severely observed focal gyral WM hyper-intensity (F-hyper) as well as D-hypo lesions. D, A

representative 2-week control T_2w image with notable decrease in WM T_2w image intensity vs. 1-week control. E, Two weeks after ischemia, new types of WM signal abnormalities are apparent. These include small focal WM hypo-intensities (F-hypo) and diffuse apparent hyper-intensities (D-hyper) in the PVWM. F, The new lesion types are observed in addition to D-hypo and F-hyper lesions, although they are less prominent than at 1 week. G, One week D-hypo and F-hyper lesion T_2w image intensities differ significantly from control. H, ADC is significantly increased only in F-hyper lesions at 1 week. I, FA in the lesions did not differ from control by 1 week. J, At 2 weeks, T_2w intensities were significantly different from control for D-hypo, F-hyper and F-hypo lesions. K, ADC was significantly increased only in F-hyper lesions. Interestingly, ADC trended down in D-hyper lesions (p=0.07). L, At 2 weeks, F-hyper lesions displayed significantly reduced FA values. * $p<0.05$

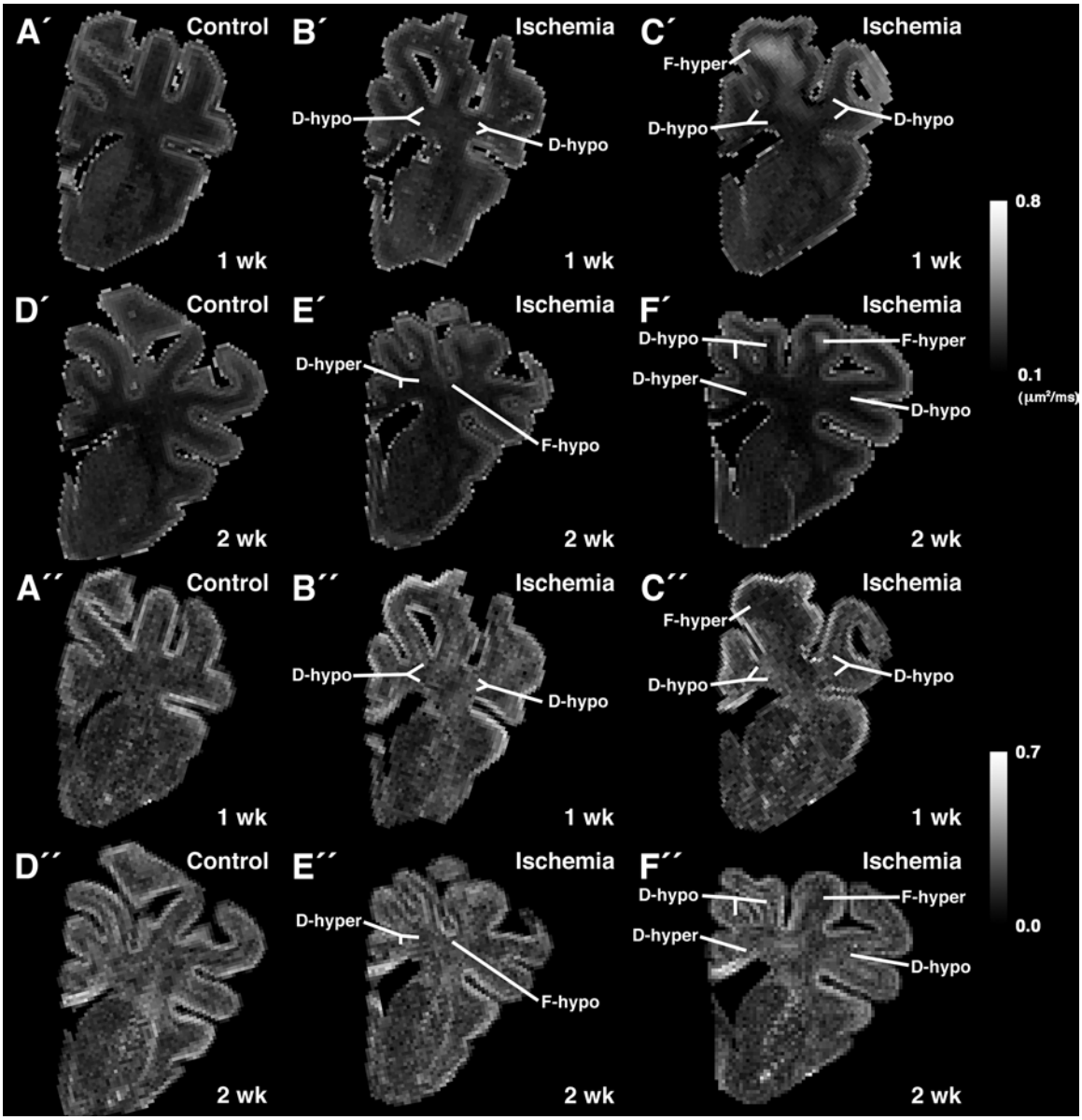

Supplemental Figure 4: Altered diffusion characteristics associated with moderate to severe WM lesions shown in Figure 5. A´-F´, ADC maps corresponding to Figure 5A-F. ADC appears

increased in F-hyper lesions (C´-F´). A´´-F´´, FA maps corresponding to Figure 5A-F. FA appears decreased in F-hyper lesions (C´´-F´´).

Diffuse deep WM lesions were the largest and most commonly observed (Table 1), comprising 88% of total lesion volume at 1 week and 83% at 2 weeks. In contrast, focal gyral WM lesions (F-hyper) were markedly smaller, less frequently observed and represented only 12% of total lesion volume at 1 week and 16% at 2 weeks. Focal hypo-intensities (F-hypo) in the deep WM were infrequently observed and constituted less than 2% of lesion volume at 2 weeks. Thus, diffuse deep WM lesions represented the most common lesion observed as well as the greatest contributor to total lesion burden at both 1 and 2 weeks.

Table 1: Features of MRI-defined lesions.

MRI Type	Survival	Total lesion number	Mean lesion volume/ animal ± S.D. (mm^3)	% Lesion volume at 1 or 2 weeks	% animals with lesion
D-hypo	1 week	23	68.4 ± 64.4	88.6	100 (7/7)
D-hypo	2 week	12	40.5 ± 12.4	50.6	83 (5/6)
D-hyper	2 week	5	22.4 ± 7.6	32.0	67 (4/6)
F-hyper	1 week	12	13.3± 13.1	11.4	71 (5/7)
F-hyper	2 week	6	6.2 ± 2.8	15.9	67 (4/6)
F-hypo	2 week	8	0.8 ± 1.1	1.5	50 (3/6)

Registration algorithms define histopathological features of high-field MRI abnormalities.

We next sought to determine if the different types of WM lesions identified by histopathology (Fig. 1) correspond to definable MRI abnormalities (Fig. 5). We quantified the astrocyte marker GFAP and the microglial/macrophage marker Iba1 within each MRI-defined lesion analyzed for T_2w signal abnormalities. Figure 6 demonstrates selected aspects of our protocol (Suppl. Fig. 5) for the registration of diffuse hypo-intense (D-hypo) WM lesions defined by MRI with GFAP staining. Histopathological images (Fig. 6A) were aligned with MRI data (Fig. 6B), allowing MRI-defined ROIs (Fig. 6C) to be superimposed on histopathological injury markers (Fig. 6D, E) at high resolution (Fig. 6F).

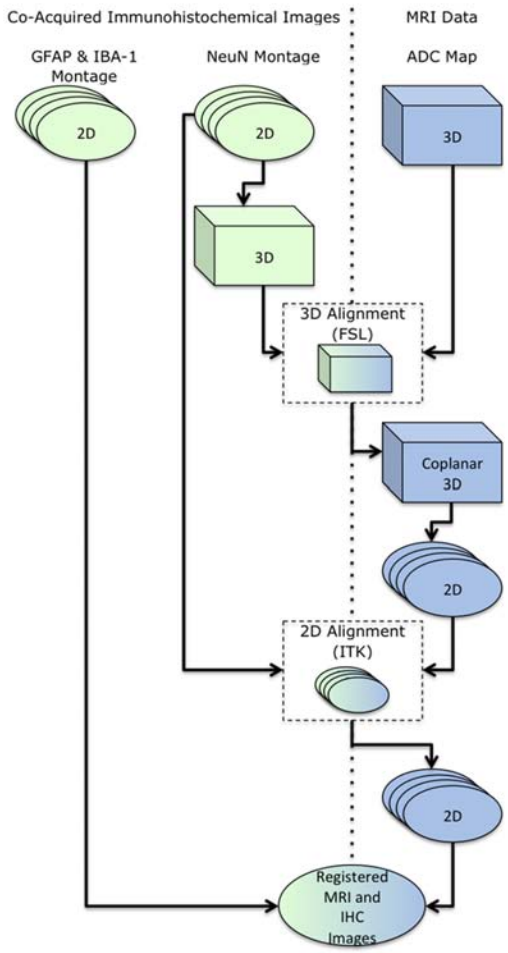

Supplemental Figure 5: Summary workflow of registration algorithm. Serial series of ~ 10 NeuN, GFAP and Iba1 triple-labeled sections were montaged at 5x magnification. NeuN montages with good anatomical contrast independent of WM lesion markers were assembled into a 3D reconstruction of the brain block using ImageJ. Any missing histological sections were replaced with the nearest intact section. Damaged sections were included as they appeared without modification. This 3D histopathological volume was rigidly registered to the ADC map using FSL in order to make the two datasets coplanar. The defined transformation was also applied to all other MRI parameters and the MRI-defined lesion maps. The ADC slices that were coplanar with the histopathological sections were then selected. 2D ADC slice-NeuN montage pairs were then aligned using sequential rotation, scaling and b-spline warping algorithms generated using the ITK toolkit. Once alignment was complete, MRI-defined lesion maps were superimposed on the GFAP and Iba1 montages and quantified.

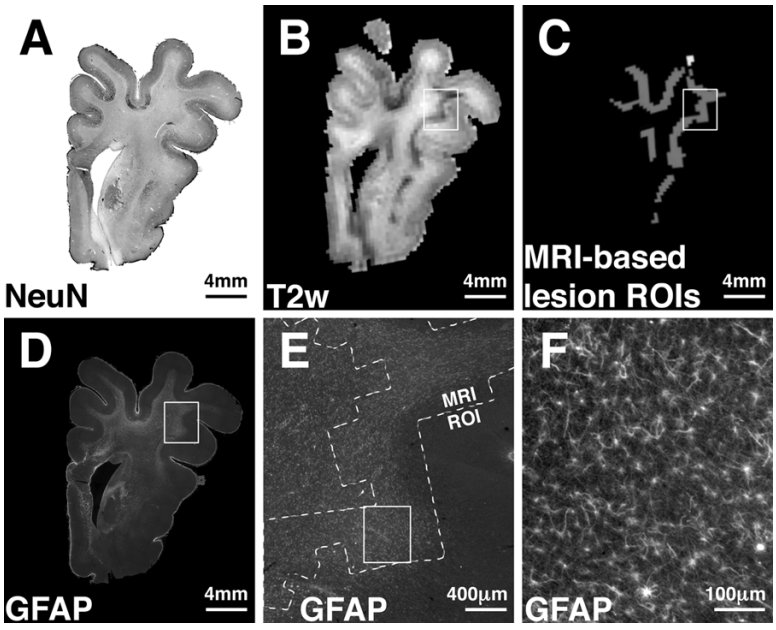

Figure 6: Independent histopathological-MRI registration allows quantification of cellular gliosis. A, The NeuN montage with tissue, but no lesion, contrast from a 1 week ischemia survivor used for registration with MRI. B, T_2w image of the MRI slice registered to A with apparent WM signal abnormalities. C, MRI-based ROI map corresponding to panels A and B. D, The GFAP montage that was co-acquired with A. Inset boxes in B-D correspond to panel E. E, GFAP montage with superimposed MRI-defined ROI (dashed line) indicating the area of GFAP quantification. Inset corresponds to panel F. F, High-resolution histopathological data with cellular detail was acquired and analyzed for GFAP quantification.

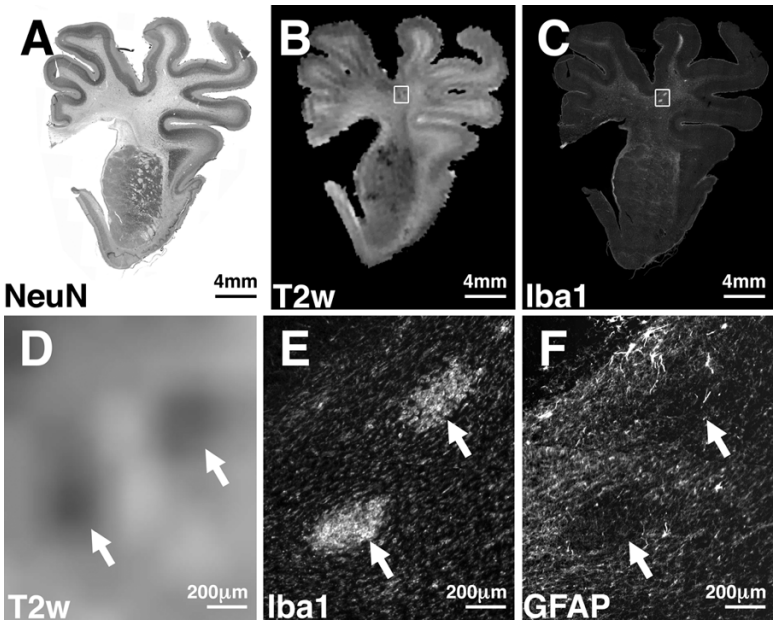

Figure 7: Registration algorithm allows sub-mm alignment of MRI and histopathological features of the WM. A, The NeuN montage with tissue, but no lesion, contrast from a 2 week ischemia survivor used for registration with MRI. B, The T_2w image registered of A with apparent WM signal abnormalities including two small WM signal abnormalities in the box. C, The Iba1 montage that was co-acquired with A. Two small microglial/macrophage foci are apparent in the box. Inset boxes in B and C correspond to panels D-E. D, Registered T_2w image of inset in B. Note the pair of abnormal WM hypo-intensities. E, F, Registered Iba1 and GFAP images respectively. Two lesions ~300 μm in diameter with intense microglial/macrophage infiltration and reduced astroglial staining (arrows) consistent with microcysts are aligned with the signal abnormalities in D.

Microscopic necrosis has not been readily identifiable by neuroimaging of human preterm survivors.(Volpe, 2008) We found that F-hypo lesions, which occurred infrequently (Table 1), corresponded to areas of microscopic necrosis defined by microcysts. Figure 7 shows two focal hypo-intense (F-hypo) lesions (Fig. 7B, D) that correspond to two microcysts intensely labeled with Iba1 (Fig. 7C, E) but with reduced labeling for GFAP (Fig. 7F). This unusual example of two microcysts occurring in close proximity demonstrates the ability of our registration method to resolve these discreet lesions. Hence, it is feasible to register both diffuse WM lesions at the sub mm level in a large brain region (Fig. 6) and discrete focal lesions less than 500 microns across (Fig. 7) that are identifiable by MRI and histopathology.

Figure 8 provides a quantitative analysis of the astroglial and microglial responses in non-necrotic (Fig. 8A, C, E) and apparent necrotic lesions (Fig. 8B, D, F) defined by histopathology and MRI. At 1 week, robust GFAP-defined astrogliosis occurred in both D-hypo lesions and F-

hyper lesions (Fig. 8A, B). In D-hypo lesions (Fig. 8A), astrogliosis was accompanied by a non-significant trend toward elevation of Iba1, consistent with moderate microglial activation in non-necrotic lesions. By contrast, F-hyper lesions (Fig. 8B) showed a significant increase in Iba1, consistent with lesions with early necrosis. At 2 weeks, astrogliosis remained significantly elevated only in D-hypo lesions and Iba1 remained similar to week 1 (Fig. 8C). Similarly, an increase in both GFAP and Iba1 also occurred in D-hyper lesions but neither reached significance (Fig. 8E). In F-hyper lesions, GFAP dramatically decreased from 1 to 2 weeks and Iba1 markedly increased to over 300% of control levels (Fig. 8D), consistent with evolving necrosis. Similarly, F-hypo lesions, which coincide with microcysts (Fig. 7), showed robust elevation of Iba1 at 2 weeks but had minimal astrogliosis (Fig. 8F). Hence, at both 1 and 2 weeks, D-hypo and D-hyper identified non-necrotic astrogliosis with marginal microglial activation, whereas F-hyper and F-hypo identified apparent evolving necrosis. Thus, MRI was able to distinguish three distinct histopathological classes of lesions.

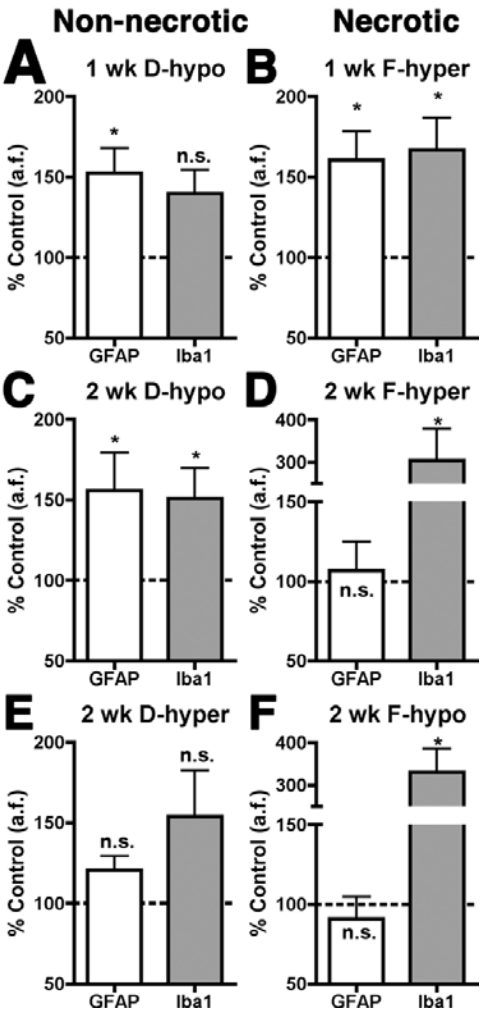

Figure 8: Quantification of GFAP and Iba1 within MRI-defined WM signal abnormalities. A, At 1 week, D-hypo lesions had significantly elevated GFAP, consistent with diffuse gliotic injury. B, At 1 week, F-hyper lesions had significantly elevated GFAP and Iba1. C, At 2 weeks, GFAP remained elevated in D-hypo lesions and Iba1 was also elevated. D, At 2 weeks, GFAP was no longer elevated in F-hyper lesions and Iba1 was markedly increased vs. age and region matched control, consistent with progressive necrotic injury. E, D-hyper lesions tended to have increased GFAP and Iba1, but were not significantly different. F, F-hypo lesions had markedly increased Iba1 labeling and no change in GFAP labeling vs. control, as seen in microcysts. * $p<0.05$

Sensitivity and specificity of high-field MRI

Since gliotic lesions were most commonly observed, we defined the sensitivity and specificity of non-necrotic T_2w signal abnormalities (D-hypo and D-hyper) in astrogliotic lesions. MRI lesions were present in all animals with astrogliosis at 1 and 2 weeks. At 1 week, D-hypo lesions detected 13/19 astrogliotic lesions. However, MRI was much more sensitive to large lesions (> 2.5 mm^3) than small lesions (< 2.5 mm^3) with a sensitivity of 100% (12/12) and 14% (1/7), respectively ($p<0.001$, two-tailed t test), such that that the effective limit of detection for these lesions was 2.5 mm^3. Large lesions comprised the majority of the total lesion volume (377 mm^3 large vs. 6 mm^3 small). GFAP-defined ROIs that constituted 84% of the total lesion volume were detected by MRI. MRI identified three small false-positive lesions and its specificity was 92% (3/39 negative observations). At 2 weeks, D-hypo or D-hyper lesions detected 9/21 astrogliotic lesions. Large lesions were also more readily detected than small lesions with a sensitivity of 75% (6/8) and 23% (3/12), respectively ($p<0.05$). Large lesions still dominated total lesion volume (186 mm^3 large vs. 20 mm^3 small). GFAP-defined ROIs that constituted 66% of the total lesion volume were detected by MRI. Only one small false-positive lesion was identified and specificity was 97% (1/29 negative observations).

DISCUSSION

Progress to develop treatments for perinatal WMI has been hampered by the lack of surrogate markers for serial assessment of perinatal WMI progression. We analyzed a pre-clinical model of chronic cerebral WMI in preterm fetal sheep where novel registration algorithms were applied to define the potential of high-field MRI to distinguish several distinct types of histopathologically-defined injury. This study yielded the following novel findings: (1) A spectrum of chronic WMI was generated similar to that commonly observed in human preterm survivors.(Buser et al.) Thus, WMI with focal or diffuse gliosis predominated and apparent cystic necrotic PVL-like lesions were infrequently observed. (2) Despite the fact that preOL degeneration predominates in early WMI,(Back et al., 2005b; Riddle et al., 2006) diffuse gliotic lesions contained an expanded population of preOLs that failed to differentiate to OLs. There was, thus, a net increase in total preOLs in lesions, that fully compensated for minimal delayed preOL degeneration. (3) PreOL maturation arrest was directly associated with the degree of gliosis, which supported that diffuse astrogliosis is a surrogate marker for lesions with arrested preOL differentiation. (4) Consistent with volumetric MRI studies in human preterm survivors,(Inder et al., 2005a) chronic WMI was accompanied by a significant reduction in white matter growth. (5) Novel registration algorithms demonstrated that high-field MRI distinguished three major types of chronic WMI. (6) High-field MRI was up to 100% sensitive and 92% specific for histopathologically-defined astrogliotic lesions larger than 2.5 mm^3.

The propensity for myelination failure is a central pathological feature that distinguishes chronic WMI from other forms of cerebral palsy. We previously proposed that myelination failure in chronic human WMI is related to targeted deletion of a susceptible pool of preOLs required to generate mature OLs.(Back and Volpe, 1997) Our results support a more complex

mechanism whereby a combination of proliferative, degenerative and arrested maturational processes result in a net expansion in the pool of preOLs with potential to generate OLs. Similar to the rat,(Segovia et al., 2008) expansion of the preOL pool was driven by proliferation of PDGFrα^{+} OL progenitors. However, delayed preOL death in rats was more severe than in fetal sheep. In rats, chronic gray and white matter injury generated preOL death that was ~50% of that observed acutely and involved widespread activation of caspase-3.(Segovia et al., 2008) By contrast, more moderate and relatively selective acute WMI is generated in our fetal sheep preparation.(Riddle et al., 2006) Although preOL death was still increasing two weeks after ischemia, it nevertheless, accounted for only ~15% of acute death and occurred independently of caspase-3 activation. Taken together, our rodent and sheep data support a mechanism where preOL survival outweighs death with a persistent net expansion in the preOL pool.

WMI was characterized by a chronic progressive process that resulted in blunting of WM growth. In fact, the magnitude of preOL arrest and astrogliosis were significantly associated across a wide range of injury responses in 2 week survivors. Further studies are needed to define the mechanism of preOL arrest in astrogliotic lesions. In demyelinating lesions, traumatic spinal cord injury, and ischemic lesions, robust expression of hyaluronan or its receptor CD44 has been detected.(Wang et al., 2002; Back et al., 2005a; Struve et al., 2005) Arrest of preOL maturation is stimulated both *in vitro* and *in vivo* by hyaluronan derived from reactive astrocytes.(Back et al., 2005a; Sloane et al., 2010) Chronic myelination failure may, thus, arise from one or more inhibitory factors that block progression of preOLs to mature myelinating OLs. It is presently unclear, however, whether preOLs in chronic lesions would retain their myelinogenic potential if extrinsic inhibitory signals were removed. Additional factors such as delayed axonal degeneration may also contribute to chronic myelination failure.

Although performed in postmortem fixed tissue, there are a number of studies that indicate that both diffusion and T_2-mediated MRI contrast observed in these studies is likely to be preserved *in vivo*. Physiological effects *in vivo* can influence diffusion parameters, but diffusion characteristics due to tissue microstructure observed *ex vivo* are likely to be observed *in vivo*. Several studies have quantitatively characterized the relationship between *in vivo* and *ex vivo* MRI of fixed postmortem tissue.(Guilfoyle et al., 2003; Sun et al., 2003; Sun et al., 2005; D'Arceuil and de Crespigny, 2007; D'Arceuil et al., 2007) In particular, absolute ADC values decrease by a factor of ~2.7 but ADC contrast between neighboring regions are preserved after death.(Sun et al., 2003; Kroenke et al., 2005b) Similarly, T_2 values decrease after death and fixation, but retain the *in vivo* pattern of image contrast between gray matter and WM,(Tovi and Ericsson, 1992; Blamire et al., 1999; Yong-Hing et al., 2005; Dawe et al., 2009) as well as between multiple sclerosis (MS) lesions and normal WM.(Nagara et al., 1987; Macchi and Cioffi, 1992; Schmierer et al., 2003) T_2 hypointense MRI artifacts have been identified in tissue preserved for years in formalin.(van Duijn et al., 2011) Tissue in our study was preserved in paraformaldehyde and stored long-term in saline and we do not believe the image contrast pattern observed due to this effect resembles the large T_2w abnormalities seen in fetal WM.

Many previous studies that co-analyzed MRI and histopathological data relied on visual level matching, which did not permit quantitation. An alternative approach employed placement of fiduciary markers, which required prior surgical intervention and tissue destruction.(Lazebnik et al., 2003; McGrath et al., 2010) A recent mouse atlas study employed three-dimensional reconstruction of histology for association with MRI data.(Lebenberg et al., 2010) We improved upon this approach to address the unique challenges related to analysis of a gyrencephalic fetal

brain that sustains more distortion during tissue preparation. We achieved sub-mm registration that permitted direct measurement of cellular elements within MRI-defined regions.

Our studies provide new insight into the pathogenesis of chronic WMI associated with preOL maturation arrest. It has been proposed that the dominant lesion in the majority of cases of diffuse WMI contains microscopic areas of necrosis defined as noncystic PVL (PVL with microcysts) that are not readily detected by MRI, and that diffuse gliosis without microcysts is of uncertain pathological significance.(Volpe, 2008) This microscopic necrosis has further been proposed as the dominant lesion that coincides with preOL maturation arrest.(Volpe, 2009) Given the small dimensions of microcysts, they may be underestimated by histopathological surveys. Our most commonly observed MRI lesions were the D-hypo and D-hyper signal abnormalities. These corresponded to lesions with diffuse gliosis without necrosis (Table 2). Consistent with the pronounced decline in cystic PVL in human,(Back, 2006; Volpe, 2009) we also observed few necrotic PVL lesions that were enriched in reactive microglia and identified by focal hyper-intensities on T_2w imaging (Table 1). Small discrete microcysts enriched in macrophages were visualized by T_2w as small focal hypo-intense lesions. Thus, high-field T_2w imaging detected microcysts not well visualized by neuroimaging in preterm survivors.(Volpe, 2008) Microcysts were not detected at 1 week, but by 2 weeks, appeared to evolve to discrete lesions visualized by MRI. Although, as in human,(Pierson et al., 2007) these lesions were commonly observed (50% of animals) they constituted only 1.5% of total lesion volume. Thus, microcysts were infrequent, even in animals with extensive WMI, and diffuse astrogliosis frequently occurred without microcysts. Our findings support that preOL maturation arrest occurs in areas of diffuse WM gliosis with or without microscopic areas of necrosis.

Our ability to detect diffuse gliosis was clearly time- and modality-dependent, with greatest sensitivity at 1 week in T_2w images. These lesions were highly sensitive for large, potentially clinically-relevant, gliotic lesions, and captured the majority of the lesion at 1 week. The sensitivity, however, declined by 2 weeks and MRI underestimated both the number and size of gliotic lesions. We also detected no change in diffusion characteristics at 1-2 weeks. The latter finding may be consistent with prior studies where sensitivity of diffusion characteristics to identify diffuse WMI was observed in preterm infants with WMI that were studied at ~3 weeks or later after birth.(Huppi et al., 2001; Miller et al., 2002) Other predominantly necrotic lesions displayed diffusion abnormalities that were increased at 2 weeks after injury as previously reported for patients with PVL.(Ment et al., 2009) At 1-2 weeks, hypo-intense lesions were identified as novel T_2w lesions with markedly low image intensity that were most prominent at 1 week.

The detection of T_2 hypo-intense lesions may be limited by the timing of imaging after injury and magnetic field strength. While we observed the greatest sensitivity to detect deep WM lesions 1 week after injury in the immature fetal sheep (~28-30 week human equivalence), prior studies have imaged preterm survivors either within weeks after birth or at term equivalence at 1 -3 T.(Ment et al., 2009; Miller and Ferriero, 2009; Mathur et al., 2010; Rutherford et al., 2010) The detection of small lesions, such as microcysts, *in vivo* may also be hampered by the relatively limited imaging resolutions achievable with most clinically-available MRI systems. Further, magnetic field strength-dependent factors that influence transverse relaxation may impart increased sensitivity to high field strength MRI systems, such as the 11.7 T system used herein, relative to current clinically accessible magnetic field strengths of 1.5-3 T. For example, we did not observe well-defined T_2w hypo-intense lesions at 3 T within a subset of the tissue

samples that had hypo-intense lesions used for this study (unpublished observations). Prior studies of MS lesions have demonstrated T_2 hypo-intensities related to T_2* contrast at 7 T.(Pitt et al., 2010) Thus, imaging modalities that maximize sensitivity to magnetic susceptibility, such as T_2*-weighting, may enhance the contrast of the lesions at lower field strengths. The biochemical source and the sensitivity of alternate MRI modalities for these lesions are currently under investigation.

Hence, current clinical MRI field strength may be a limiting factor to detect diffuse gliosis, microscopic necrosis and possibly other types of WMI. These data underscore the need for future studies to determine the clinical-translational utility of high-field MRI for improved diagnosis of perinatal WMI. Our large preclinical animal model provides unique experimental access to questions directed at the mechanisms of myelination failure in advanced lesions as well as definition of the optimal field strength and modality to resolve evolving lesions by MRI. Such studies will be critically important to define the potential windows after injury when myelination failure might be ameliorated. One such potential therapeutic strategy may be to reverse preOL maturation arrest by agents that alter the composition of the glial scar to promote myelination.(Sherman and Back, 2008)

Table 2: Summary of histopathological and MRI characteristics of cerebral WM lesions.

Path. Diagnosis	Survival	MRI Type	Location	Histopathological Features		MRI Characteristics		
				MG/Mø	AS	T_2w	ADC	FA
Diffuse non-cystic	1 week	D-hypo	Deep & Sub-gyral WM	+	+ + +*	↓*	NC	NC
gliosis	2 week	D-hypo	Deep & Sub-gyral WM	+*	+ + +*	↓*	NC	NC
		D-hyper	Deep WM	+	+	↑	NC	NC
Focal necrosis	1 week	F-hyper	Gyral WM	+ +*	+ + +*	↑*	↑*	↓
	2 week	F-hyper	Gyral WM	+ + +*	+	↑*	↑*	↓*
Microcysts	2 week	F-hypo	PVWM	+ + +*	–	↓*	↑	↓

MG, microglia; Mø, macrophage; AS, astrocyte; NC, no change vs. control; ↑, increased relative to control; ↓, decreased relative to control; *, values significantly different from control
MG/Mø (Iba1 % Control): +, 100–175%; + +, 175–250%; + + +, > 250%.
AS (GFAP % control): –, < 100%; +, 100–125%; + +, 125–150%; + + +, > 150%;

CHAPTER 3

DIFFERENTIAL SUSCEPTIBILITY TO AXONOPATHY IN NECROTIC AND NON-NECROTIC PERINATAL WHITE MATTER INJURY

Art Riddle, BS[1], Jennifer Maire, BS[1], Xi Gong, MD[1], Kevin Chen, BS[1], Chris Kroenke, PhD[2,3,4], A. Roger Hohimer, PhD[5], Stephen Back, MD,PhD[1,6]

From the Departments of Pediatrics[1], Behavioral Neuroscience[2], the Advanced Imaging Research Center[3], the Oregon National Primate Research Center[4], Obstetrics and Gynecology[5], and Neurology[6] Oregon Health & Science University, Portland, Oregon.

Riddle A, Maire J, Gong X, Chen KX, Kroenke CD, Hohimer AR, Back SA (2011) Differential susceptibility to axonopathy in necrotic and non-necrotic white matter injury. Stroke; In Press.

ABSTRACT

Although cerebral white matter injury (WMI) is the most common lesion in survivors of premature birth, the role of axonal injury in the myelination failure that leads to cerebral palsy has been hampered by lack of a suitable animal model. Thus, the focus for development of preventive therapies for WMI remains unclear. We analyzed WMI in a novel preterm fetal sheep model of global cerebral ischemia that replicates the relative burden of necrotic and non-necrotic human WMI. WMI was analyzed at 1- or 2-weeks after ischemia and identified by ex vivo high-field (11.7 tesla) MRI of fixed brain tissue. Axonal integrity was analyzed by immunohistochemical detection of axon injury markers and by transmission electron microscopy (EM) to quantify intact and degenerating axons in MRI-defined lesions within superficial and deep periventricular white matter. Axonal degeneration, defined by staining for neurofilament protein and β-amyloid precursor protein, was restricted to small discrete foci of necrosis with robust microglial activation and low astroglial reaction. Axonal degeneration was not visualized within large non-necrotic lesions with diffuse reactive astrogliosis, which was the major form of WMI. In diffuse gliotic lesions, quantitiative EM studies found no significant differences in the density of intact and degenerating axons or in the distribution of axon diameters. Axonal degeneration occurs in association with small discrete foci of necrosis with pan-cellular loss, but was not detectible within primary large non-necrotic lesions. Hence, therapies directed at prevention of axonal degeneration should target mechanisms related to necrotic WMI.

ACKNOWLEDGEMENTS

Supported by the NIH (P51RR000163 (CDK); National Institutes of Neurological Diseases and Stroke: 1RO1NS054044, R37NS045737-06S1/06S2 to SAB and 1F30NS066704 to AR) a Bugher Award from the American Heart Association (SAB) and the March of Dimes Birth Defects Foundation (SAB). High-field MRI instrumentation used in this work was purchased with support from the W.M. Keck Foundation. The Electron Microscopy Core at OHSU is supported by NIH grant P30 NS061800. We would like to thank Sue A. Aicher (PI), Robert Kayton (Core Manager) and Elizabeth Geltz and the OHSU Electron Microscopy Core for their assistance.

INRODUCTION

Cerebral hypoxia-ischemia (H-I) is a common cause of white matter injury (WMI) in the developing brain and a leading cause of life-long neurological disability in survivors of premature birth and infants with congenital heart disease.(McQuillen and Miller, 2010) WMI is now the most common lesion in children with CP,(Bax et al., 2006) and manifests as the non-progressive motor deficits of cerebral palsy (CP) as well as cognitive and learning disabilities. Advances in neuro-imaging have identified a shift from predominantly large necrotic WMI (periventricular leukomalacia; PVL) to focal or diffuse non-destructive lesions.(Ment et al., 2009) However, the burden of small foci of microscopic necrosis, that are undetected by MRI, remains unresolved in human(Pierson et al., 2007) but is low in a preclinical model of WMI in preterm fetal sheep.(Riddle et al., 2011)

The propensity for myelination failure distinguishes WMI from other forms of CP that involve gray matter injury.(Volpe, 2008) In necrotic lesions, myelination failure arises from acute degeneration of axons and glia.(Kinney and Back, 1998) Due to the pronounced reduction in necrotic WMI lesions in contemporary cases of WMI, there has been increased study of myelination failure in non-necrotic lesions where diffuse astrogliosis predominates. One emerging mechanism of myelination failure in non-necrotic lesions involves disrupted maturation of the oligodendrocyte (OL) lineage. Although H-I triggers substantial degeneration of late oligodendrocyte progenitors (preOLs) during acute WMI, preOLs mount a robust regenerative response, but fail to differentiate in chronic lesions.(Segovia et al., 2008; Riddle et al., 2011) Presently unclear, however, is the extent to which axonopathy contributes to myelination failure in these non-necrotic lesions and lesions with microscopic necrosis.

We addressed here the role of axonopathy in myelination failure, because it has significant implications for therapeutic strategies to promote myelination in chronic WMI. We employed a fetal sheep model of global cerebral ischemia where we recently defined the relative burden of microscopic necrosis and non-necrotic chronic WMI through a combination of histopathology and high-field MRI.(Riddle et al., 2011) We identified that both forms of WMI involve astroglial and microglial activation. Since reactive glia can promote chronic inflammation and the generation of factors deleterious to axonal survival, we tested the hypothesis that the burden of axonopathy would be greater in necrotic lesions with mixed glia reaction than in non-necrotic lesions with predominantly astroglial reaction. We undertook the first quantitative ultrastructural studies to define axonal integrity in chronic white matter lesions identified by high field MRI. Our findings support that axonal degeneration occurs in association with discrete foci of microscopic necrosis with pan-cellular loss, but is not detectible within large lesions with diffuse astrogliosis and preOL maturation arrest, which appears to be the primary mechanism of myelination failure in perinatal WMI.

MATERIALS AND METHODS

Animal Surgery: Surgery was performed on time-bred sheep of mixed western breed between 88–91d of gestation (term 145d) modified from a previously described protocol.(Riddle et al., 2006) Ewes with twin pregnancies were studied so that each experimental animal had a twin control. The ewe was initially anesthetized with intravenous ketamine (5 mg/kg) and diazepam (0.13 mg/kg), an endotracheal tube placed, and anesthesia maintained with 1% halothane in O_2 and N_2O. Maternal end tidal PCO_2 and oxygen saturation were monitored continuously. A midline laparotomy and a hysterotomy were performed in a sterile field and the fetus exposed. Vinyl catheters were placed in an axillary artery and a femoral vein. The vertebral-occipital arteries were isolated bilaterally and ligated with silk suture. In sheep, these anastomoses connect the vertebral arteries supplied by the thoracic aorta with the external carotid arteries that are fed by the common brachiocephalic.(Baldwin and Bell, 1963) A Hydraulic occluder (silastic) was placed on the common brachiocephalic artery. Finally, an amniotic fluid catheter was placed and one million units of penicillin G were given when the uterus was closed.

Physiological Monitoring. On the second or third post-operative day, at least 30 minutes prior to the start of the experiment, pressure transducers and a chart recorder (PowerLab 16/30, ADInstruments, Sydney, Australia) recorded pressure in the fetal artery relative to amniotic fluid (MABP). Fetal heart rate (HR) was calculated from triplicate measurements of the arterial pressure pulse intervals over a continuous recording of no less than 20 seconds.

Blood analysis. Blood samples (1 mL) taken anaerobically from the fetal axillary artery were analyzed for arterial pH_a, P_aO_2, P_aCO_2 corrected to 39°C, hemoglobin content (Thb), arterial oxygen saturation ($SatO_2$) and hematocrit (Hct; ABL725 blood gas analyzer, Radiometer

Medical A/S, Bronshoj, Denmark). After a 24 h recovery from surgery, fetuses were entered into the study if they demonstrated normal fetal oxygenation, defined as > 6 ml O_2/100 ml blood.

Cerebral Hypoperfusion Studies: Ischemia of 25 min duration was performed on the second or third post-operative day using a model similar to that previously reported.(Riddle et al., 2011) Briefly, mild fetal and maternal hypoxia was induced by administering a 11% O_2 air mixture to the ewe. After 10 minutes, sustained cerebral hypoperfusion was initiated by occlusion of the common brachiocephalic artery after inflation of the brachiocephalic occluder and reestablished by deflation of the brachiocephalic occluder. $There were no significant differences in the physiological responses of the animals in this study relative to animals from a prior cerebral hypoperfusion study(Riddle et al., 2011).

Tissue Processing: The ewe and fetuses were sacrificed (barbiturate overdose, Euthasol) at 1 (control, n=8; ischemia, n=8) or 2 (Control, n=8; ischemia, n=8) weeks following completion of the occlusion protocol. Heparin (1.5 mL) was administered to all fetuses via the umbilical vein. Half of the fetal brains from each of the groups (4 1 week control; 4 1 week H-I; 4 2 week control; 4 2 week H-I) were immersion fixed at 4° C in 4% paraformaldehyde in 0.1M phosphate buffer, pH 7.4 for 3 d and then stored in PBS for at least 60 days. The remaining fetal brains (4 1 week control; 4 1 week H-I; 4 2 week control; 4 2 week H-I) were perfusion fixed with 50 mL of 4% paraformaldehyde in 0.1M phosphate buffer, pH 7.4 followed by 1 L of 5% gluteraldehyde in 0.1M phosphate buffer, pH 7.4 administered by cannulation of the left ventricle. Immediately upon administration of the perfusion the descending aorta and pulmonary trunk were ligated and the jugular veins clipped bilaterally.

Gluteraldehyde fixed fetal brains were cut into five equivalent coronal blocks in proportion to the distance between the frontal and parietal poles (6–10 mm). All frontal blocks studied spanned from the genu of the corpus callosum to the optic chiasm.

Ex Vivo MRI: Tissue was embedded alongside a twin control tissue block from the same level in 0.5% agarose and immersed in PBS within a 4 cm diameter plexiglass tube. A custom single-turn solenoidal coil (5 cm diameter, 5 cm length) was utilized for radiofrequency transmission and reception. Experiments were performed using an 11.7 T magnet interfaced with a 9 cm inner diameter magnetic field gradient coil (Bruker, Rheinstetten, Germany). Procedures generally followed the previously published strategy that used diffusion tenser imaging (DTI) to characterize postmortem tissue from other species.(Kroenke et al., 2005; Kroenke et al., 2009) Detailed scanning and image segmentation procedures are provided in supplemental methods.

Immunohistochemistry: Tissue blocks were serially sectioned at 50 μm using a Leica VTS1000 vibrating microtome (Leica Microsystems Inc., Bannockburn, IL). The detailed immunohistochemical protocols to visualize specific cell types were performed as previously described.(Riddle et al., 2006; Riddle et al., 2011) Astroglia were visualized with rabbit glial fibrillary acidic protein (GFAP) antisera (1:500, Z-0334; DAKO, Carpinteria, CA). Microglia and macrophages were visualized with a rabbit anti-ionized calcium-binding adapter molecule 1 (Iba1) antibody (1:500; 019-19741; Wako Chemicals, Richmond, VA). Axons were visualized with the pan-axonal neurofilament marker, mouse monoclonal antibody SMI-312 (1:1000; SMI-312R; Covance, Berkley, CA). Mouse monoclonal beta app (β-APP; Millipore) and 3,3'-diaminobenzidine with nickel-enhancement (SK4100; Vector Laboratories) was used to visualize degenerating axons.

Electron Microscopy (EM): Two 2 x 1 x 1 mm blocks were dissected from regions of apparent diffuse white matter gliosis indicated by T2 hypointensities from MRI-scanned tissue blocks and corresponding controls. Tissues were processed for EM as described.(Back et al., 2007) Briefly, tissues were post-fixed in excess cacodylate-buffered 1% osmium tetroxide (pH 7.4), dehydrated, and embedded in epoxy resin. Cross sections (~900 nm thick) were stained with 1% toluidine blue and screened by bright-field microscopy. Thin sections (~90 nm) of regions of special interest were stained with 2% uranyl acetate followed by 1% lead citrate for examination by transmission EM.

Morphometric EM Studies: At least twelve images of each tissue block were randomly acquired at 56,400x magnification across the block. The total density of degenerating axons, intact axons and axon diameter was determined by a blinded individual in a minimum of twelve randomly acquired images for each block as previously described.(Partadiredja et al., 2003) Briefly, an unbiased counting frame (Fig. 1), which was 2 μm in width by 2 μm in length, was used for the measurement of the number of axons per 100 μm^2 and axon diameter. Axons were only counted when they were clearly identifiable. Axons were defined by cylindrical shape, a lack of ribosomes and the presence of at least one microtubule. Degenerating axons were distinguished by the presence of vacuolar bodies, disrupted plasma membrane, swollen mitochondria or dark axoplasm. Axons were counted and measured if they were partially in the counting frame and did not intersect the plane of the left side or bottom of the counting frame. The counting frame was superimposed randomly on each image (ImageJ). Axon diameter was determined by measuring the longest diameter perpendicular to the long axis of the axon in order to estimate the cross-sectional diameter (Fig. 1).

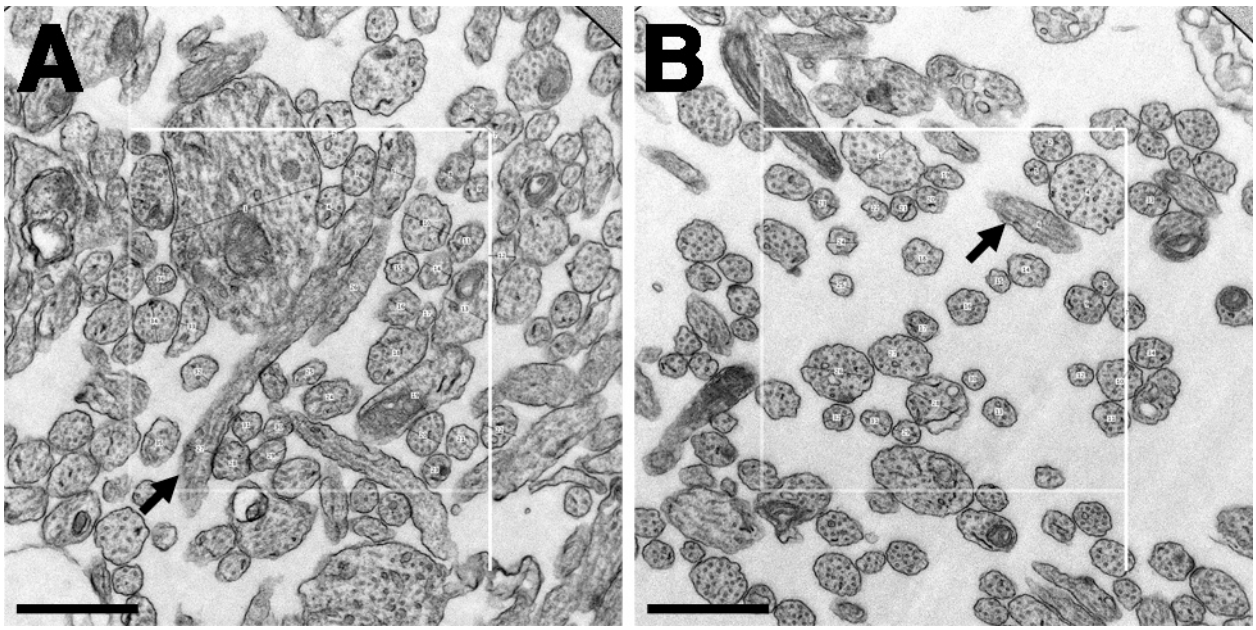

Figure 1. Stereological Analysis of axonal caliber and density. A and B, Example measurements of intact axons with an unbiased counting frame. A 4 μm^2 counting frame was randomly superimposed on electron microcraphs. The lines within numbered axons represents the axon diameter as measured. Obliquely cut axon diameters were measured perpendicular to the long axis of the axon (arrows). Scale bars: 667 nm.

Statistical analysis. Data analysis was performed using Prism 4 statistical software (GraphPad Software Inc., La Jolla, CA) except where noted. Data were expressed as means ± 1 SEM unless otherwise noted. Comparisons were performed using using ANOVA with *post hoc* inference testing done with Tukey's multiple comparison test. Because axon diameter data was not normally distributed, these data were analyzed with the Kruskal-Wallis non-parametric test for one-way ANOVA. $P<0.05$ was considered statistically significant.

RESULTS

Diffuse white matter gliosis was the major form of hypoxic-ischemic WMI.

In order to define the magnitude and distribution of axonopathy associated with hypoxia-ischemia (H-I)-induced WMI, we first employed high field MRI to identify early chronic lesions in animals that survived for 1 or 2 weeks. As recently described,(Riddle et al., 2011) high field MRI identified diffuse hypo-intense lesions in periventricular white matter that were visible on T_2-weighted images (T_2W) in H-I animals (Fig. 2B) but not controls (Fig. 2A). These diffuse lesions, present in all H-I animals, had FA and ADC values that did not differ from control. Histopathological analysis of diffuse lesions demonstrated that the MRI corresponded to non-necrotic WMI defined by increased reactive astrogliosis ($GFAP^+$) and mild microglial activation ($Iba1^+$). Consistent with recent observations, diffuse gliotic lesions were the major form of WMI in all animals, whereas necrotic foci were a minor component.(Riddle et al., 2011)

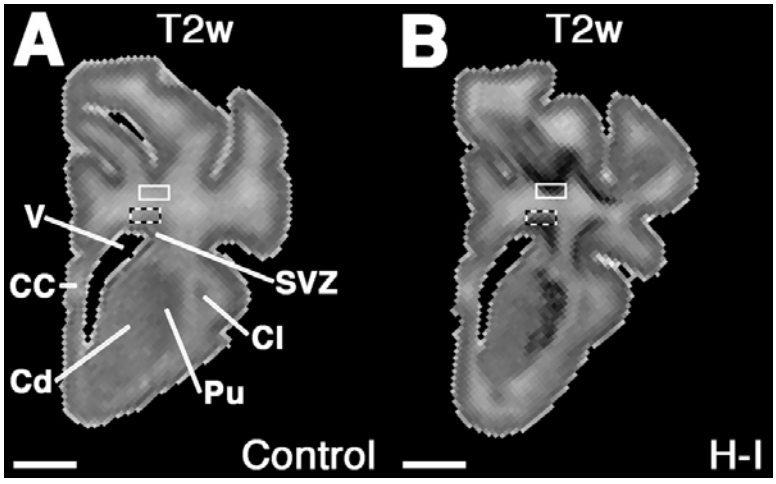

Figure 2. Tissue sampling for ultrastructural studies. A and B, Hemisected coronal t2-weighted image (T2w) from frontal control (A) and hypoxia-ischemia (H-I, B) blocks. MRI-scanned blocks were used to identify two regions of predilection for injury in the frontal WM indicated by the dark bands in B. Superficial (solid box) and deep (checkered box) blocks of 2 x 1 x 1 mm were excised from these locations in H-I animals and corresponding controls and processed for ultrastructural analyses. CC, corpus callosum; Cd, caudate; Cl, claustrum; Pu, putamen; SVZ, subventricular zone; V, lateral ventricle. Scale bars: 4 mm.

Axon injury markers are elevated in focal necrotic but not in diffuse non-necrotic WMI.

We next employed axon injury markers to define the burden of axonopathy in diffuse lesions and foci of necrosis in 1 and 2 week survivors. Staining for neurofilament protein (NF; SMI-312)

revealed that controls (Fig. 3A) and diffuse lesions (Fig. 3B) had normal-appearing axons. By contrast, at both 1 and 2 weeks, lesions with macroscopic necrosis or focal microscopic necrosis (Fig. 3C) displayed reduced NF-staining, axonal swellings and spheroids consistent with axonal degeneration. Staining for β-amyloid precursor protein (β-APP) also visualized foci of axonal degeneration (Fig. 3D). Thus, axonal injury markers did not localize to diffuse white matter gliosis, but were restricted to necrotic lesions.

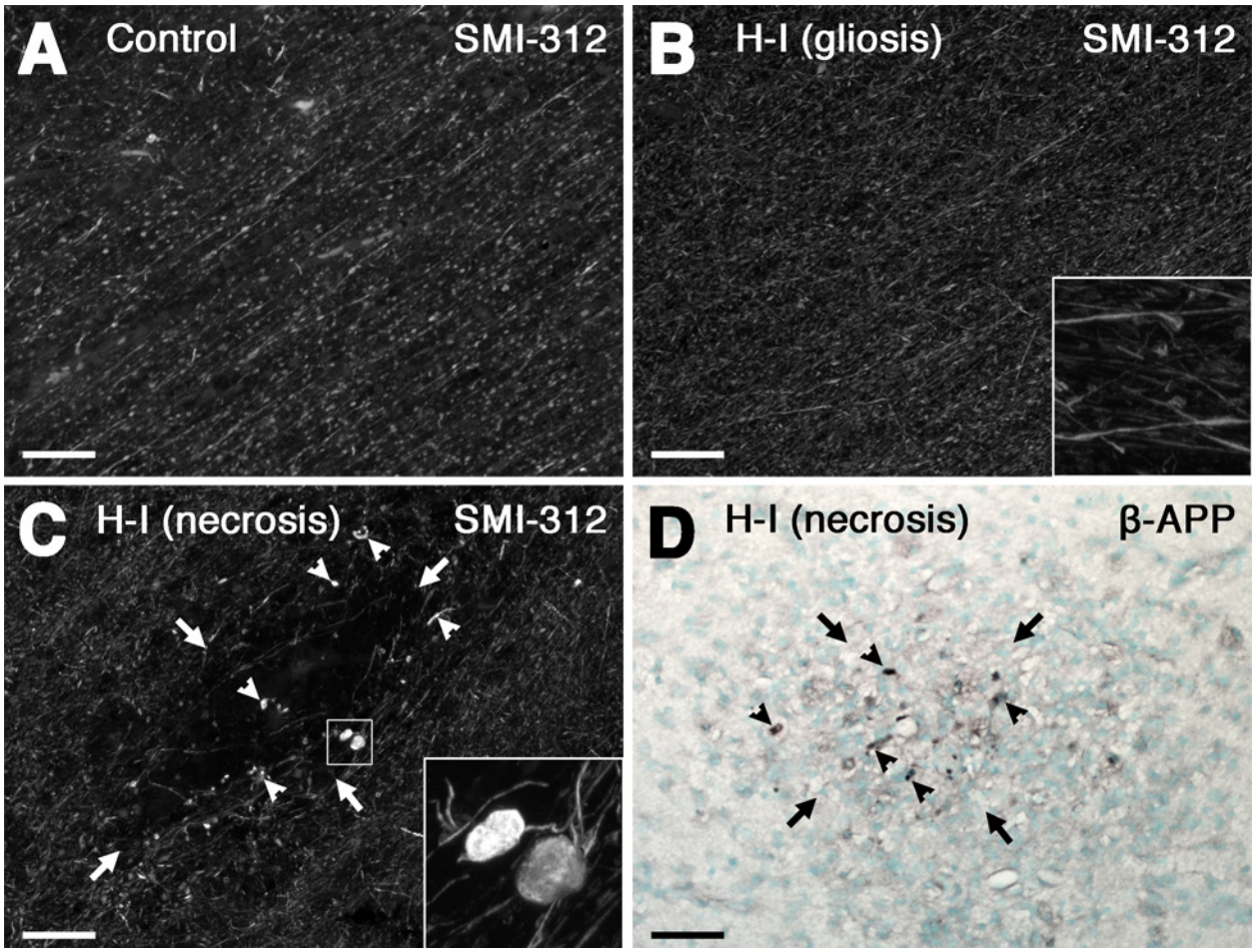

Figure 3. Immunohistochemical assessment of axonal integrity in chronic white matter lesions. A, Normal neurofilament staining (SMI-312) in control white matter. B, Neurofilament staining was intact in regions of diffuse gliosis and intact axons are visible at high magnification (B, inset). C, In a rare region of microscopic necrosis (arrows) multiple degenerating axons (arrowheads) with axonal spheroids (C, inset) are visualized with neurofilament staining in the core and immediately surrounding the necrotic focus. D, β-APP (black) staining reveals injured axons (arrowheads) within and immediately adjacent to a necrotic focus (arrows), but not in the

surrounding white matter. Nissl staining (green) is used to visualize nuclei. Scale bars: 100μm. Inset: 400μm^2.

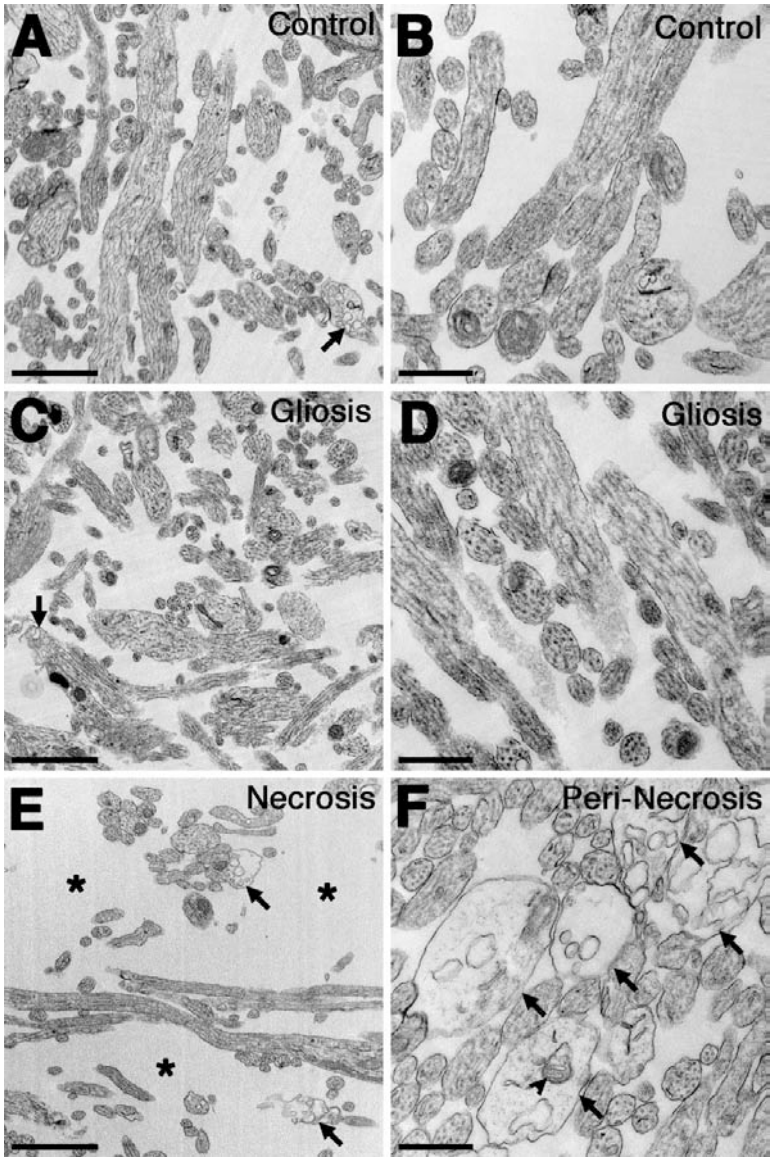

Figure 4. Ultrastructural characteristics of axons within regions of diffuse white matter gliosis. A and B, Examples of typical axonal ultrastructure observed within the white matter. An occasional degenerating axon was observed (arrow). C and D, The untrastructure of tissue and axons appeared intact within areas of diffuse white matter gliosis. Numerous intact appearing axons with normal axoplasm and intact microtubules and occasional degenerating axons with membrane swellings, swollen mitochondria, numerous vacuoles or loss of microtubules (arrow) were visible E, A necrotic focus imaged for comparison with evident unltrastructural damage. Large spaces appeared in the tissue with no axonal elements (*) as well as more frequent degenerating axons (arrows). F, Tissue adjacent to a necrotic focus contains numerous axons, but contains more profiles of degenerating axons (arrows). Scale bars: A, C, E, 2 μm; B, D, F, 500 nm.

Ultrastructural features of degenerating axons in diffuse WMI

We next addressed the possibility that immunohistochemical detection of axon injury markers may be relatively insensitive to some forms of axonal degeneration in diffuse gliotic lesions. To analyze the ultra-structural integrity of axons, we processed for electron microscopy (EM), a superficial and deep region of periventricular white matter that corresponded to diffuse WMI

identified by T_2W hypointensities from MRI-scanned tissue blocks and corresponding controls (insets, Fig. 2A, B).

In controls (Fig. 4A, B), degenerating axons were rarely visualized. Similarly, in lesions with diffuse WMI, rare degenerating axons were identified by the presence of vacuolar bodies, disrupted plasma membrane and swollen mitochondria (Fig. 4C, D). By contrast, in necrotic lesions, the number of axons was markedly reduced and degenerating axon profiles were frequently visualized (Fig. 4E, F).

Table 1. Ultrastructural Analysis of Axons

Region		**Axon Density** (axons/100μm^2)	**Degenerating Axon Density** (axons/100μm^2)
SWM			
1 wk	*Control*	332 ± 58	9 ± 2
	H-I	323 ± 41	11 ± 2
2 wk	*Control*	344 ± 68	11 ± 2
	H-I	310 ± 65	12 ± 1
DWM			
1 wk	*Control*	273 ± 24	8 ± 3
	H-I	321 ± 17	11 ± 1
2 wk	*Control*	410 ± 33 *	14 ± 3
	H-I	364 ± 47	15 ± 2

The number of axons, degenerating axons and axon caliber in areas of chronic WMI. Data are presented as mean ± SEM, n = 4 animals per group. * $p < 0.05$ vs. 1 week control (ANOVA with post hoc Tukey between groups).

Intact axon density is preserved in regions of diffuse WMI.

We next addressed the possibility that a gradual loss of axons may occur in diffuse WMI by 1 or 2 weeks after H-I and would be detected by counting the total number of axonal profiles present in random fields sampled by EM (Fig 1). In a blinded analysis of ~ 3000 intact axons per group, there were no significant changes in the density of either intact or degenerating axons between the control and H-I groups at either 1 or 2 weeks in either the superficial or deep periventricular white matter (Table 1). In the peri-callosal deep white matter from controls, a significant increase

in axon density occurred between 1 week (273 ± 24 axons/ 100 mm2) and 2 weeks (410 ± 33; $p < 0.05$) that reflected an apparent normal developmental expansion in the total population of axons.

The distribution of axon diameters is unaffected by diffuse WMI.

We next determined if a loss of axons in diffuse lesions would be detected as a change in the distribution of mean axonal diameters between controls and the H-I group. There was, however, no change in the mean axonal diameter in response to H-I at either 1 or 2 weeks (Table 1). Figure 4 shows the distribution of axonal diameters in the regions studied at 1 and 2 weeks. Anatomical differences in the distribution of fiber diameters and peak fiber diameters were present between the superficial (Fig 5A, B) and deep periventricular white matter WM (Fig. 5C, D), but H-I did not disrupt the normal developmental distribution of axon diameters in either region between 1 and 2 weeks after HI. Hence, diffuse white matter lesions showed no apparent axonal loss or disruption in the normal trajectory for axon development.

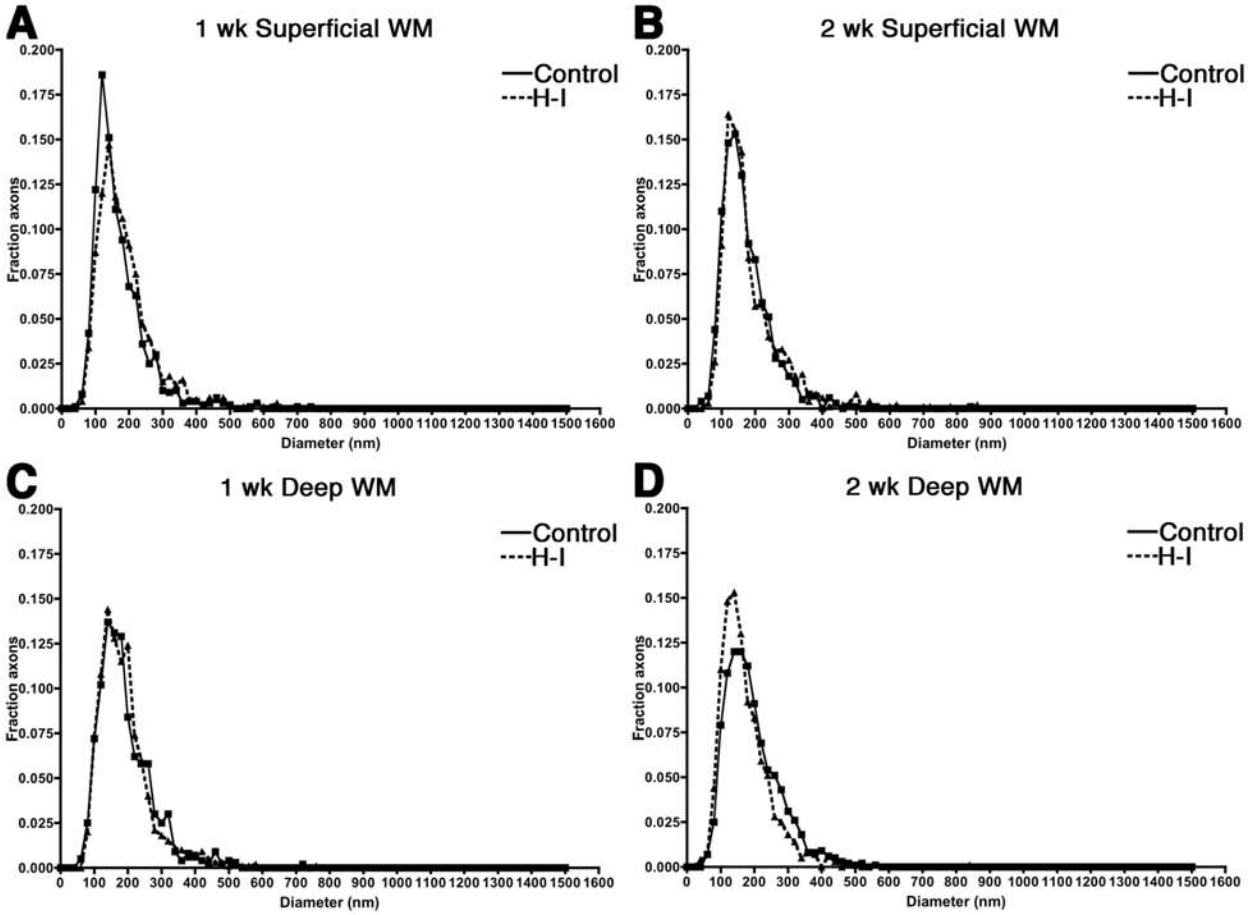

Figure 5. The fraction of axons of varying caliber after hypoxia ischemia. A through D, Histograms showing the fraction of axons of varying diameter in the white matter after hypoxia-ischemia (H-I; dashed line) or sham control (Control; solid line) as determined by stereological assessment. A, One week superficial block. B, Two week superficial block. C, One week deep block. D, Two week deep block. No change in the distribution of axonal diameters was found in either region at 1 or 2 weeks.

DISCUSSION

Failure of normal myelination is a major consequence of perinatal WMI, a common cause of cerebral palsy and cognitive impairment in survivors of premature birth.(Ferriero, 2004; Volpe, 2008) Failure to initiate myelination may be a consequence of disrupted maturation of oligodendrocyte progenitors(Segovia et al., 2008; Zhiheng et al., 2009) or loss of axonal integrity. The contribution of axonal injury to myelination failure has been resistant to study for several reasons. Several markers have been studied in developing white matter that identify degenerating axons in early necrotic lesions.(Arai et al., 1995; Haynes et al., 2008) However, the timing of WMI during premature brain development coincides with a period prior to the onset of myelination. Hence, it is not possible to apply markers of axonal integrity, such as nodal proteins, that are expressed later in development with the onset of myelination and are disrupted in dysmyelinated adult white matter.(Schafer and Rasband, 2006; Eftekharpour et al., 2007) Progress to define axon integrity also has been hampered by the lack of a large pre-clinical animal model that closely replicates the pathophysiology and spectrum of pathology in premature human periventricular white matter.(Ferriero, 2006)

We defined axonal integrity in a recently described model of chronic WMI in which global cerebral ischemia generates a similar spectrum and relative burden of pathology as seen in human.(Riddle et al., 2011) The periventricular white matter of the preterm fetal sheep at 0.65 gestation has few myelinated axons, consistent with the immature state of the white matter at this time in development. With this model, *ex vivo* high field MRI identified novel signal abnormalities that histologically correspond to microscopic necrosis and diffuse non-necrotic WMI. These lesions have been previously undetected at lower field strength.(Ferriero and Miller, 2010) Here we found striking differences in the burden of axonal degeneration in necrotic and

non-necrotic WMI that was defined by a combination of light and transmission electron microscopy.

Quantitative EM studies, guided by high field MRI, have not been applied before to study axon integrity. This approach allowed us to visualize both overt and subtle changes in the integrity of developing axons that are not currently feasible to detect by light microscopy alone. The most significant axonal degeneration was visualized in necrotic lesions. Lesions were confirmed to be necrotic by the presence of dystrophic axons and axonal spheroids, which degenerate during the early phase of coagulative necrosis.(Banker and Larroche, 1962; Deguchi et al., 1997; Marin-Padilla, 1997; Hirayama et al., 2001) Reduced myelination secondary to neuro-axonal degeneration is a prominent feature in perinatal rat models of hypoxia-ischemia.(Sizonenko et al., 2003; Sizonenko et al., 2005) Cerebral hypoxic-ischemic injury in rodents is typically more severe than in human and similar necrotic neuro-axonal injury is mostly associated with cystic necrotic lesions,(Pierson et al., 2007; Haynes et al., 2008) which now occur infrequently. Moreover, in human, neuronal loss is uncommon in cases where diffuse gliotic lesions comprise the major form of WMI.(Pierson et al., 2007) In such lesions, we have also not observed significant neuro-axonal injury in cerebral gray matter.(Riddle et al., 2011)

The burden of microsopic necrosis is unclear in human, since such lesions cannot be detected by MRI. However, in fetal sheep, we found that the burden of microscopic necrosis is very low.(Riddle et al., 2011) Here we found that most axonal degeneration was restricted to these small discrete lesions. The clinical significance of these lesions is unclear given their small size, but is likely to be influenced by the location of the lesion.

During development, small pre-myelinated axons are particularly susceptible to glutamate-mediated excitotoxicity at sites of contact with oligodendrocyte processes that

involves both N-methyl-D-aspartic acid (NMDA) receptors and non-NMDA glutamate receptors.(Fern et al., 1998; Alix and Fern, 2009) Glutamate-mediated axonal injury is related to a mechanism of excessive glutamate depletion from oligodendrocyes and axons,(Fern et al., 1998; Fern and Moller, 2000; Wilke et al., 2004; Salter and Fern, 2005) which appear to be the major sources of extracellular glutamate during energy failure from hypoxia-ischemia.(Back et al., 2007) Thus, one potential approach to prevent myelination failure in necrotic lesions may be to block axonal degeneration via pathways that mediate excitotoxic injury.(Domingues et al., 2010)

The paucity of axonal loss or degeneration in diffuse WMI supports that the mechanism of myelination failure in these lesions differs substantially from that in necrotic lesions. Despite the pronounced reactive astrocytosis and modest microgliosis in diffuse WMI,(Riddle et al., 2011) our data suggests that significant axonal degeneration does not coincide with reactive gliosis. Prior studies of acute WMI also found no overt axonal degeneration in either human or fetal sheep.(Back et al., 2005b; Riddle et al., 2006) Axonal injury has been observed in regions of diffuse WMI adjacent to large acute or organizing necrotic lesions.(Haynes et al., 2008) Since axons typically traverse long distances in central white matter tracts, it is not unexpected that individual axons that traverse large necrotic lesions display dystrophic features in adjacent non-destructive lesions. Such lesions are now clinically uncommon and our data supports that significant axonopathy does not occur in diffuse lesions in the absence of large necrotic lesions. Although there was no structural evidence of abnormal axons, we cannot exclude the possibility that reactive glia generate a chronic inflammatory response that results in axonal dysfunction. Electrophysiological studies would be needed to address this possibility.

An alternative mechanism for myelination failure in diffuse WMI involves disturbances in oligodendrocyte (OL) lineage maturation. Preterm neonates are susceptible to acute diffuse WMI that is triggered by selective vulnerability of pre-oligodendrocytes (preOLs; late OL progenitors) as opposed to other glia, neurons or axons.(Back et al., 2002; Back et al., 2005b) Acute degeneration of preOLs triggers reactive astrogliosis and a compensatory increase in preOLs that fail to differentiate to mature OLs.(Segovia et al., 2008; Zhiheng et al., 2009; Riddle et al., 2011) Thus, preOL maturation arrest within areas of astrogliosis may significantly contribute to chronic myelination failure in preterm survivors.

In summary, our findings support that axonal degeneration occurs in association with discrete foci of microscopic necrosis with pan-cellular loss. Axonopathy was not detectible within large lesions with diffuse astrogliosis and preOL maturation arrest. Hence, the primary mechanism of myelination failure in perinatal WMI appears to involve an aberrant reaction to injury in which preOLs mount a disrupted repair response with arrested maturation. Hence, therapies directed at prevention of axonal degeneration would optimally target mechanisms related to necrotic WMI, whereas in diffuse lesions, alternative strategies will be required to reverse myelination failure that is related to preOL maturation arrest. One strategy may be to target the accumulation of hyaluronan within the extracellular matrix of diffuse astrogliotic white matter lesions. Within adult demyelinating lesions, hyaluronan triggers the arrest of preOL maturation.(Back et al., 2005a; Sloane et al., 2010)

SUMMARY AND CONCLUSIONS

Area of Focus

Perinatal white matter injury (WMI) is a major cause of chronic neurological morbidity and mortality in children (Volpe, 2008). In a large population-based study of children with cerebral palsy (CP), WMI was the most common finding, and was seen in almost half of affected children (42.5%) (Bax et al., 2006). Due to the non-progressive nature of the motor deficits, CP is often considered a static encephalopathy that results from destructive processes and has limited potential for recovery or repair. This notion has hampered the development of therapeutic strategies. The central aim of my research is to define the pathogenic mechanisms of cerebral injury in survivors of premature birth, in order to gain insight into potential therapeutic strategies to repair the myelination disturbances related to cerebral palsy and cognitive deficits.

Methodological Advances

We undertook several novel methodologies to quantitatively analyze factors hypothesized to contribute to the pathogenesis of selective WMI.

- An integrated analysis of cerebral blood flow was developed using fluorescently-labeled microspheres that was used to quantify regional fetal cerebral blood flow in utero.
- A systematic and rapid estimate of GFAP- and Iba1-stained cellular area was developed to determine the magnitude of astrocyte activation in order to replace bias prone ordinal rating scales.

- Novel registration algorithms were used to identify unique histopathological characteristics of distinct classes of lesions identified by high-field-MRI.

Key Findings

We developed a large pre-clinical model in preterm fetal sheep that yielded the following novel findings in support of a significant role for a mechanism of ischemic injury in acute WMI:

- Graded WMI was generated that was proportional to the duration of ischemia.
- Selective WMI ranged from discrete focal lesions to diffuse injury that reproduced the spectrum of injury seen in human.
- The periventricular white matter (PVWM) displayed a lower threshold for injury than cortical or subcortical gray matter or the subventricular zone.
- There was lower blood flows in PVWM than in gray matter, but this did not account for the distribution of white matter damage.
- The heterogeneity of WMI coincided with greater immaturity of the OL lineage stages present in vulnerable regions of PVWM.
- Selective WMI resulted in cell death that spared most glial cell types and primarily involved pre-myelinating stages in the OL lineage that degenerated via a caspase-3-dependent mechanism.
- No evidence of blood flow heterogeneity that could explain the WM injury pattern was found during ischemia or reperfusion.

We further developed this model of chronic cerebral WMI where animals were studied at 1 or 2 weeks after global cerebral ischemia. Novel registration algorithms were applied to define the potential of high-field MRI to distinguish distinct types of histopathologically-defined injury.

- A spectrum of chronic WMI was generated similar to that commonly observed in human preterm survivors.(Buser et al.) Thus, WMI with focal or diffuse astrogliosis predominated and necrotic lesions were infrequently observed.
- Despite the fact that preOL degeneration predominates in early WMI,(Back et al., 2005b; Riddle et al., 2006) chronic lesions contained an expanded population of preOLs that failed to differentiate to OLs. There was, thus, a net increase in total preOLs in lesions, that also fully compensated for acute and delayed preOL degeneration.
- PreOL maturation arrest was directly associated with the magnitude of astrogliosis, which supported that diffuse astrogliosis is a surrogate marker for lesions with arrested preOL differentiation.
- Consistent with volumetric MRI studies in human preterm survivors,(Inder et al., 2005) chronic WMI was accompanied by a significant reduction in white matter growth.
- Novel registration algorithms demonstrated that high-field MRI distinguished three major types of chronic WMI.

- It was feasible to register both large diffuse WM lesions at the sub mm level and discrete focal lesions less than 500 μm in diameter that were identifiable by MRI and histopathology.
- High-field MRI was up to 100% sensitive and 92% specific for histopathologically-defined astrogliotic lesions larger than 2.5 mm^3. Large lesions comprise greater than 97% of total lesion burden.
- Significant axonopathy was not present in diffuse lesions that were the major form of WMI. Thus, we identified that the major form of WMI comprised a diffuse form of astrogliosis with preOL arrest without significant axonopathy.
- The spectrum of pathology observed in this animal model closely resembles that observed from human neuropathology studies from our lab; thus supporting the significant advantages of this model for hypothesis-driven studies that are not readily feasible with human autopsy tissues.

In order to address the burden of axonopathy within chronic white matter lesions, we applied our stereological and registration techniques to an ultrastructural analysis of axonal injury burden in chronic WMI at 1 and 2 weeks.

- Consistent with the immature state of the white matter, almost all axons were in an unmyelinated state and myelinated axons were rare.
- Degenerating axons visible by light miscroscopy and ultrastructure were frequently observed in and immediately surrounding rare foci of microscopic necrosis.

- No change in the number of degenerating axons, density of degenerating axons, axonal caliber or the distribution of axonal calibers was found one or two weeks after ischemia in two regions of diffuse WMI, the major form of WMI.

Summary

Until recently, the mechanism of acute degeneration of vulnerable preOLs was unresolved. Direct depletion of preOLs in the white matter during acute ischemia was a longstanding hypothesis for myelination failure (Volpe, 2008). This distribution of injury was considered to be due to the existence of apparent vascular end zones in the developing white matter that were poorly perfused by beds of long and short penetrating arteries that might account for the distribution of WMI (Greisen and Borch, 2001; Volpe, 2001). Cerebral blood flow measurement techniques were previously unable to reliably determine blood flow in susceptible regions, deep in the human white matter. In addition, small animal models have been relatively uninformative due to the relative lack of white matter in lissencephalic animals, the severe nature of the mixed gray and white matter damage and the technical limitations of invasive blood flow measurements (Back, 2001).

In order to address these shortcomings, we developed an in situ measurement of cerebral blood flow using fluorescently-labeled microspheres in the preterm fetal sheep to address the degree to which the pattern of injury in the white matter coincided with the regional variations in oligodendrocyte (OL) maturation (Riddle et al., 2006). We employed a well-established model of cerebral hypotension in the instrumented 0.65 gestation fetal sheep where cerebral ischemia was induced by reversible inflation of bilateral carotid occluders in an unanesthetized state. This model generated a graded

response to injury where damage varied from selective non-necrotic WMI to extensive cortical and subcortical gray matter injury and white matter necrosis with increasing durations of ischemia. Thus, the model was able to generate the pattern and spectrum of injury observed in human survivors of premature birth. We found that flow to the vulnerable periventricular white matter, although absolutely lower both before and during ischemia, dropped proportionally to other regions of the cerebral cortex and white matter during ischemia. Furthermore, regions of the periventricular white matter with greater degrees of injury did not suffer a greater degree of ischemia than those with less injury. During reperfusion, blood flow in the periventricular white matter remained proportional. Thus, it seemed unlikely that vascular factors drive the pattern of injury to the white matter.

We next considered whether cellular maturational factors might play a greater role in defining the injury pattern. Another longstanding hypothesis on the origin of myelination disturbances was that the specific loss of OL progenitors might deplete the pool of cells available to become mature myelinating OLs (Back and Volpe, 1999). The developmental window for the highest incidence of selective WMI corresponds to the period when OLs in the white matter are predominantly in the preOL stage, 24 to 32 weeks, before the maturation of OLs to immature OLs and the onset of myelination (Back et al., 2001). It is well established that the preOL is vulnerable to oxidative stress in vitro and ischemia-reperfusion in vivo compared to more mature OL stages (Back et al., 1998; Fern and Moller, 2000; Back et al., 2002; Baud et al., 2004; Fragoso et al., 2004; Lin et al., 2004). Targeted loss of preOL has also been observed in autopsy studies of human infants with WMI (Back et al., 2005b). In these studies, loss of preOLs was

observed in areas with increased signs of oxidative stress, including lipid peroxidation products that accumulate during oxidative stress. Thus, the susceptibility of the white matter seems related to the relative population of OL lineage cells present within the white matter, with decreasing vulnerability as the OL population becomes more mature.

We observed that the white matter of the 0.65 gestation fetal sheep has heterogeneous OL lineage maturation in the periventricular white matter, with relatively immature white matter rich in preOLs medially and more mature immature OLs predominating laterally (Riddle et al., 2006). We used this observation to test whether oligodendroctyte maturation was able to predict the relative susceptibility of medial and lateral periventricular white matter to ischemic injury. Indeed, we found that injury in the periventricular white matter was non-uniform. The medial portion of the periventricular white matter contained almost three times more acutely degenerating OLs and suffered twice the depletion of OLs than the lateral white matter. Thus, the relative predominance of preOLs in the medial white matter coincided with the susceptibility of this region to ischemia, while we were unable to find any differences in blood flow between these regions. Moreover, when we examined other components of the white matter, including microglia, astrocytes and axons, we were unable to find any evidence of degeneration at the durations of ischemia that produced selective WMI. Taken together, these findings suggest that although perturbations in cerebral blood flow are necessary, to damage the periventricular white matter, that the predilection and pattern of acute WMI is related to the appearance and maturation of vulnerable preOLs.

However, this is not sufficient to explain myelination failure. Our studies in fetal sheep found that approximately half of preOLs were acutely depleted in white matter

lesions. Reduction in the number of preOLs is incomplete in both human and animal studies, indicating that ablation of this population may not be the mechanism of myelination failure in chronic WMI (Back et al., 2002; Back et al., 2005b; Riddle et al., 2006). The preOL is a simple multipolar, mitotically active late OL progenitor. The white matter is also enriched in OL progenitors, which are mitotically active and produce preOLs. Recent studies have shown that initial preOL vulnerability and death is followed by a period of increased preOL and OL progenitor proliferation combined with a failure of these cells to differentiate into myelinating OLs (Segovia et al., 2008). Thus, direct depletion of preOLs during acute ischemia, does not sufficiently explain observations of preOL expansion after ischemia.

The propensity for myelination failure in chronic WMI is the central pathological feature that distinguishes brain injury in the preterm survivor from other forms of CP that principally involve gray matter. Until recently, the prevailing hypothesis for the pathogenesis of cerebral palsy in premature infants was that acute degeneration of preOLs led directly to depletion of the pool of myelinating OLs and resulted in myelination failure (Back and Volpe, 1999). Since we had addressed the acute mechanism of preOL degeneration, we next examined how acute loss of vulnerable, but potentially proliferative preOLs leads to myelination failure. We felt that the 0.65 gestation fetal sheep was the ideal model system to determine if preOLs repopulate lesions in a preclinical animal model of selective WMI. However, in fetal sheep, as in rodents, we found that chronic white mattesr lesions undergo partial regeneration and repair due to novel injury response mechanisms intrinsic to oligodendrocyte progenitors (Riddle et al., 2011). PreOLs repopulate astrogliotic fetal ovine lesions within weeks of

injury. By several weeks after injury, these cells persist within lesions in proportion to the degree of gliosis. However, accumulating preOLs fail to generate OLs in regions of diffuse reactive astrogliosis. These findings challenge the long-standing view that myelination failure in WMI results from irreversible loss of preOLs that generate mature myelinating OLs. They support a more complex mechanism of myelination failure whereby a combination of proliferative and arrested maturational processes result in a net expansion in the pool of preOLs with potential to generate OLs.

Cell proliferation and maturation arrest is accompanied by a marginal increase in cell death processes that we found to be largely mediated through caspase-3 independent mechanisms. Cell death observed in the fetal sheep was much less severe than that previously observed in the rat (Segovia et al., 2008). By contrast, the chronic white matter lesions in the rat are predominantly of a mixed gray and white matter type that generated severe ongoing caspase-3-mediated degeneration of preOLs. Thus, endogenous proliferative and survival rather than death appear to be the predominant mechanisms acting on preOLs in chronic diffuse gliotic lesions in the fetal sheep.

The relative burden and significance of lesions characterized by diffuse astrogliosis and preOL maturation arrest is controversial. Pathological findings of WMI range from cystic necrotic foci, periventricular leukomalacia (PVL) to diffuse myelination failure (Kinney and Back, 1998; Volpe, 2001). Due to advances in neonatal intensive care, the major pathological lesion associated with WMI has shifted from PVL to diffuse WMI (Counsell et al., 2003; Inder et al., 2003; Miller et al., 2003; Chau et al., 2009). MRI studies now define either focal or diffuse white matter changes in intact tissue as the major type of lesion. Pathological studies support that a milder form of necrotic lesion

that involves microscopic necrosis is frequently found in cases of chronic WMI, and microscopic necrosis has been advanced as the primary pathology in WMI (Volpe, 2009). Due to their small size, microscopic lesions may be underappreciated in neuroimaging studies and the burden of microscopic necrosis and its contribution to myelination failure in chronic lesions was unresolved.

Undertaking a unique combined neuroimaging and histopathological approach in the fetal sheep, we defined the relative burden of the three major types of pathology found in chronic survivors of premature birth (Riddle et al., 2011). We developed registration algorithms for MRI and histopathology data to be applied to a complex gyrencephalic brain. There are still no effective solutions for solving the 2D to 3D registration necessary to place and analyze single sections in a volume such as MRI data. Other registration techniques have commonly relied on internal or external fiduciary markers to align datasets (Lazebnik et al., 2003; McGrath et al., 2010), or been performed in less complex lissincephalic animals (Lebenberg et al., 2010). We used serial sectioning techniques and ImageJ image analysis software to generate a 3D histopathological model. FSL and the ITK toolkit were then used to register, align and warp 3D MRI data to that model. The availability of powerful, free, open source image analysis programs now makes overcoming the challenges of accurate registration between modalities feasible in complex brain regions. These techniques can be applied broadly to questions about the pathological basis of neuroimaging findings. With these novel algorithms, we identified three major types of MRI-defined lesions, each of which had distinct histopathological features that corresponded to diffuse gliosis, microscopic necrosis and white matter necrosis. Two of these injury types were identified with high sensitivity and specificity

by novel MRI signal abnormalities that have not been previously described. Thus, high field imaging has the potential to identify pathology that has not been detected in previous clinical and experimental studies performed at lower field strengths. By far the most commonly observed and largest chronic lesions involved diffuse astrogliosis without necrosis, comprising approximately 80-90% of lesion volume at 1 and 2 weeks. Large focal necrotic lesions with the characteristics of PVL were detected in a minority of cases, and made up only 10-15% of lesion volume. While small regions of microscopic necrosis less than 1 mm across were detected in half of animals at 2 weeks, these lesions comprised only 2% of the lesion volume. Thus, our data supports the notion that diffuse white matter gliosis, rather then PVL, is now the major type of lesion in cases of WMI. However, our data also disputes the hypothesis that white matter necrosis is the dominant form of WMI, further supporting that preOL maturation arrest may be the primary mechanism of myelination failure.

Several studies have reported that both microscopic necrotic and diffuse astrogliotic white matter lesions can involve widespread axonopathy and the contribution of axonopathy to myelination failure remains controversial (Pierson et al., 2007). It is difficult to determine the integrity of axons by classical light microscopic neuropathological techniques in the deep white matter. Therefore, we applied our novel techniques to a stereological analysis of axonal ultrastructure in MRI-defined regions of necrotic and non-necrotic white matter lesions. We first employed both MRI and immunohistochemical markers of injury to define regions with focal necrosis and diffuse white matter gliosis. Although axonal pathology was found in association with rare areas of microscopic necrosis, it was not present in the predominant diffuse astrogliotic lesions.

Stereological approaches were used to determine the density of degenerating axons, total axons and axonal diameter. No change in any of these features was present in the lesion group relative to control. Thus, this study indicates that axonopathy does occur in association with rare areas of microscopic necrosis, but is not a feature of diffuse white matter gliosis. These results limit the potential contribution of irreversible axonal degeneration to myelination failure and support the hypothesis that myelination failure arises due to a failure of an expanding population of preOLs in the glial scar to differentiate into mature OLs.

Future Directions

Although significant progress has been made to define the pathogenesis of WMI, several questions about the mechanisms of myelination failure in survivors of premature birth remain. We observe that initial preOL death is followed by a period of increased preOL and OL progenitor proliferation combined with a failure of these cells to differentiate into myelinating OLs. Further studies are required to determine the mechanism of chronic myelination failure after acute WMI. Arrested maturation of OLs observed in gliotic lesions may be due to altered intrinsic cell fate signaling or an altered environment. A novel mechanism of myelination failure recently identified in a model of chronic adult demyelinated lesions is related to the presence of the extracellular matrix molecule HA, a glycosaminoglycan and the principle ligand for the transmembrane receptor CD44 (Back et al., 2005a). In vertebrates, HA is comprised of unbranched, repeating disaccharide units of glucuronic acid and N-acetyl-D-glucosamine that range in molecular mass from ~2 $x10^5$ to ~$10x10^6$ Da, and has size-dependent activities. In the CNS, HA is synthesized

predominantly by astrocytes where it is localized in the interstitial space between myelin and astrocyte processes (Asher et al., 1991; Eggli et al., 1992). Accumulation of high-molecular weight HA in vivo blocks remyelination in adult demyelinated lesions by a mechanism that involves arrest of OL lineage maturation (Back et al., 2005a). HA also reversibly inhibited OL progenitor maturation in vitro (Back et al., 2005a). Therefore, myelination failure in WMI may be related to the chronic accumulation of HA in astrogliotic lesions that blocks preOL maturation.

Myelination failure and accumulation of preOLs resulted in a persistent state of vulnerability of the white matter to hypoxia ischemia in rodents. Animals that underwent a recurrent episode of hypoxia had significantly increased acute degeneration of preOLs in chronic lesions compared to age-matched controls (Segovia et al., 2008). A single incidence of WMI and the formation of a persistent glial scar that causes preOL maturation arrest may extend the period during which susceptible preOLs predominate in the white matter. This could lengthen the period of white matter vulnerability, and increase the risk of further insult. Future studies in a preclinical model are needed to determine whether preOL maturation arrest confers increased vulnerability to the white matter and for how long this may persist.

Although myelination failure remains the central finding in acute WMI, it is unclear whether this is a permanent state. Due to the difficulty in obtaining appropriate contemporary tissue samples, it is currently unknown whether glial scars in preterm survivors resolve or remyelinate over longer periods of time. The fetal sheep model is ideal to determine if repair processes like those observed in the adult rodent can be found in a preclinical fetal model system, or, if like persistent cell death, there are significant

differences in cellular repair mechanisms. Furthermore, studies are needed to establish if arrested preOLs are functionally equivalent to normal preOLs and have a normal capacity for myelination if the appropriate cues for differentiation were restored.

Although it is not established if remyelination may eventually occur in preterm survivors, MRI evidence of gray matter loss in chronic survivors of premature birth has established that volume loss of cortical and deep nuclear gray matter is a frequent persistent sequela of WMI (Inder et al., 2005). However, the neuropathological basis for these lesions is unknown. The fetal sheep is the only known model system that faithfully reproduces these neuroimaging findings. In our study of the acute vulnerability of white and gray matter structures to varying durations of ischemia we determined that acute neuronal injury was not a significant contribution to selective white matter lesions, although cortical lesions could be generated at longer durations of ischemia. Despite this, we found that by 2 weeks after ischemia cortical volume was significantly reduced. Chronic studies should be used to determine if cortical volume loss persists into the period of rapid maturation that occurs near term. It is currently unclear if this volume loss is due to ongoing cell death in neurons, or due to a change in the organization or maturation of the cerebral cortex. In the future, analyses of cortical neuronal type, number, morphology and electrophysiology should be performed to determine the pathogenesis of cortical volume loss.

Although MRI is the optimal imaging modality to define WMI in preterm survivors (Ment et al., 2009; Miller and Ferriero, 2009; Mathur et al., 2010; Rutherford et al., 2010), there is limited ability to directly detect WMI in the developing brain. We identified novel high-field contrast that is able to distinguish diffuse gliosis and

microscopic necrosis, which was thought to be the primary component of noncystic WMI. We were able to determine that the majority of lesions are diffuse gliosis while microscopic necrosis makes up a small fraction. Improved detection of these lesions could provide significant improvements in the diagnosis of WMI. However, we have found that the T_2w contrast observed in gliotic lesions at 12T is not observed at 3T. Thus, the MRI field strength of current clinical scanners may limit our capacity to diagnose diffuse gliosis and microscopic necrosis. Future studies to determine the biochemical source of this novel field-dependent contrast could provide insights into how to optimize scanning parameters to make better MRI detection parameters available in clinical situations. These data emphasize the need to determine the clinical-translational utility of high-field MRI for improved diagnosis of perinatal WMI.

Conclusions

Our data in this large preclinical animal model challenged several long-standing views on the pathogenesis of myelination failure in preterm infants. We established that the distribution of preOL injury is related to cellular maturational patterns rather than vascular susceptibility. Our data also strongly supports that WMI involves a disrupted cellular repair mechanism that results in an expanded pool of OL progenitors that do not undergo significant delayed cell death and fail to differentiate to myelinating cells, while other cellular elements including axons remain intact within lesions. Furthermore, our large preclinical animal model is poised to provide access to experimental questions related to the mechanisms of myelination failure in chronic lesions as well as definition of the optimal field strength and modality to resolve evolving lesions by MRI. These

studies will be essential for the identification of potential strategies and the windows after injury when myelination failure might be addressed. Our findings indicate that one such therapeutic strategy may involve altering the composition of the gliotic lesions to promote maturation of accumulating arrested preOLs.

APPENDIX

Papers & Awards in Pursuit of Degree

Original Research Papers

(1) **Riddle A**, Luo NL, Manese M, Beardsley DJ, Green L, Rorvik DA, Kelly KA, Barlow CH, Kelly JJ, Hohimer AR, Back SA. Spatial heterogeneity in oligodendrocyte lineage maturation and not cerebral blood flow predicts fetal ovine periventricular white matter injury. *J Neurosci*. 2006 Mar 15;26(11):3045-55.3. *Cover*

(2) Broughton SK, Chen H, **Riddle A**, Kuhn SE, Nagalla S, Roberts CT Jr, Back SA. Large-scale generation of highly enriched neural stem-cell-derived oligodendroglial cultures: maturation-dependent differences in insulin-like growth factor-mediated signal transduction. *J Neurochem*. 2007 Feb;100(3):628-38.

(3) McClure MM*, **Riddle A***, Manese M, Luo NL, Rorvik DA, Kelly KA, Barlow CH, Kelly JJ, Vinecore K, Roberts CT, Hohimer AR, Back SA. Cerebral blood flow heterogeneity in preterm sheep: lack of physiologic support for vascular boundary zones in fetal cerebral white matter. *J Cereb Blood Flow Metab*. 2008 May;28(5):995-1008. *Denotes authors contributed equally to this work.

(4) Segovia KN, McClure M, Moravec M, Luo NL, Wan Y, Gong X, **Riddle A**, Craig A, Struve J, Sherman LS, Back SA. Arrested oligodendrocyte lineage maturation in chronic perinatal white matter injury. *Ann Neurol*. 2008 Apr;63(4):520-30.

(5) Buser J; Segovia KN; Dean J, Nelson K; Beardsley DJ, Gong X, Luo, NL; Ren J, Wan Y, **Riddle A**, McClure MM, Ji X, Derrick M, Back SA Tan S. Timing of Appearance of Late Oligodendrocyte Progenitors Coincides with Enhanced Susceptibility of Preterm Rabbit Cerebral White Matter to Hypoxia-Ischemia. *J Cereb Blood Flow Metab*. 2009 2010 Jan 13.

(6) **Riddle, A**, Dean JM, Buser, JR, Gong X, Maire J, Chen K, Ahmad T, Chen V, Nguyen T, Kroenke CD, Hohimer AR and SA Back. Histopathological correlates of MRI-defined chronic perinatal white matter injury, *Annals Neurol*, Epub ahead of print.

(7) Dean JM, **Riddle, A**, Maire J Hansen KD, Preston M, Barnes AP Sherman LS and SA Back. An organotypic slice culture model of chronic white matter injury with maturation arrest of oligodendrocyte progenitors, *Molecular Neurodegeneration*, Epub ahead of print.

(8) Buser, JR, Maire, J, **Riddle, A**, Nelson, K, Gong, X, Luo, NL, Ren, J, Nguyen, T, Struve, J, Sherman, LS, Miller, SP, Chau, V, Hendson, G, Ballabh, P Grafe, MR and SA Back, Myelination failure in human perinatal white matter injury: A disrupted cellular repair mechanism linked to pre-oligodendrocyte maturation arrest, *Annals Neurol*, in press.

(9) **Riddle, A** Maire J, Gong X, Kroenke CD, Hohimer AR and SA Back. Differential susceptibility to axonopathy in necrotic and non-necrotic perinatal white matter lesions. *Stroke*. In Press.

Reviews

(1) Back SA, **Riddle A**, Hohimer AR. Role of instrumented fetal sheep preparations in defining the pathogenesis of human periventricular white-matter injury. *J Child Neurol*. 2006 Jul;21(7):582-9. Review.

(2) Back SA, **Riddle A**, McClure MM. Maturation-dependent vulnerability of perinatal white matter in premature birth. *Stroke*. 2007 Feb;38(2 Suppl):724-30. Review.

Posters

37th Annual meeting for the American Society for Neurochemistry, 2006 Spatial heterogeneity in oligodendrocyte lineage maturation and not cerebral blood flow predicts fetal ovine white matter injury. **Riddle A**, Luo NL, Manese M, Beardsley DJ, Green L, Rorvik DA, Kelly KA, Barlow CH, Kelly JJ, Hohimer AR, Back SA. Poster.

Presentations

(1) Northwest Pediatric Neurology Colloquium, 5/19/2006. "Perinatal white matter injury: a new experimental model relevant to pathogenesis and prevention."

(2) Northwest Pediatric Neurology Colloquium, 6/22/2007. "Brain injury in survivors of premature birth: have we been thinking about this all wrong?"

(3) Neuroscience Graduate Program Retreat, 9/22/09. "Brain Injury in Survivors of Premature Birth. Changing perspectives in white matter injury"

(4) Child Neurology Society 37th Annual Meeting, Neurobiology of Disease in Children Symposium, 11/6/08. "Blood flow is necessary but not sufficient to predict the pattern of white matter injury in preterm fetal sheep"

(5) Portland ARCS Society Annual Meeting 10/20/09. "Brain Injury in Survivors of Premature Birth: New insights into pathogenesis?"

(6) Oregon Society for Neuroscience 2010 Annual Meeting 3/26/10. "High-Field-Strength Imaging of Perinatal White Matter Injury in the Immature Fetal Sheep"

(7) Hershey Conference on Developmental Brain Injury 2010 6/5/10. "Mechanisms of Chronic Perinatal White Matter Injury in the Immature Fetal Sheep"

(8) Pediatric Neuroscience Seminar Series, 1/19/2011. "Histopathological Correlates of MRI-Defined Chronic Perinatal White Matter Injury"

Awards

(1) Portland ARCS Society Scholarship, 2007

(2) Child Neurology Society Young Investigator Award, 2008

(3) Banker Training Grant, 2007

(4) Grompe Training Grant, 2009

(5) Neurorenew Course Scholarship in Confocal Microscopy and Stereology, 2010

(6) NRSA (F30) award, 2010

REFERENCES

Abramoff M, Magelhaus P, Ram S (2004) Image Processing with ImageJ. Biophotonics International 11:36-42.

Alix JJ, Fern R (2009) Glutamate receptor-mediated ischemic injury of premyelinated central axons. Ann Neurol 66:682-693.

Ando M, Takashima S, Mito T (1988) Endotoxin, cerebral blood flow, amino acids and brain damage in young rabbits. Brain Devel 10:365-370.

Arai Y, Deguchi K, Mizuguchi M, Takashima S (1995) Expression of b-amyloid precursor protein in axons of periventricular leukomalacia brains. Pediatr Neurol 13:161-163.

Asher R, Perides G, Vanderhaeghen J, Bignami A (1991) Extracellular matrix of central nervous system white matter: demonstration of an hyaluronan-protein complex. J Neurosci Res 28:410-421.

Back S, Craig A, Luo N, Ren J, Akundi R, Rebeiro I, Rivkees S (2006a) Protective effects of caffeine on chronic hypoxia-induced perinatal white matter injury. Ann Neurol 60:696-705.

Back S, Tuohy T, Chen H, Wallingford N, Craig A, Struve J, Luo N, Banine F, Liu Y, Chang A, Trapp B, Bebo J, BF, Rao M, Sherman L (2005a) Hyaluronan accumulates in demyelinated lesions and inhibits oligodendrocyte progenitor maturation. Nat Med 9:966-972.

Back SA (2006) Perinatal white matter injury: The changing spectrum of pathology and emerging insights into pathogenetic mechanisms. MRDD Res Rev 12:129-140.

Back SA, Volpe JJ (1997) Cellular and molecular pathogenesis of periventricular white matter injury. MRDD Res Rev 3:96-107.

Back SA, Volpe JJ (1999) Approaches to the study of diseases involving oligodendroglial death. In: Cell death and diseases of the nervous system (Koliatsos V, Ratan R, eds), pp 401-428. Totowa, New Jersey: Humana Press.

Back SA, Riddle A, Hohimer AR (2006b) Role of instrumented fetal sheep preparations in defining the pathogenesis of human periventricular white matter injury. Journal of Child Neurology 21:582-589.

Back SA, Gan X-D, Li Y, Rosenberg PA, Volpe JJ (1998) Maturation-dependent vulnerability of oligodendrocytes to oxidative stress-induced death caused by glutathione depletion. J Neurosci 18:6241-6253.

Back SA, Luo NL, Borenstein NS, Volpe JJ, Kinney HC (2002a) Arrested oligodendrocyte lineage progression during human cerebral white matter development: dissociation between the timing of progenitor differentiation and myelinogenesis. J Neuropathol Exp Neurol 61:197-211.

Back SA, Luo NL, Borenstein NS, Levine JM, Volpe JJ, Kinney HC (2001) Late oligodendrocyte progenitors coincide with the developmental window of vulnerability for human perinatal white matter injury. J Neurosci 21:1302-1312.

Back SA, Craig A, Kayton R, Luo NL, Meshul C, Allcock N, Fern R (2007) Hypoxia-Ischemia preferentially triggers glutamate depletion from oligodendroglia and axons in perinatal cerebral white matter. Journal of Cerebral Blood Flow and Metabolism 27:334-347.

Back SA, Han BH, Luo NL, Chrichton CA, Tam J, Xanthoudakis S, Arvin KL, Holtzman DM (2002b) Selective vulnerability of late oligodendrocyte progenitors to hypoxia-ischemia. J Neurosci 22:455-463.

Back SA, Luo NL, Mallinson RA, O'Malley JP, Wallen LD, Frei B, Morrow JD, Petito CK, Roberts J, C.T., Murdoch GH, Montine TJ (2005b) Selective vulnerability of preterm white matter to oxidative damage defined by F_2-isoprostanes. Ann Neurol 58:108-120.

Baldwin B, Bell F (1963) The anatomy of the cerebral circulation of the sheep and ox. The dynamic distribution of the blood supplied by the carotid and vertebral arteries to cranial regions. J Anat, Lond 97:203-215.

Banker B, Larroche J (1962) Periventricular leukomalacia of infancy. A form of neonatal anoxic encephalopathy. Arch Neurol 7:386-410.

Barlow R (1969) The foetal sheep: morphogenesis of the nervous system and histochemical aspects of myelination. J Comp Neurol 135:249-262.

Basser P, Pierpaoli C (1996) Microstructural and physiological features of tissues elucidated by quantitative-diffusion-tensor MRI. J Mag Reson, Ser B 111:209-219.

Batchelor PG (2003) Anisotropic noise propagation in diffusion tensor MRI sampling schemes. Magn Reson Med 49:1143-1151.

Baud O, Greene A, Li J, Wang H, Volpe JJ, Rosenberg PA (2004) Glutathione peroxidase-catalase cooperativity is required for resistance to hydrogen peroxide by mature rat oligodendrocytes. J Neurosci 24:1531-1540.

Bax M, Tydeman C, Flodmark O (2006) Clinical and MRI correlates of cerebral palsy: the European Cerebral Palsy Study. JAMA 296:1602-1608.

Biran V, Joly L-M, Heron A, Vernet A, Vega C, Mariani J, Renolleau S, Charriaut-Marlangue C (2006) Glial activation in white matter following ischemia in the neonatal P7 rat brain. Exp Neurol 199:103-112.

Blamire AM, Rowe JG, Styles P, McDonald B (1999) Optimising imaging parameters for post mortem MR imaging of the human brain. Acta Radiol 40:593-597.

Brault S, Martinez-Bermudez A, Roberts II J, Cui Q-L, Fragoso G, Hemdan S, Lui H-N, Gobeil Jr F, Quiniou C, Kermorvant-Duchemin E, Lachance C, Almazan G, Varma D, Chemtob S (2004) Cytotoxicity of the E_2-Isoprostane 15_{2T}-IsoP on oligodendrocyte progenitors. Free Radic Biol Med 37:358-366.

Buchvald F, Keshe K, Griesen G (1999) Measurement of cerebral oxyhaemoglobin saturation and jugular blood flow in term healthy newborn infants by near-infrared spectroscopy and jugular venous occlusion. Biol Neonate 75:97-103.

Buser J, Maire J, Nelson K, Gong X, Riddle A, Luo N, Ren J, Nguyen T, Struve J, Sherman L, Miller S, Chau V, Hendson G, Ballabh P, Grafe M, Back S Myelination failure in human perinatal white matter injury: a disrupted repair mechanism linked to pre-oligodendrocyte maturation arrest. submitted.

Chau V, Poskitt KJ, McFadden DE, Bowen-Roberts T, Synnes A, Brant R, Sargent MA, Soulikias W, Miller SP (2009) Effect of chorioamnionitis on brain development and injury in premature newborns. Ann Neurol 66:155-164.

Cook C, Williams C, Gluckman P (1987a) Brainstem auditory evoked potential in the fetal lamb, in utero. J Dev Physiol 9:429-440.

Cook C, Gluckman P, Johnston B, Williams C (1987b) The development of the somatosensory evoked potential in the unanaesthetized fetal lamb. J Dev Physiol 9:441-456.

Counsell S, Allsop J, Harrison M, Larkman D, Kennea N, Kapellou O, Cowan F, Hajnal J, Edwards A, Rutherford M (2003) Diffusion-weighted imaging of the brain in preterm infants with focal and diffuse white matter abnormality. Pediatrics 112:176-180.

Craig A, Luo NL, Beardsley DJ, Wingate-Pearse N, Walker DW, Hohimer AR, Back SA (2003) Quantitative analysis of perinatal rodent oligodendrocyte lineage progression and its correlation with human. Exp Neurol 181:231-240.

D'Arceuil H, de Crespigny A (2007) The effects of brain tissue decomposition on diffusion tensor imaging and tractography. Neuroimage 36:64-68.

D'Arceuil HE, Westmoreland S, de Crespigny AJ (2007) An approach to high resolution diffusion tensor imaging in fixed primate brain. Neuroimage 35:553-565.

Dawe RJ, Bennett DA, Schneider JA, Vasireddi SK, Arfanakis K (2009) Postmortem MRI of human brain hemispheres: T2 relaxation times during formaldehyde fixation. Magnetic resonance in medicine : official journal of the Society of Magnetic Resonance in Medicine / Society of Magnetic Resonance in Medicine 61:810-818.

Deguchi K, Oguchi K, Takashima S (1997) Characteristic neuropathology of leukomalacia in extremely low birth weight infants. Pediatr Neurol 16:296-300.

Domingues AM, Taylor M, Fern R (2010) Glia as transmitter sources and sensors in health and disease. Neurochem Int 57:359-366.

Druzhyna N, Hollensworth S, Kelley M, Wilson G, Ledoux S (2003) Targeting human 8-oxoguanine glycosylase to mitochondria of oligodendroyctes protects against menadione-induced oxidative stress. Glia 42:370-378.

Eftekharpour E, Karimi-Abdolrezaee S, Wang J, El Beheiry H, Morshead C, Fehlings MG (2007) Myelination of congenitally dysmyelinated spinal cord axons by adult neural precursor cells results in formation of nodes of Ranvier and improved axonal conduction. J Neurosci 27:3416-3428.

Eggli P, Lucocq J, Ott P, Grabe W, van der Zypen E (1992) Ultrastructural localization of hyaluronan in myelin sheaths of the rat central and rat and human peripheral nervous systems using hyaluronan-binding protein-gold and link protein-gold. Neuroscience 48:737-744.

Fern R, Moller T (2000) Rapid ischemic cell death in immature oligodendrocytes: a fatal glutamate release feedback loop. J Neurosci 20:34-42.

Fern R, Davis P, Waxman S, Ransom B (1998) Axon conduction and survival in CNS white matter during energy deprivation: a developmental study. J Neurophysiol 79:95-105.

Ferriero DM (2004) Neontal brain injury. New England Journal of Medicine 351:1985-1995.

Ferriero DM (2006) Can we define the pathogenesis of human periventricular white-matter injury using animal models? Journal of Child Neurology 21:580-581.

Ferriero DM, Miller SP (2010) Imaging selective vulnerability in the developing nervous system. J Anat 217:429-435.

Follet PL, Rosenberg PA, Volpe JJ, Jensen FE (2000) NBQX attenuates excitotoxic injury to the developing white matter. J Neurosci 20:9235-9241.

Fragoso G, Martinez-Bermudez A, Lui H-N, Khorchid A, Chemtob S, Mushynski W, Almazan G (2004) Developmental differences in H_2O_2-induced oligodendrocyte cell death: role of glutathione, mitogen-activated protein kinases and caspase 3. J Neurochem 90:392-404.

Greisen G (1986) Cerebral blood flow in preterm infants during the first week of life. Acta Paediatr Scand 75:43-51.

Greisen G, Borch K (2001) White matter injury in the preterm neonate: the role of perfusion. Dev Neurosci 23:209-212.

Grether J, Nelson KB, Walsh E, Willoughby RE, Redline R (2003) Intrauterine exposure to infection and risk of cerebral palsy in very preterm infants. Arch Pediatr Adolesc Med 157:26-32.

Guilfoyle DN, Helpern JA, Lim KO (2003) Diffusion tensor imaging in fixed brain tissue at 7.0 T. NMR Biomed 16:77-81.

Hagberg H, Peebles D, Mallard C (2002) Models of white matter injury: comparison of infectious, hypoxic-ischemic, and excitotoxic insults. MRDD Res Rev 8:30-38.

Hamrick S, Miller SP, Leonard C, Glidden D, Goldstein R, Ramaswamy V, Piecuchi R, Ferriero DM (2004) Trends in severe brain injury and neurodevelopmental outcome in premature newborn infants: the role of cystic periventricular leukomalacia. J Pediatr 145:593-599.

Haynes RL, Billiards SS, Borenstein NS, Volpe JJ, Kinney HC (2008) Diffuse axonal injury in periventricular leukomalacia as determined by apoptotic marker fractin. Pediatr Res 63:656-661.

Haynes RL, Folkerth RD, Keefe RJ, Sung I, Swzeda LI, Rosenberg PA, Volpe JJ, Kinney HC (2003) Nitrosative and oxidative injury to premyelinating oligodendrocytes in periventricular leukomalacia. J Neuropathol Exp Neurol 62:441-450.

Hirayama A, Okoshi Y, Hachiya Y, Ozawa Y, Ito M, Kida Y, Imai Y, Kohsaka S, Takashima S (2001) Early immunohistochemical detection of axonal damage and glial activation in extremely immature brains with periventricular leukomalacia. Clin Neuropathol 20:87-91.

Huang H, Xue R, Zhang J, Ren T, Richards LJ, Yarowsky P, Miller MI, Mori S (2009) Anatomical characterization of human fetal brain development with diffusion tensor magnetic resonance imaging. J Neurosci 29:4263-4273.

Huppi PS, Murphy B, Maier SE, Zientara GP, Inder TE, Barnes PD, Kikinis R, Jolesz FA, Volpe JJ (2001) Microstructural brain development after perinatal cerebral white matter injury assessed by diffusion tensor magnetic resonanance imaging. Pediatrics 107:455-460.

Inder TE, Andersen NJ, Spencer C, Wells S, Volpe JJ (2003) White matter injury in the premature infant: a comparison between serial cranial ultrasound and MRI at term. AJNR Am J Neuroradiol 24:805-809.

Inder TE, Warfield S, Wang H, Huppi PS, Volpe JJ (2005a) Abnormal cerebral structure is present at term in premature infants. Pediatrics 115:286-294.

Inder TE, Neil JJ, Kroenke CD, Dieni S, Yoder B, Rees S (2005b) Investigation of cerebral development and injury in the prematurely born primate by magnetic resonance imaging and histopathology. Dev Neurosci 27:100-111.

Jenkinson M, Smith S (2001) A global optimisation method for robust affine registration of brain images. Med Image Anal 5:143-156.

Kinney H, Back S (1998) Human oligodendroglial development: relationship to periventricular leukomalacia. Semin Pediatr Neurol 5:180-189.

Kroenke CD, Bretthorst GL, Inder TE, Neil JJ (2005a) Diffusion MR imaging characteristics of the developing primate brain. Neuroimage 25:1205-1213.

Kroenke CD, Bretthorst GL, Inder TE, Neil JJ (2005b) Diffusion MR imaging characteristics of the developing primate brain. Neuroimage 25:1205-1213.

Kroenke CD, Taber EN, Leigland LA, Knutsen AK, Bayly PV (2009) Regional patterns of cerebral cortical differentiation determined by diffusion tensor MRI. Cereb Cortex 19:2916-2929.

Lazebnik RS, Lancaster TL, Breen MS, Lewin JS, Wilson DL (2003) Volume registration using needle paths and point landmarks for evaluation of interventional MRI treatments. IEEE Trans Med Imaging 22:653-660.

Lebenberg J, Hérard A-S, Dubois A, Dauguet J, Frouin V, Dhenain M, Hantraye P, Delzescaux T (2010) Validation of MRI-based 3D digital atlas registration with histological and autoradiographic volumes: an anatomofunctional transgenic mouse brain imaging study. NeuroImage 51:1037-1046.

Leviton A, Gilles F (1984) Acquired perinatal leukoencephalopathy. Ann Neurol 16:1-10.

Lin S, Rhodes P, Lei M, Zhang F, Cai Z (2004) a-Phenyl-n-*tert*-butyl-nitrone attenuates hypoxic-ischemic white matter injury in the neonatal rat brain. Brain Res 1007:132-141.

Litt J, Taylor H, Klein N, Hack M (2005) Learning disabilities in children with very low birthweight:prevalence, neuropsychological correlates and educational interventions. J Learn Disabil 8:130-141.

Liu YY, Silverstein FS, Skoff R, Barks JD (2002) Hypoxic-ischemic oligodendroglial injury in neonatal rat brain. Pediatr Res 51:25-33.

Lodygensky G, West T, Stump M, Holtzman D, Inder T, Neil J (2010) In vivo MRI analysis of an inflammatory injury in the developing brain. Brain Behav Immun 24:759-767.

Lodygensky G, West T, Moravec M, Back S, Dikranien K, Holtzman D, Neil J (2011) Diffusion characteristics associated with neuronal injury and glial activation following hypoxia-ischemia in the immature brain. Magnetic Resonance in Medicine in press.

Macchi G, Cioffi RP (1992) An in vivo and post mortem MRI study in multiple sclerosis with pathological correlation. Ital J Neurol Sci 13:97-103.

Marin-Padilla M (1997) Developmental neuropathology and impact of perinatal brain damage. II: white matter lesions of the neocortex. J Neuropathol Exp Neurol 56:219-235.

Mathur AM, Neil JJ, Inder TE (2010) Understanding brain injury and neurodevelopmental disabilities in the preterm infant: the evolving role of advanced magnetic resonance imaging. Semin Perinatol 34:57-66.

McClure M, Riddle A, Manese M, Luo N, Rorvik D, Kelly K, Barlow C, Kelly JJ EJ, Bernard SL, Glenny RW, Barlow CH, Vinecore K, Roberts C, Hohimer A, Back S (2008) Cerebral blood flow heterogeneity in preterm sheep: lack of physiological support for vascular boundary zones in fetal cerebral white matter. J Cereb Blood Flow Metab 28:995-1008.

McGrath DM, Vlad RM, Foltz WD, Brock KK (2010) Technical note: fiducial markers for correlation of whole-specimen histopathology with MR imaging at 7 tesla. Med Phys 37:2321-2328.

McQuillen P, Miller S (2010) Congenital heart disease and brain development. Ann N Y Acad Sci 1184:68-86.

Menke J, Michel E, Hildebrand S (1997) Cross-spectral analysis of cerebral autoregulation dynamics in high risk preterm infants during the perinatal period. Pediatr Res 42:690-699.

Ment LR, Hirtz D, Huppi PS (2009) Imaging biomarkers of outcome in the developing preterm brain. Lancet Neurol 8:1042-1055.

Miller S, Ferriero D (2009) From selective vulnerability to connectivity: insights from newborn brain imaging. Trends Neurosci 32:496-505.

Miller S, Vigneron D, Henry R, Bohland M, Ceppi-Cozzio C, Hoffman C, Newton N, Partridge JC, Ferriero DM, Barkovich AJ (2002) Serial quantitative diffusion tensor MRI of the premature brain: development in newborns with and without injury. J Magn ResonImaging 16:621-632.

Miller SP, Cozzio CC, Goldstein RB, Ferriero DM, Partridge JC, Vigneron DB, Barkovich AJ (2003) Comparing the diagnosis of white matter injury in

premature newborns with serial MR imaging and transfontanel ultrasonagraphy findings. AJNR Am J Neuroradiol 24:1661-1669.

Nagara H, Inoue T, Koga T, Kitaguchi T, Tateishi J, Goto I (1987) Formalin fixed brains are useful for magnetic resonance imaging (MRI) study. Journal of the Neurological Sciences 81:67-77.

Nelson KB, Grether J, Dambrosia J, Walsh E, Kohler S, Satyanarayana G, Nelson P, Dickens B, Phillips T (2003) Neonatal cytokines and cerebral palsy in very preterm infants. Pediatr Res 53:600-607.

Partadiredja G, Miller R, Oorschot D (2003) The number, size, and type of axons in rat subcortical white matter on left and right sides: a stereological, ultrastructural study. J Neurocytol 32:1165-1179.

Penning D, Grafe J, Hammond R, Matsuda Y, Patrick J, Richardson B (1994) Neuropathology of the near-term and midgestation ovine fetal brain after sustained in utero hypoxemia. Am J Obstet Gynecol 170:1425-1432.

Pierson CR, Folkerth RD, Billiards SS, Trachtenberg FL, Drinkwater ME, Volpe JJ, Kinney HC (2007) Gray matter injury associated with periventricular leukomalacia in the premature infant. Acta Neuropathol 114:619-631.

Pitt D, Boster A, Pei W, Wohleb E, Jasne A, Zachariah CR, Rammohan K, Knopp MV, Schmalbrock P (2010) Imaging cortical lesions in multiple sclerosis with ultra-high-field magnetic resonance imaging. Arch Neurol 67:812-818.

Pyrds O (1991) Control of cerebral circulation in the high-risk neonate. Ann Neurol 30:321-329.

Reddy K, Mallard C, Guan J, Marks K, Bennet L, Gunning M, Gunn A, Gluckman P, Williams C (1998) Maturational change in the cortical response to hypoperfusion injury in the fetal sheep. Pediatr Res 43:674-682.

Riddle A, Luo N, Manese M, Beardsley D, Green L, Rorvik D, Kelly K, Barlow C, Kelly J, Hohimer AR, Back SA (2006) Spatial heterogeneity in oligodendrocyte lineage maturation and not cerebral blood flow predicts fetal ovine periventricular white matter injury. Journal of Neuroscience 26:3045-3055.

Riddle A, Dean J, Buser J, Gong X, Maire J, Chen K, Ahmad T, Chen V, Nguyen T, Kroenke C, Hohimer AR, Back SA (2011) Histopathological correlates of MRI-defined chronic perinatal white matter injury. Annals of Neurology: in press.

Roessmann U, Gambetti P (1986) Pathological reaction of astrocytes in perinatal brain injury. Immunohistochemical study. Acta Neuropathol 70:302-307.

Rutherford MA, Supramaniam V, Ederies A, Chew A, Bassi L, Groppo M, Anjari M, Counsell S, Ramenghi LA (2010) Magnetic resonance imaging of white matter diseases of prematurity. Neuroradiology 52:505-521.

Salter M, Fern R (2005) NMDA receptors are expressed in developing oligodendrocyte processes and mediate injury. Nature 438:1167-1171.

Schafer DP, Rasband MN (2006) Glial regulation of the axonal membrane at nodes of Ranvier. Curr Opin Neurobiol 16:508-514.

Schmierer K, Scaravilli F, Barker GJ, Gordon R, MacManus DG, Miller DH (2003) Stereotactic co-registration of magnetic resonance imaging and histopathology in post-mortem multiple sclerosis brain. Neuropathol Appl Neurobiol 29:596-601.

Segovia K, Mcclure M, Moravec M, Luo N, Wang Y, Gong X, Riddle A, Craig A, Struve J, Sherman L, Back S (2008) Arrested oligodendrocyte lineage maturation in chronic perinatal white matter injury. Ann Neurol 63:517-526.

Sherman L, Back S (2008) A GAG reflex prevents repair of the damaged CNS. Trends Neurosci 31:44-52.

Sizonenko SV, Kiss JZ, Inder T, Gluckman PD, Williams CE (2005) Distinctive neuropathologic alterations in the deep layers of the parietal cortex after moderate ischemic-hypoxic injury in the P3 immature rat brain. Pediatr Res 57:865-872.

Sizonenko SV, Sirimanne E, Mayall Y, Gluckman PD, Inder T, Williams C (2003) Selective cortical alteration after hypoxic-ischemic injury in the very immature rat brain. Pediatr Res 54:263-269.

Skov L, Pyrds O, Griesen G, Lou H (1992) Estimation of cerebral venous oxygen saturation in newborn infants by near infrared spectroscopy. Pediatr Res 32:52-55.

Sloane J, Batt C, Ma Y, Harris Z, Trapp B, Vartanian T (2010) Hyaluronan blocks oligodendrocyte progenitor maturation and remyelination through TLR2. Proc Natl Acad Sci USA 107:11555-11560.

Smith SM, Jenkinson M, Woolrich MW, Beckmann CF, Behrens TE, Johansen-Berg H, Bannister PR, De Luca M, Drobnjak I, Flitney DE, Niazy RK, Saunders J, Vickers J, Zhang Y, De Stefano N, Brady JM, Matthews PM (2004) Advances in functional and structural MR image analysis and implementation as FSL. Neuroimage 23 Suppl 1:S208-219.

Struve J, Maher P, Li Y, Kinnery S, Fehlings MG, Kuntz Ct, Sherman LS (2005) Disruption of the hyaluronan-based extracellular matrix in spinal cord promotes astrocyte proliferation. GLIA 52:16-24.

Sun SW, Neil JJ, Song SK (2003) Relative indices of water diffusion anisotropy are equivalent in live and formalin-fixed mouse brains. Magn Reson Med 50:743-748.

Sun SW, Neil JJ, Liang HF, He YY, Schmidt RE, Hsu CY, Song SK (2005) Formalin fixation alters water diffusion coefficient magnitude but not anisotropy in infarcted brain. Magn Reson Med 53:1447-1451.

Takashima S, Tanaka K (1978) Development of cerebrovascular architecture and its relationship to periventricular leukomalacia. Arch Neurol 35:11-16.

Thevenaz P, Ruttimann UE, Unser M (1998) A pyramid approach to subpixel registration based on intensity. IEEE Trans Image Process 7:27-41.

Tovi M, Ericsson A (1992) Measurements of T1 and T2 over time in formalin-fixed human whole-brain specimens. Acta Radiol 33:400-404.

Tsuji M, Saul J, du Plessis A, Eichenwald E, Sobh J, Crocker R, Volpe J (2000) Cerebral intravascular oxygenation correlates with mean arterial pressure in critically ill premature infants. Pediatrics 106:625-632.

van Duijn S, Nabuurs RJA, van Rooden S, Maat-Schieman MLC, van Duinen SG, van Buchem MA, van der Weerd L, Natté R (2011) MRI artifacts in human brain tissue after prolonged formalin storage. Magnetic resonance in medicine : official journal of the Society of Magnetic Resonance in Medicine / Society of Magnetic Resonance in Medicine.

Volpe JJ (2001) Neurobiology of periventricular leukomalacia in the premature infant. Pediatr Res 50:553-562.

Volpe JJ (2008) Neurology of the Newborn. Philadelphia: W.B. Saunders.

Volpe JJ (2009) Brain injury in premature infants: a complex amalgam of destructive and developmental disturbances. Lancet Neurology 8:110-124.

Wang X, Xu L, Wang H, Zhan Y, Pure E, Feuerstein G (2002) CD44 deficiency in mice protects brain from cerebral ischemia injury. Journal of Neurochemistry 83:1172-1179.

Wilke S, Thomas R, Allcock N, Fern R (2004) Mechanism of acute ischemic injury of oligodendroglia in early myelinating white matter: the importance of astrocyte injury and glutamate release. J Neuropathol Exp Neurol 68:872-881.

Wilson-Costello D, Fridedman H, Minich N, Fanaroff A, Hack M (2005) Improved survival rates with increased neurodevelopmental disability for extremely low birth weight infants in the 1990s. Pediatrics 115:997-1003.

Woolrich MW, Jbabdi S, Patenaude B, Chappell M, Makni S, Behrens T, Beckmann C, Jenkinson M, Smith SM (2009) Bayesian analysis of neuroimaging data in FSL. Neuroimage 45:S173-186.

Yong-Hing CJ, Obenaus A, Stryker R, Tong K, Sarty GE (2005) Magnetic resonance imaging and mathematical modeling of progressive formalin fixation of the human brain. Magnetic resonance in medicine : official journal of the Society of Magnetic Resonance in Medicine / Society of Magnetic Resonance in Medicine 54:324-332.

Yoo TS, Ackerman MJ, Lorensen WE, Schroeder W, Chalana V, Aylward S, Metaxas D, Whitaker R (2002) Engineering and algorithm design for an image processing Api: a technical report on ITK--the Insight Toolkit. Stud Health Technol Inform 85:586-592.

Young RSK, Hernandez MJ, Yagel SK (1982) Selective reduction of blood flow to white matter during hypotension in neonatal dogs: a possible mechanism of periventricular leukomalacia. Ann Neurol 12:445-448.

Yoxall C, Weindling A (1998) Measurment of cerebral oxygen consumption in the human neonate by near infrared spectroscopy: Cerebral oxygen consumption increases with advancing gestational age. Pediatr Res 44:283-290.

Yushkevich PA, Piven J, Hazlett HC, Smith RG, Ho S, Gee JC, Gerig G (2006) User-guided 3D active contour segmentation of anatomical structures: significantly improved efficiency and reliability. Neuroimage 31:1116-1128.

Zhiheng H, Liu J, Cheung P-Y, Chen C (2009) Long-term cognitive impairment and myelination deficiency in a rat model of perinatal hypoxic-ischemia brain injury. Brain Res 1301:100-109.